Heinrich Heine
Universität
Düsseldorf

Merits and Limits of Biological Systems Modeling Strategies

Inaugural dissertation

for the attainment of the title of doctor
in the Faculty of Mathematics and Natural Sciences
at the Heinrich Heine University Düsseldorf

presented by

Nadia Heramvand

from Tehran

Düsseldorf, May 2022

from the institute for Mathematical Modeling of Biological Systems
at the Heinrich Heine University Düsseldorf

Published by permission of the
Faculty of Mathematics and Natural Sciences at
Heinrich Heine University Düsseldorf

Supervisor: Prof. Dr. Markus Kollmann
Co-supervisor: Prof. Dr. Achim Tresch

Date of the oral examination: 28.09.2022

I would like to dedicate this thesis to my loving

Parents

Nima

Aran

Avina

Declaration

I hereby declare that this dissertation is the result of my own work. No other person's work has been used without due acknowledgment. This dissertation has not been submitted in the same or similar form to other institutions. I have not previously failed a doctoral examination procedure.

Nadia Heramvand
May 2022

Acknowledgements

I would like to acknowledge the help and support of all people through this journey,

Specifically my supervisor Prof. Dr. Markus Kollmann and my thesis advisors Prof. Dr. Mathias Beller, and Prof. Achim Tresch as well as all the members of the Mathematical Modeling of Biological Systems Institute at Heinrich Heine University. And also I would like to thank Prof. Dr. Dr. med. Christian Jung and Dr. med. Maryna Masyuk at Cardiology Department of the Düsseldorf University Hospital.

And I can not forget to thank my family and friends for all the unconditional support.

And finally thank Nima, Aran, and Avina for their encouragement and their unconditional love.

Table of contents

List of figures

List of tables

0 | Abstract

A biological system is a group of relevant components on different scales, such as genes, cells, or body organs that work together to fulfill a particular task. The components of a biological system are connected through complex interactions and exhibit a collective behavior that belongs to the system and not to each component on its own. Understanding the function of such a complex system is a great challenge and requires advanced experiments and computations. There are two approaches to analyzing a biological system. The first one is the reductionist view, which explains the whole system by studying each component separately. One of the significant drawbacks of reductionism is that it misses the interactions between the components and therefore, is not able to explain the collective behavior that belongs to the whole system and not each component. On the other hand, a second approach is a system approach, which considers a biological system as an integrated system and studies how the components interact and work together. Such an integrated system can be considered as a network of interacting individual components. On this basis, systems biology aims to infer and model the underlying network. Therefore, understanding a biological system requires complete sets of experiments to uncover the underlying relations between the components, and for a highly complex system such as the human body, it is not possible to examine each component.

This thesis takes the systems approach. Chapter 2 explains how the complex structure of a biological system together with insufficient experiments limit the inference of the biological network. Chapter 3,4 simplify the human body and represent it as compartments to describe the kinetics of two anticoagulation drugs in the body.

Overall, the present study suggests that, before the start of the modeling, based on the complexity level of the problem and the available data, an optimal scale should be chosen. This means, in the case of a highly complex system and lack of enough information, a useful and informative approach is reducing unnecessary details and decomposing the system into simpler subsystems (compartments), and seeing how these subsystems work together.

0.1 List of Publications

Publication 1 :

Experimental noise cutoff boosts inferability of transcriptional networks in large-scale gene-deletion studies

C. F. Blum*, N. Heramvand*, A. S. Khonsari & M. Kollmann

This article is published in Nature Communications 9(1), 2018.

https://www.nature.com/articles/s41467-017-02489-x

* equal contribution

Publication 2 :

Pharmacosimulation of interruptions and its solution in intravenous administration of cangrelor

Maryna Masyuk, Nadia Heramvand, Johanna M. Muessig, Amir M. Nia, Amin Polzin, Markus Kollmann, Malte Kelm, Christian Jung

This article is published in Clinical Hemorheology and Microcirculation, vol. 68, no. 4, pp. 421-425, 2018

https://content.iospress.com/articles/clinical-hemorheology-and-microcirculation/ch170323

Publication 3 :

Pharmacosimulation of delays and interruptions during administration of tirofiban: a systematic comparison between EU and US dosage regimens

Nadia Heramvand*, Maryna Masyuk*, Johanna M. Muessig, Amir M. Nia, Athanasios Karathanos1, Amin Polzin, Marco Valgimigli, Paul A. Gurbel, Udaya S. Tantry, Malte Kelm, Christian Jung

This article is published in Journal of Thrombosis and Thrombolysis, 2022.

https://link.springer.com/article/10.1007/s11239-022-02654-0

* equal contribution

"Every object that biology studies is a system of systems."

Francois Jacob (1974)

1 Introduction

1.1 General Introduction

A biological system consists of several biologically relevant components that are connected through numerous ways of complex interactions and comprise a unified whole. Examples of biological systems span a wide range of scales from large scale such as human body and body organs to small scale such as organelle and gene regulatory pathways. These biological systems exhibit a unique behavior that belongs to the whole system and is not shared by the individual components on their own. For example, the heart is made up of cells that don't have the property of pumping. Therefore, a biological system or a natural system is considered to be an integrated system. Understanding such a complex natural system represents the greatest intellectual and experimental challenge that biologists are facing. Recently mathematical and computational models are increasingly applied to interpret experimental observations as well as describe and model the behavior of the system under study.

There are two views to modeling a natural process. The first one is reductionism, identified by René Descartes, the founder of *Cartesian physics*. He formulated the notion that complex situations can be analyzed by reducing them to manageable pieces, examining each in turn, and reassembling the whole from the behavior of the pieces [1].

For a biological system, the reduction is the idea that the system is studied at the lowest possible level, and the experimental studies should be aimed at uncovering molecular and biochemical causes [2]. Nevertheless, it has been argued that the reductionist approach cannot explain the collective behavior and emergent properties, which belong to the whole system and not to the individual members [3]. The reductionist view dominated science in the past, but now it is accepted that new approaches are required to better understand how parts came together to give rise to something greater than parts [4]. In the other words, life at

any level − from cell functioning to human behavior − is defined by dynamical interactions between its components, not by the properties of each component in isolation [5].

The second approach to analyzing and modeling a natural process is a *system* approach, which is opposite to the reductionist view. A system is defined as a set of components and relations among them [6]. Therefore, a biological system is an integrated system where its components interact with each other, to fulfill a specific function. Such an integrated system has a distinct quality called an *organization* and can be considered to be a *network* of interacting individual components.

System approach and integration of biological systems have long been of interest to eminent scientists. Among them, one can refer to the great contribution of Paul A. Weise and Ludwig von Bertalanffy who made the system concept applicable in biology in the early 20th century. Bertalanffy is widely known as the father of *general systems theory* (GST) and has a significant role in the advancement of theoretical biology [7–9].

Furthermore, it is notable to mention the work of Robert Rosen in the 1960s, whose life-long quest for the secrets of life is well-known [10]. Rosen applied relational models by neglecting structural details of components and focusing on the relationship between organizations (components) of biological systems. To that end, Rosen used category theory, which is the extension of graph theory to represent the relations between the components of the system. He explicitly referred to the components as black boxes without making any assumptions about the internal structure of these boxes [11, 12].

In the last two decades, *Networks Science* is widely used as a relational approach in biology to represent the structure and function of various biological systems [13, 14]. The most recent effort was to describe different network topologies mathematically. In 1998 Watts and Strogatz explored the models of small-world networks [15]. By analogy with the popular notation of *"six degrees of separation"*, in human social network with the property of small-world, where any two people in the network can reach each other through a short sequence of the path. In 1999 Barabáshi and Albert developed the dynamical model of scale-free networks [16]. A network with the property of being scale-free contains components with many connections (hub). A scale-free network grows to some extent that the ratio in the number of connections versus all other components is constant.

Network diagrams are used as an abstract representation of biological systems that illustrate the interactions between any biological components in different biological organization levels [1] such as genes, proteins, metabolites, drugs, body organs or humans (Figure 1.1)

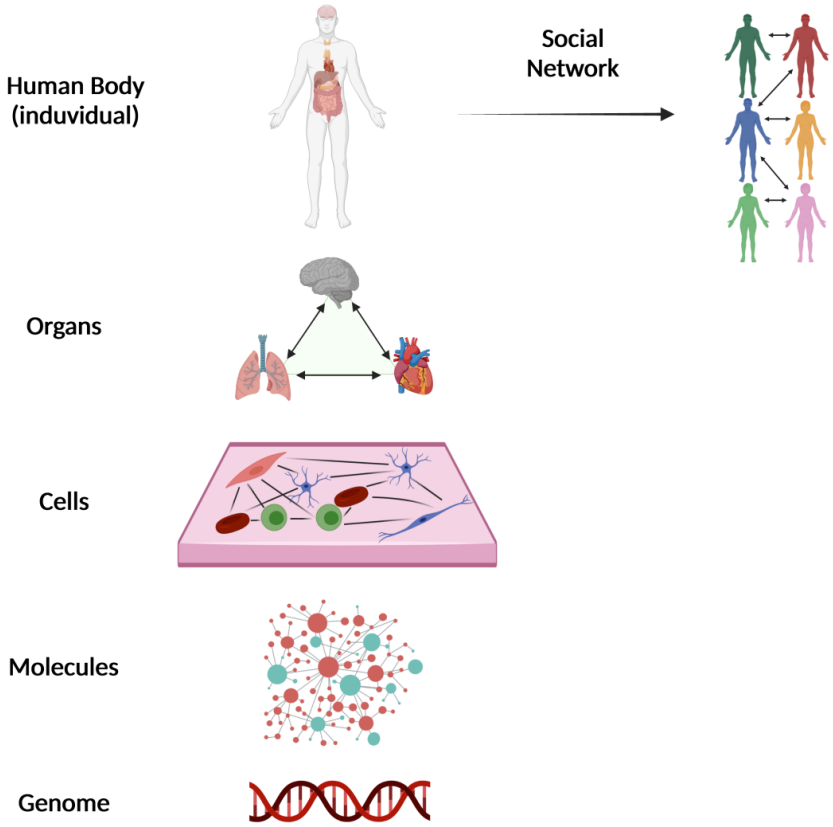

Fig. 1.1 Biological systems at different organization levels

To uncover and model the underlying interacting network, experimental data, such as high-throughput data generated by *omics* technologies or clinical data, along with advanced computational methods are required. However, due to the high complexity of the biological systems and limitations of available experimental data, it is hard to precisely assess the interacting pattern and consequently model the function of the system.

The complexity of the biological systems could mainly be the result of a large number of interacting components as well as the complicated underlying network. For example, for a highly connected network, a large number of empirical experiments are required to uncover all interactions. Conducting such extensive experiments is often time-consuming

[1] Levels of the organization are structures in nature, usually defined by part-whole relationships, with things at higher levels being composed of things at the next lower level [17].

and always affected by measurement errors. Therefore, available experimental datasets are often incomplete and noisy.

Now the question is that, according to the mentioned limitations, what is an appropriate approach to develop a mathematical model that could simulate the function of a biological system *in silico* and in particular could predict outcomes in different circumstances?

One strategy is discovering the design principles of a biological system [18]. One example of design principles is the network motifs, which are small repeated patterns of connectivity, found in different regulatory networks [14]. The discovery of network motifs requires the reduction of large biological networks into collections of small and separable subsystems.

Network motifs are applied as templates for more detailed models that represent the structures of the biological networks and describe their functions. In fact, network motifs are considered simple building blocks of complex networks. For example, the Feed-Forward Loop (FFL) structure is understood as persistence detector for noisy input signals in metabolic regulation in E. coli [14]. Figure 1.5 represent a coherent type 1 FFL motif (see section 1.2.8).

The functionality of network motifs is expected to be *modular* which requires that these motifs always perform a similar function in different biological contexts [19, 20]. However, many network motifs can perform several different functions depending on different biological conditions [21]. One example is the role of positive feedback on the stripe pattern of gene expression in early embryogenesis. The feed-forward motifs are the minimal networks that are capable of stipe patterning. Positive feedback within genes has been hypothesized that enhances the sharpness and the precision of gene expression borders. *Munteanu et al.* have shown that the addition of positive feedback can have different effects on two different designs of feed-forward motif [22].

Furthermore, searching for network motifs or specific biological pathways of a biological network requires decomposition and localization of the component parts. Such approaches are successful at the cellular level in the sense that they make the investigation of cellular processes traceable. Nevertheless, they could limit the understanding of the overall function of parts of more complex systems. For example diseases such as cancer can rarely be explained by studying just single pathways [23].

As a complement approach, another strategy is the decomposition of a complex biological system into relatively independent and simpler modules (subsystems). Then appropriate experimental and computational approaches can be designed to discover the function of each

module and see how they are related to each other. From a mathematical point of view, this approach is desired because some modules can be considered as functions whose inputs are determined by the rest of the network.

Such strategies of abstraction are useful because first, they simplify the identification of the biological mechanisms ,and second, they explain the system-level patterns of organization [24]. This is similar to a good road map that omits unnecessary details while representing only the essential features for purpose of navigation [23].

One example of the abstraction approach is compartmental modeling, which is applied to describe the transport of materials or energies throughout a system. Compartment models are composed of sets of interconnected mixing chambers, which are homogeneous with uniform concentration. For example, in pharmacokinetics (PK) [2] , compartmental models are widely used to describe the time course of the concentration of a drug in a body fluid after administration. This is applied for effective therapeutic management of drugs in an individual patient, such as defining the optimum dosage regime of the drug [25]. In PK modeling, the body is represented as a single or series of compartments, where one compartment is a group of tissues with similar blood flow and drug affinity. Compartments are considered as black boxes without exact internal structures, with inputs and outputs defined as flow fluxes and change of concentrations expressed as rate equations. Compartmental models are descriptive models that do not explain the mechanism, rather they explain the kinetics of a drug in the body (see section 1.3.2).

The following sections will introduce the basic principles of the biological networks and compartmental modeling which are related to the results of the manuscripts of the later chapters.

[2] Pharmacokinetics is a branch of pharmacology that studies the dynamic movement of chemical material throughout the body of a biological system.

1.2 Complex Network

This section presents the bases of the complex networks. First, complex systems are defined and then networks are introduced as a map to represent the complex systems. Afterward, the basic concepts of networks are characterized, such as network types, network measures, and network models. And finally, gene regulatory networks, as one of the most important examples of biological systems are mathematically described.

1.2.1 What is a Complex System

A complex system are systems with many interacting components. Examples of complex systems are the communication systems, human brain, a living cell, an organism, human social networks, ants society, migrating birds, and many other examples. Instead of focusing on the components themselves, a complex system can be understood by focusing on how the components within a system are related to one another. Therefore, the differences between systems are due to the differences in how these parts depend on and how affect one another. For example, steam and ice are made of water molecules but, because of differences in interactions between the molecules, they have very different properties. In this example, the behavior that distinguishes between gas and solid is called the emergence property. The emergence property is a collective behavior that cannot be understood from systems parts individually, rather it can be understood through the relationship between parts. In addition to the emergence property which is the most striking property of the complex systems, they have some other properties in common; The interactions between system components are nonlinear. Complex systems are open and share information with their environment and can coordinate their internal structure and pattern to adapt to the external condition. This property is self-organizing that arises not from an external or internal control but rather autonomously from cooperative interactions between the components of the system. Self-organization makes a complex system robust and resistant to perturbations. In addition, based on evidence, various range of complex systems follow universal laws. It means that different complex systems can have similar behavioral and structural properties. For example, all gas-liquid phase transition common behavior despite different component molecules [26, 27].

1.2.2 What is a network?

A network is, in simplest form, a collection of points joined together in pairs by lines. The points are referred to as *nodes* or *vertices* and lines are referred to as *links* or *edges*. This set of nodes and links represents the relationships among the components of a system. In other words, a network is a map showing how components of a system interact with each other. There are many systems of interest to scientists that are composed of individual parts or components that are linked together by some means. One example is the internet which is the collection of computers linked by data connections. This network representation offers a common language to study systems that may differ greatly in nature, appearance, or scope. In the scientific literature the term *network* and *graph* are used interchangeably; The combination of the {*network*, *node*, *link*} often refers to real systems. For example, the WWW is a network web documents linked by URLs. The metabolic network represents all chemical reactions between metabolites and the enzymes to catalyze a metabolic reaction in a cell. On the other hand, the combination of {*graph*, *vertex*, *edge*} are used to represent these networks mathematically [28, 13].

1.2.3 Why networks are important?

In order to facilitate the analysis of complex systems, they can be represented as **networks** where systems components are abstracted by nodes and their interaction by links. For this reason, network science aims to build models that reproduce the properties of the real complex system.

Many systems of interest are composed of components linked together in some way. Examples include the Internet, a collection of computers linked by data connections, or Biological Networks consisting of molecules such as DNA, RNA, protein, and metabolites linked by interactions between these molecules. Gene Regulatory Networks (GRNs) are specific examples of biological networks which consist of molecular species and their regulatory interactions to control gene expression in the cell.

Every network can be represented in the form of an adjacency matrix **A**. If we denote an edge between node i and j by (i , j), the adjacency matrix **A** of a simple network is the matrix with elements of A_{ij} such that:

$$A_{ij} = \begin{cases} 1 & \text{if there is a link between nodes } i \text{ and } j\text{ ,} \\ 0 & \text{otherwise.} \end{cases}$$

1.2.4 Types of Network Links

Different types can be considered for the links of networks depending on their nature and function. Links can be:

Undirected links if there is a single connection between node i and node j .

Directed links if a link between nodes i and j is represented by an arrow, thus indicating a direction from node i to node j or vice versa.

Weighted links if link between node i and j has an associated weight. The weighted network can be represented by giving the elements of the adjacency matrix values equal to the weight (Figure 1.2).

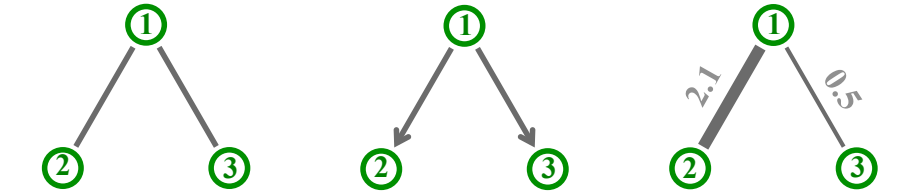

Undirected links

$$A = \begin{bmatrix} 0 & 1 & 1 \\ 1 & 0 & 0 \\ 1 & 0 & 0 \end{bmatrix}$$

Directed links

$$A = \begin{bmatrix} 0 & 1 & 1 \\ 0 & 0 & 0 \\ 0 & 0 & 0 \end{bmatrix}$$

Weighted links

$$A = \begin{bmatrix} 0 & 2.1 & 0.5 \\ 2.1 & 0 & 0 \\ 0.5 & 0 & 0 \end{bmatrix}$$

Fig. 1.2 Types of network links and network adjacency matrix

1.2.5 General Network Measures

Here are the most basic network measures to compare and characterize different complex networks:

Path

A path in a network is any sequence of nodes such that any successive pair of nodes in the sequence is connected by a link in the network.
The **length of a path** in a network, is the number of links transversed along the path. The **shortest path**, is a path between two nodes such that no shorter path exists [28].

Degree

The degree (or connectivity) of a node in a network is the number of links connected to it. The degree of node i is denoted by k_i. For an undirected network of N nodes, the degree of node i can be written in terms of the elements of the adjacency matrix:

$$k_i = \sum_{j=1}^{N} A_{ij} \tag{1.1}$$

For an undirected network, the total number of the links is equal to the half of the summation of all node degrees:

$$m = \frac{1}{2}\sum_{i=1}^{N} k_i = \frac{1}{2}\sum_{ij} A_{ij} \tag{1.2}$$

The mean degree, $< k >$, of an undirected network is

$$< k >= \frac{1}{N}\sum_{j=1}^{N} k_i \tag{1.3}$$

In directed networks node i has two deferent degrees: *in-degree*, k_i^{in}, which is the number of incoming links connected to node i, and an *out-degree*, k_i^{out}, which is the number of outgoing links from node i. By assuming $A_{ij} = 1$, representing a connection from node i to node j, in- and out-degree can be written

$$k_i^{in} = \sum_{j=1}^{N} A_{ji}, \quad k_j^{out} = \sum_{j=1}^{N} A_{ij} \tag{1.4}$$

Each link going out from a node enters another node. Therefore, the total number of links, m in a directed network equals the total to the number of outgoing links, or equivalently the total number of the incoming links:

$$m = \sum_{i=1}^{N} k_i^{in} = \sum_{i=1}^{N} k_i^{out} = \sum_{ij} A_{ij} \tag{1.5}$$

Thus the mean in-degree, $< k^{in} >$ and the mean out-degree, $< k^{out} >$, of every directed network are equal:

$$< k^{in} >= \frac{1}{N} \sum_{i=1}^{N} k_i^{in} = \frac{1}{N} \sum_{i=1}^{N} k_i^{out} =< k^{out} > \tag{1.6}$$

Degree Distribution

Degree distribution $P(k)$ is the probability distribution of the fraction of nodes with a given degree, or equivalently is the probability that a random node has a given degree.

1.2.6 Random Network Models

Erdös-Rényi Random Network

One of the simplest, well-studied, and famous random models, is Erdös-Rényi random network (ER random network). According to this model, each possible link appears independently and with identical probability (p) [29]. The degree distribution of a random network is given by a binomial distribution (See figure 1.3). Therefore, the probability of a node to have degree k, $P(k)$ is:

$$P(k) = \begin{pmatrix} N-1 \\ k \end{pmatrix} p^k (1-p)^{(N-1-k)} \tag{1.7}$$

where N is total number of nodes in the network.

As the number of nodes becomes large, the degree distribution converges to a Poisson distribution:

$$P(k) \approx e^{-<k>} \frac{< k >^k}{k!} \tag{1.8}$$

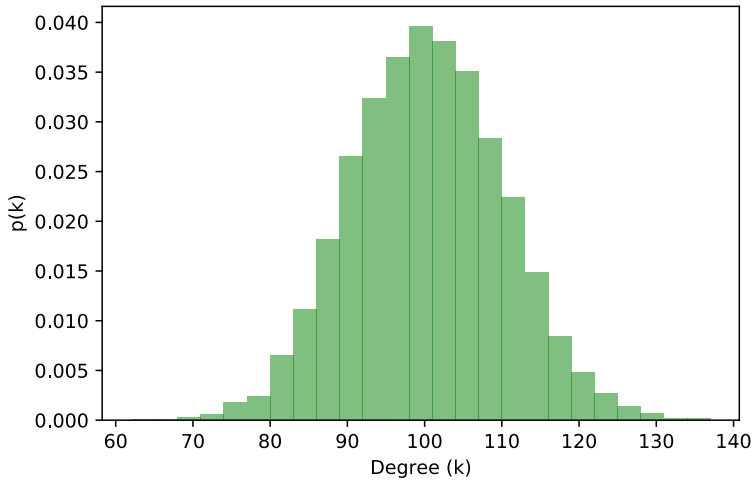

Fig. 1.3 Degree distribution of a random where size of the network, N, is 10,000 and each two nodes are connected with the probability of 0.01.

How to construct an ER random network?

To construct a random network with the size of N, where nodes are connected with the probability of p, three steps are needed:

1 Start with N isolated nodes.

2 Select a pair of nodes, i, and j. Then select a random number between 0 and 1. If the number is smaller than p, connect node i and node j, otherwise leave them disconnected.

3 Repeat step 2 for each $\frac{N(N-1)}{2}$ node pairs.

Scale-Free Network

Despite ER random networks that follow Poisson degree distribution, a scale-free network is a network whose degree distribution follows a power law [16]:

$$P(k) \sim k^{-\gamma} \tag{1.9}$$

where γ denotes *degree exponent* and determines many properties of the systems (Figure 1.4).

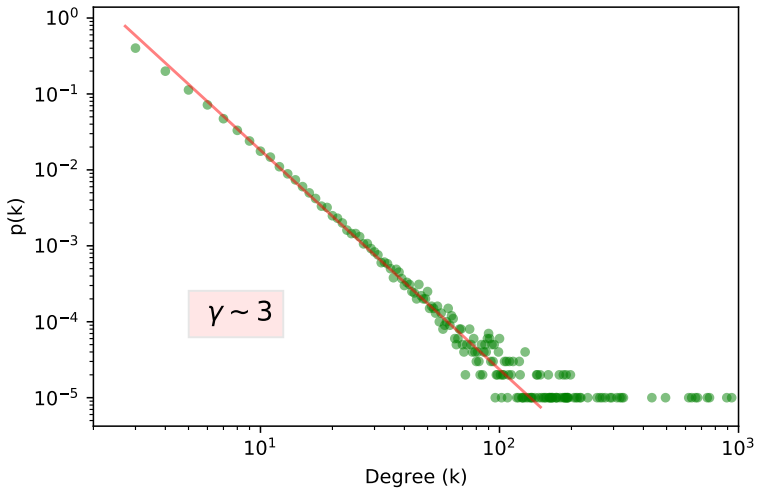

Fig. 1.4 Degree distribution of a scale-free network where network size, N, is 100,000 and m is 3, generated by Barabàshi-Albert model (see section 1.2.7).

For a directed scale free network characterized by *in-* and *out-degree*, the probability that a randomly chosen node had k^{in} or k^{out} degree, can be approximated by a power law degree distribution:

$$P(k^{in}) \sim k^{-\gamma_{in}}, \quad P(k^{out}) \sim k^{-\gamma_{out}} \tag{1.10}$$

where γ_{in} and γ_{out} are the degree exponent for the in- and out-degree, respectively.

As examples of scale-free networks one can refer to a few network projections of metabolic chemical reactions that belong to the class of scale-free networks [30, 31]. Another example of scale-free networks is the gene regulatory network of yeast obtained from the microarray data from 273 different yeast gene deletions [32].

The main difference between a random network and a scale-free network is the tail of the degree distribution. Scale-free networks are characterized by high-degree nodes called hubs. In a network with a power-law degree distribution, nodes with low degrees appear more frequently. These numerous small nodes are held together by a few highly connected hubs. Therefore, aimed removal of high degrees nodes can affect the network's topology significantly. The smaller the value of γ, the more important the role of the hubs is in the network.
For a scale-free network, the degree of the biggest hub, k_{max}, called *natural cutoff* of the degree distribution[13]

$$k_{max} = k_{min} N^{\frac{1}{\gamma-1}} \tag{1.11}$$

where k_{min} is the degree of the smallest node.

Equation 1.11 indicates that the larger the network, the larger is the size of the biggest hub.

How do the properties of a scale-free network change with γ?

Many properties of a scale-free network depend on the value of the degree exponent,γ:

Anomalous Regime ($\gamma \leqslant 2$) for $\gamma < 2$ the exponent in 1.11 is larger than one. Therefore for sufficiently large size of the network, N, the degree of the largest hub exceeds the total number of the network N. In the other words, k_{max} grows faster than the size of the network, N. Similarly, the average degree, $< k >$ diverges in the $N \to \infty$ limit.

Scale-Free Regime $2 < \gamma < 3$ Based on equation 1.11, k_{max} grows with the size of the network with exponent $\frac{1}{\gamma-1}$ which is smaller than 1. In this regime hubs link to a large number of small-degree nodes, creating short distances between them [33]. This regime is also called *ultra-small world*.

Random Network Regime ($\gamma > 3$) for large γ the degree distribution, $P(k)$ decays significantly fast which makes the size of the hubs small and less numerous. Under this condition, the scale-free network is indistinguishable from a random network.

1.2.7 How to construct a scale-free network?

The *Barabàshi-Albert* model or *BA* model, is the best known generative networks model describing scale-free networks [16]. In this model, nodes are connected one by one to a suitably preferentially chosen set of previously existing nodes. Assume at time = 0, a network consists of n_0 nodes which are linked together arbitrarily and each node has at least one link. The network develops following two steps:

(A) Growth: At each time step, t, a new node with n links ($n \leqslant n_0$) connects to the m nodes that already exist in the network (m is the degree of the new node, n).

(B) Preferential attachment: The probability $\prod(k)$ that a link of the new node connects to node i depends on the degree k_i as.

$$P(\text{links to node } i) = \prod(k_i) = \frac{k_i}{\sum_j k_j} \tag{1.12}$$

After t time steps the Barabàshi-Albert model generate a network with $N = t + n_0$ nodes and $m_0 + mt$ links. The achieved network has a power-law degree distribution, which is characterized by degree exponent $\gamma \sim 3$ [13] (Figure 1.4).

1.2.8 Network Motifs

Network motifs are simple building blocks of a complex network. Network motifs are defined as patterns of interconnections (or subgraphs) occurring in complex networks at numbers significantly higher than those in randomized networks [34]. For example one of the known motifs of transcriptional regulation networks of *Escherichia coli* , is "Feed-Forward Loop" (FFL) defined by a transcription factor X that regulates a second transcription factor Y, such that both X and Y jointly regulate an operon Z.

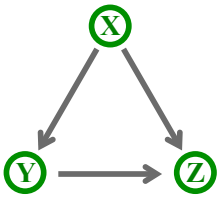

Fig. 1.5 Example of Feed-Forward Loop (FFL) motif

1.2.9 Gene Regulatory Networks

A Gene Regulatory Network or a genetic regulatory network (GRN) is a collection of DNA segments in a cell, which interact with each other(indirectly through their RNA and protein expression products) and with the other substances in the cell, therefore governing the rate at which genes are transcribed into mRNA, to control many cellular processes such as cell cycle, cellular differentiation, and apoptosis [35].

From a mathematical point of view, GRNs can be represented, as a directed network, where nodes denote genes and links denote their regulatory interactions. Nevertheless, revealing the architecture of a GRN is one of the key tasks in computational biology. In this regard, computational biology seeks a comprehensive model to represent the overall structure of the network and describe the full range of behaviors that these systems exhibit under different conditions.

1.2.10 Inference of Gene Regulatory Networks

There are several experimental techniques to reveal an unknown gene regulatory network. Gene perturbation experiment is one of the examples which includes gene knockout, gene over-expression, RNA interference (RNAi), or drug treatment, to record the response of the perturbation on the other genes. This experimental data is called gene expression data or node activity data. Reconstruction of gene regulatory network from node activity data called *reverse engineering* or *netwtork inference*.

1.2.11 Mathematical Modeling of Gene Regulatory Networks

Ordinary differential equations (ODEs) are popular tools to model the dynamical system of the GRNs. They represent the concentration of gene products by continuous time-dependent variables. More precisely, for a system of GRN consisting of n interacting genes (nodes), gene expression level over time is modeled through the following differential equation:

$$\frac{d\mathbf{x}(t)}{dt} = \mathbf{f}(\mathbf{x}, \theta, \mathbf{u}) \tag{1.13}$$

where, $\mathbf{x} = [x_1, ..., x_n]^T$ and $x_i \in \mathbf{x}$ is the expression level of gene i. $\theta = [\theta_1, ..., \theta_n]^T$, and $\theta_i \in \theta$ is sets of parameters quantifying interactions between gene i and the rest of regulator genes. $\mathbf{u} = [u_1, ..., u_n]^T$ and $u_i \in \mathbf{u}$ is external perturbation on gene i. $\mathbf{f} = [f_1, ..., f_n]^T$ $f_i : \mathbb{R}^n_{\geqslant 0} \to \mathbb{R}$ is a function representing nonlinear regulatory interaction between gene i and the rest of regulator genes.

Although gene regulations are often nonlinear, nonlinear models become quite difficult to treat mathematically, due to the complex structure of the involving network and the sparsity of experimental data. For this reason, most of the existing approaches for GRN inference apply linear or additive models [36]. In fact, linear models are the first-order terms of the Taylor expansion of f function near the steady-state. Surprisingly, linear models can capture

the main features of the network and can provide a good starting point for further modeling and analysis.

The linear form of equation 1.13 is:

$$\frac{d\mathbf{x}(t)}{dt} = \mathbf{J}\mathbf{x}(t) + \mathbf{u}(t) \tag{1.14}$$

where, $\mathbf{J} \in \mathbb{R}^{N\times N}$ and $J_{ij} = \frac{\partial f(x_i)}{\partial x_j}$ is Jacobian matrix or connectivity matrix, representing the effect of gene i on gene j.

In steady state condition equation 1.14 can be written as:

$$\mathbf{x} = -\mathbf{J}^{-1}\mathbf{u} \tag{1.15}$$

where $\mathbf{x}$ is gene expression level and the observed gene expression (node activity) is

$$\mathbf{y} = \mathbf{x} + \varepsilon \tag{1.16}$$

where ε is measurement noise.

In fact, $\mathbf{y}$ is the gene expression data obtained from experiment and here an appropriate network inference method should be applied to estimate connectivity matrix, $\mathbf{J}$, which reveals the structure of the regulatory network.

1.2.12 Linear Stability Analysis for ODEs

Biological systems always face different unpredictable disturbances such as fluctuations in molecular concentrations, environmental noise, and ... . Therefore, Robustness is one important property allowing a system to maintain its function despite internal and external perturbations [37]. For this reason, the analysis of local and global behavior of the system in equilibrium is the most concern in computational biology.

ODEs sets of equation 1.13, can be written in a more abstract form of

$$\dot{\mathbf{x}} = \mathbf{f}(\mathbf{x}) \tag{1.17}$$

suppose that $\mathbf{x}^*$ is an equilibrium point. By definition, $\mathbf{f}(\mathbf{x}) = 0$. A small perturbation of such a system could be written in form of Taylor expansion of the right-hand side of the differential equation:

$$\dot{\mathbf{x}} = \mathbf{f}(\mathbf{x}^*) + \frac{\partial \mathbf{f}}{\partial \mathbf{x}}|_{\mathbf{x}^*}(\mathbf{x} - \mathbf{x}^*) + ... \tag{1.18}$$

The partial derivative in the above equation is **Jacobian matrix**:

$$\mathbf{J} = \begin{bmatrix} \frac{\partial f_1}{\partial x_1} & \frac{\partial f_1}{\partial x_2} & \dots & \frac{\partial f_1}{\partial x_n} \\ \frac{\partial f_2}{\partial x_1} & \frac{\partial f_2}{\partial x_2} & \dots & \frac{\partial f_2}{\partial x_n} \\ \vdots & \vdots & \ddots & \vdots \\ \frac{\partial f_n}{\partial x_1} & \frac{\partial f_n}{\partial x_2} & \dots & \frac{\partial f_n}{\partial x_n} \end{bmatrix} \tag{1.19}$$

If $\delta\mathbf{x} = \mathbf{x} - \mathbf{x}^*$ is defined as small deviation from equilibrium, then $\dot{\delta\mathbf{x}} = \mathbf{x}$, which can be written as $\dot{\delta\mathbf{x}} = \mathbf{J}^*\delta\mathbf{x}$. The matrix $\mathbf{J}^*$ is Jocobian matrix at equilibrium point.

Theorem *An equilibrium point $\boldsymbol{x}^*$ of differential equation 1.17 is stable if all the eigenvalues of $\boldsymbol{J}^*$, the Jocobian evaluated at $\boldsymbol{x}^*$, have negative real parts. The equilibrium is unstable if at least one of the eigenvalues has a positive real part.* [38].

This theorem is called **Linear stability analysis** because the linear term of equation 1.18 is kept. This theorem does not mention what happens if some eigenvalues have zero real parts while the others are all negative. To answer this question, the non-linear terms must be kept as well in order to determine the stability. Dealing with this case requires nonlinear theory.

1.3 Pharmacokinetics

This section describes the movement of a drug into, through, and out of a living organism body under the title of Pharmacokinetics. First of all, the compartmental models are introduced to formulate the kinetics of a drug in the body. Then, types of Pharmacokinetics models and the fundamental concepts to develop a proper model are introduced.

1.3.1 Use of Drug

The use of a drug to treat disease goes back to the old history. Since drugs have compounds that are foreign to the body, they have the potential to harm rather than healing, especially when they are applied in the wrong dose for the individual patients being treated [39]. Therefore, the determination of the proper dose which is therapeutic but not toxic in an individual patient is required.

In addition to the correct use of an existing drug, scientific researchers are engaged in the process of discovering new drugs that are safe and effective for the treatment or prevention of disease. The following steps are involved in the drug development process:

1. The pharmacologically active molecule must be synthesized, isolated, or extract from various possible sources.

2. The formulation of the dosage form (i.e. tablet, capsules, etc) that will deliver a recommended dose to the "site of action" or a tissue target.

3. The establishment of a dosage regimen to provide an effective concentration of a drug in the body.

Only a successful integration of these aspects will result in successful drug therapy. To this end, a good knowledge of rate process (kinetics), chemistry, physiology, and pharmacology is essential to understand the dynamics of the substances administered to a living organism as a therapeutic agent. Pharmacokinetics which is the study of the movement of drugs, into, through, and out of the body, is the result of such a successful integration of Multidisciplinary knowledge.

What is Pharmcokinetics?

Pharmacokinetics (PK), derived from the Greek words *pharmakon* (drug) and *kinetikos* (movement), is used to describe the time course of drug absorption, distribution, metabolism, and excretion (ADME) of a compound in humans and animals [40]. Pharmacokinetics

describes how the concentration of a dosed drug and its metabolites in body fluids and tissues changes with time. It analyzes chemical metabolism to discover the fate of a drug from the moment that it is administrated up to the point at which it is eliminated from the body. Receptor sites of drugs are generally inaccessible to our observations or are widely distributed in the body, and therefore a direct measurement of drug concentrations at these sites is not practical. However, we can measure drug concentration in the blood or plasma, urine, saliva, and other easily sampled fluids. Normally PK models describe the time course of drugs' concentration in various areas of the body, e.g. plasma, kidney, receptors, as a function of time.

1.3.2 Compartmental Models - Simplification of a Physiologic System

The handling of a drug by the body is very complex. To predict the concentration of the administrated drug in the body, simplifications of the body structure are necessary. Therefore, a model of the body must be selected. Generally, the body as a physiological system is described by decomposition into numbers of interacting subsystems, called *compartments*. The compartments represent a group of similar organs or tissues. In the compartmental model, each compartment may exchange the drug with other compartments with a specific transfer rate constant. Figure 1.6 shows one example of the compartment model, where the body is divided into four compartments. After administration of a chemical substance, it can transfer between compartments with specific transport rates.

1.3.3 PK Modeling

PK modeling aims to describe the concentration of the drug in different areas of the body. Compartment models are the basic type of models which are used in pharmacokinetics. Compartmental models are categorized by the number of compartments needed to describe the behavior of the drug in the body. There are several types of compartmental models:

- one compartment model
- two compartment model
- multi-compartment model

The selection of a compartment model entirely depends upon the distribution characteristics of a drug after administration. Organs and tissues in which drug distribution is similar are grouped into one compartment. In other words, since the heart pumps blood constantly, it can

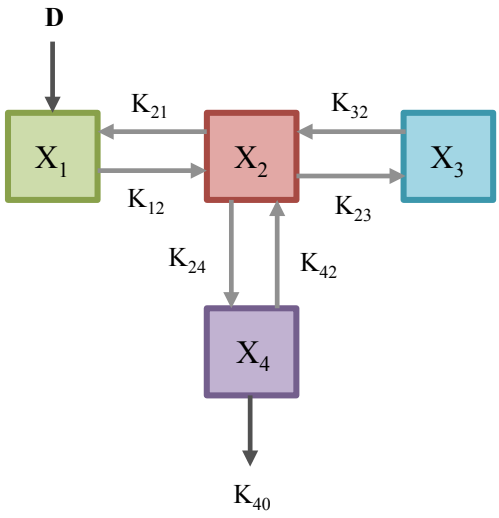

Fig. 1.6 Example of compartment model, where the body is divided into four homogeneous compartments and each arrow shows the transfer of the drug across the compartments with specific transfer rates. K_{mn} is transfer rate of the drug from compartment **m** to compartment **n** and **D** is the administration dosage.

be assumed that the concentration of the drug is the same within the bloodstream at a given time. Therefore, the highly perfused organs, such as the heart, liver, and kidneys often have similar drug distribution patterns, so these organs may be considered as one compartment, which usually is referred to as *central compartment*. The other compartment that includes fat tissue, muscle tissue, and cerebrospinal fluid is referred to as the *peripheral compartment*, which is less well perfused than the central compartment. This type of organ grouping for central and peripheral compartments is shown in Figure 1.7.

1.3.4 One Compartment Model

In a one-compartment model, the body is assumed as a kinetically homogeneous unit, in which after drug administration, the drug distributes throughout the body and equilibrates between tissues instantaneously. Therefore, all body organs and tissues are considered as a compartment and referred to as *central compartment*. The model can be depicted as Figure 1.8, where X_0 is intravenous bolus dosage, X_1 is the amount of drug in the central compartment and k_{10} is the elimination constant rate.

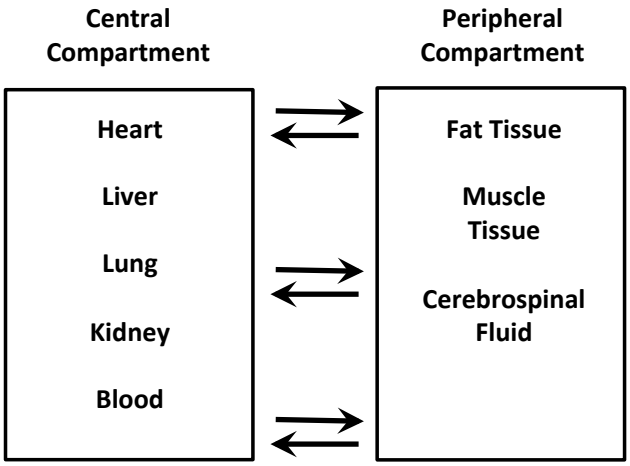

Fig. 1.7 Typical organ groups for central and peripheral compartments

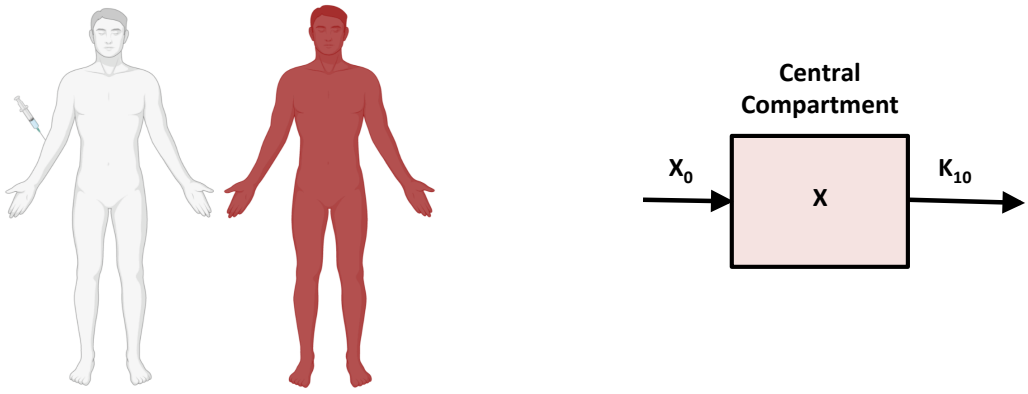

Fig. 1.8 One Compartment Model: Representation of the body as one homogenous unit

The mathematical differential equation that describes the relationship between the rate of elimination and the amount of the drug in the central compartment, in case the drug is administrated as an intravenous bolus dose, is:

$$\frac{dX_1}{dt} = -k_{10}X_1 \tag{1.20}$$

where the elimination rate $k_{10}$is constant.

Equation 1.20 results in:

$$X(t) = X_0 e^{-k_{10}t} \tag{1.21}$$

The following section defines fundamental PK parameters following the intravenous bolus administration of a drug. These parameters can be generalized and applied in the two-compartment model.

1.3.5 Fundamental Concepts

Volume of Distribution

The volume of distribution (V_d) has no direct physiological meaning; it is not a real volume and is usually referred to as the *apparent volume of distribution*. It is defined as that volume of plasma in which the total amount of drug in the body would be required to be dissolved to reflect the drug concentration attained in plasma: [41]

$$V_d = \frac{X_t}{(C_p)_t} = \frac{X_0}{(C_p)_0} \tag{1.22}$$

where X_t is the amount of the drug at any time t, $(C_p)_t$ is the concentration of drug at any time t, X_0 amount of drug at $t = 0$ (initial dosage), and $(C_p)_0$ is the plasma concentration of drug at $t = 0$.

Concentration

Drug concentration is defined as the amount of drug in a given volume of plasma (or serum):

$$C_p = \frac{X}{V} \tag{1.23}$$

where C_p is drug plasma concentration, X is the amount of drug in the body and V is the volume in which drug is distributed.

Dividing equation 1.21, by volume of distribution, results in drug plasma concentration as follows:

$$C_p(t) = C_{p0}e^{-k_{10}t} \tag{1.24}$$

where C_p is the plasma concentration of the drug at any time t and C_{p0} is the plasma concentration of the drug at time$= 0$.

Elimination Half Life

The time required to reduce the plasma concentration to one-half its initial value is defined as the half-life ($t_{1/2}$) [41]. From equation 1.21 the half of the initial plasma concentration is defined as follows:

$$\frac{C_{p0}}{2} = C_{p0}e^{-k_{10}t} \tag{1.25}$$

Therefore, the elimination half-life ($T_{\frac{1}{2}}$) is:

$$T_{\frac{1}{2}} = -\frac{\ln(0.5)}{k_{10}} = \frac{0.693}{k_{10}} \tag{1.26}$$

Clearance

Drug clearance (CL) is the volume of blood or plasma or mass of an organ effectively cleared of a substance by elimination (metabolism and excretion) per unit of time. A drug can be cleared by renal excretion or by metabolism or both. Clearance is additive and, total body clearance (CL_T) is the sum of all individual organ clearances that contribute to the overall elimination of drugs. Therefore, the total clearance is the sum of renal clearance. CL_r and non-renal clearance CL_{nr}:

$$CL_T = CL_r + CL_{nr} \tag{1.27}$$

and based on definition, clearance has the following mathematical relation with elimination rate constant, k_{10}, and the volume of distribution, V_d:

$$CL_T = k_{10} V_d \tag{1.28}$$

1.3.6 Two Compartment Model

As mentioned before, the Two-compartment PK model divides the body into central and peripheral compartments. The central compartment (compartment 1) consists of the plasma and tissues where the distribution of the drug is practically instantaneous (such as blood, heart, kidney, and liver). The peripheral compartment (compartment 2) consists of tissues where the distribution of the drug is slower (generally, muscle, lean tissues, and fat). Figure 1.9 represents schematically the two-compartment model, in which X_0 is the dose of the intravenously injected drug, X_1 is the amount of drug in the central compartment, X_2 is the amount of drug in the peripheral compartment, k_{12} and k_{21} are transferred rate constants from central compartment to peripheral compartment and conversely, k_{10} is elimination rate constant from the central compartment.

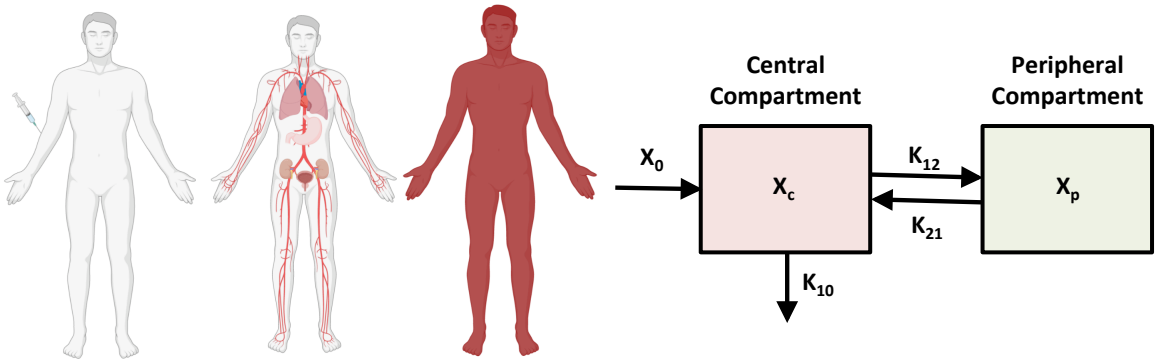

Fig. 1.9 Two-Compartment Model: Representation of the body as two homogenous parts where the drug distributes differently

Differential equation describing the change of drug mass during distribution and post-distribution phase is as following:

$$\frac{dX_1}{dt} = k_{21}X_2 - k_{12}X_1 - k_{10}X_1 \tag{1.29}$$

$$\frac{dX_2}{dt} = k_{12}X_1 - k_{21}X_2 \tag{1.30}$$

Integrating equation 1.29 yields an equation for the amount of drug in the central compartment (X_1) as a function of time after a single IV bolus dose (X_0):

$$X_1 = \frac{X_0(\alpha - k_{21})}{(\alpha - \beta)}e^{-\alpha t} + \frac{X_0(k_{21} - \beta)}{(\alpha - \beta)}e^{-\beta t} \tag{1.31}$$

where

$$\alpha + \beta = k_{12} + k_{21} + k_{10} \tag{1.32}$$

$$\alpha\beta = k_{21}k_{10} \tag{1.33}$$

and α is distribution rate constant and β is disposition or elimination (post-distribution) constant.

Dividing equation 1.31 by the volume of distribution of the central compartment, V_c, results in the time profile of the plasma concentration of the drug in the central compartment, C_p:

$$C_p(t) = \frac{X_0(\alpha - k_{21})}{V_c(\alpha - \beta)}e^{-\alpha t} + \frac{X_0(k_{21} - \beta)}{V_c(\alpha - \beta)}e^{-\beta t} \tag{1.34}$$

Equation 1.34 can be simplified to:

$$C_p(t) = Ae^{-\alpha t} + Be^{-\beta t} \tag{1.35}$$

where

$$A = \frac{X_0(\alpha - k_{21})}{V_c(\alpha - \beta)} \tag{1.36}$$

$$B = \frac{X_0(k_{21} - \beta)}{V_c(\alpha - \beta)} \tag{1.37}$$

In equation 1.35 A and B are empirical constant with units of concentration (e.g. μgmL^{-1}) [39].

According to equation 1.35, after intravenous administration of the drug, the resulting decrease of the drug's plasma concentration follows a biphasic pattern (see Figure 1.10).

- Distributive phase (or α phase): This phase is an initial phase of rapid decrease in plasma concentration. The decrease accounts for the drug distribution from the central compartment into the peripheral compartments. This phase ends when a pseudo-equilibrium of drug concentration is established between the central and peripheral compartments.
- Post-distributive phase (or β phase): This is a phase of a gradual decrease in plasma concentration starting after the distributive. The decrease is primarily attributed to drug elimination, which is, metabolism and excretion [42].

Method of residuals

The method of residual is a curve-fitting approach that is applied when the plasma concentration of a drug follows the two-compartment model. Based on this method, the biexponential plot of plasma concentration against time is separated into monoexponential segments [41]. This method is applied to determine the distribution and elimination rates. For an intravenous bolus injection of the drug, the first term of equation 1.35, $Ae^{-\alpha t}$, approaches zero faster than $Be^{-\beta t}$. The reason is that the slope of the α phase is greater than the slope of the β phase (Figure 1.10). Therefore at later times, the contribution of the first term of equation 1.35 is negligible and the plasma concentration of the drug approximates to:

$$C_p(t) \cong Be^{-\beta t} \tag{1.38}$$

According to equation 1.38, B and β can be estimated by extrapolation of a fitted line passing through the concentration-time points of the elimination phase. The y-intercept and the slope

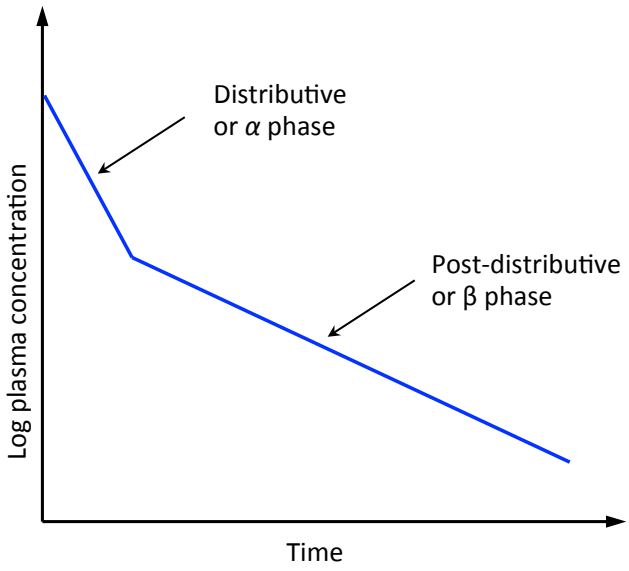

Fig. 1.10 Log of plasma concentration of drug in two-compartment model follows a biphasic pattern

of the extrapolated line are equal to the coefficient $\ln B$ and the elimination rate constant β respectively. The difference between the concentration-time points of the observed data and the values of $Be^{-\beta t}$, obtained from the extrapolated line, is called *residuals*. A and α of the absorption phase are estimated according to the semi-logarithmic plot of the residuals.

The method of the residuals can be summarized by the following steps (Figure 1.11) [43]

- concentration-time points data is plotted in a semi-logarithmic scale.
- a line is fitted to the elimination time points and the slope β and the intercept $\ln B$ of the line are estimated.
- for each time point the residuals, $C(t) - Be^{-\beta t}$, are calculated and plotted in a semi-logarithmic scale.
- a fitted line to the residuals estimates the A and α of the absorption phase.

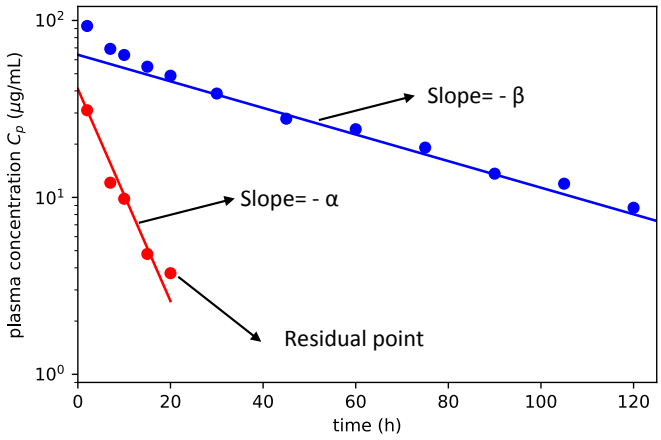

Fig. 1.11 Estimation of B, β, A, α by applying the method of residuals, the blue points refer to elimination phase and red points are residuals referring to absorption phase.

2 The Structural Complexity of Network Inference

2.1 Summary

Inference of a biological network such as a gene regulatory network (GRN) is identifying the interaction of the genes using experimental data. To obtain the experimental data, typically one node is perturbed and the response of the rest of the network is measured and recorded. For a GRN, a perturbation could be gene knock-out, gene knock-down, or drug treatment. The recorded experimental data is called node activity data (Figure 2.1).

The ability of the computational network inference approaches is limited by two fundamental factors: a) presence of measurement noise which leads to an inference of the false positive interactions, b) an insufficient number of perturbed nodes which makes the complete inference of the network almost impossible.

An Inference method unbiased toward measurement noise is introduced and based on that the fundamental limits of network inference such as insufficient perturbation data, in the absence of noise, and in the stationary condition is quantified analytically.

To investigate the effect of the insufficient perturbation experiments, the average number of inferable links is calculated. Inferable links are the maximum possible average number of links that can be inferred when not all but only a fraction of nodes are perturbed. Under such conditions, the impact of the structure of the network on the number of inferable links is studied. The most influencing structural feature is the size of the network (N), the average degree of the network($< k >$), and the degree exponent (γ) in the case of a scale-free net-

work. For this purpose, three classes of random networks with different average degrees are studied: random network, scale-free networks with incoming hubs, and scale-free network with outgoing hubs and random networks. To quantify the influence of different network structures on network inference, the area under the curve of the inference plot is defined as **inferability**. For example, Figure 2.2 illustrates the inference plot of a scale-free network with incoming links, in which the area under the curve is inferability.

In addition to the mentioned three classes of random networks, the inferability of two types of real networks, social and biological networks, are investigated. For these real networks the relation between inferability and average degree is shown (Table 2.1). The data of the real networks are taken from SNAP ↗ database (2015 download)[44].

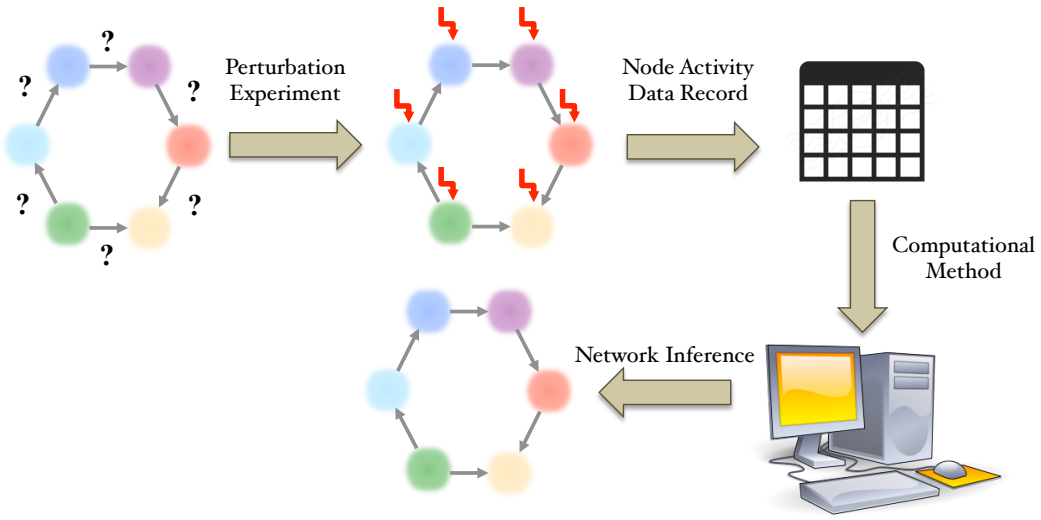

Fig. 2.1 Reconstruction of a biological network from experimental data

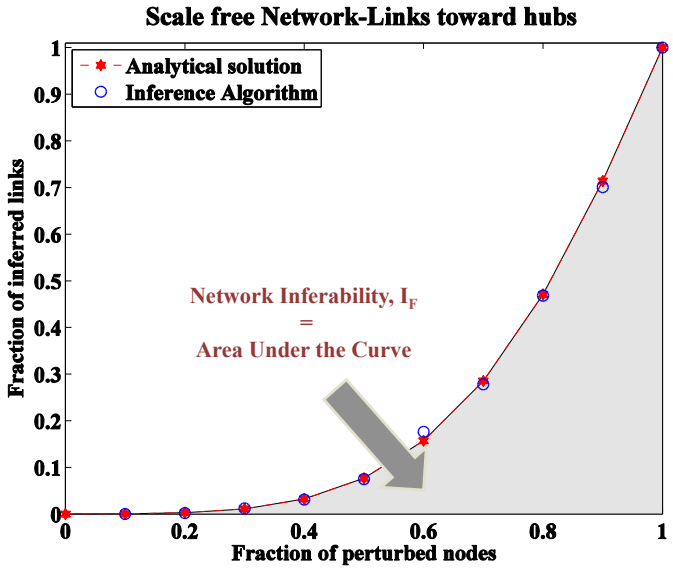

Fig. 2.2 The inference plot represents the number of inferable links relative to the number of perturbed nodes for a scale-free network with incoming hubs. Inferability is defined as the area under the curve of the inference plot, shown in gray

Table 2.1 Real network specifications

List of Real Networks				
Type	Name	Size	Average Degree	Inferability
Internet peer-to-peer networks				
	Gnutella05	8846	3.5993	0.1562
	Gnutella06	8717	3.6165	0.1551
	Gnutella08	6301	3.2974	0.1554
Social Networks				
	wiki-vote	7115	14.5733	0.1206
	Slashdot	77360	10.7053	0.1299
	Epinion	75879	6.7059	0.1423
	ego.twitter	81306	21.7467	0.1118
Communication Networks				
	email-EuAll	265214	1.5797	0.2787
World wide web				
	Web-NotreDame	325729	4.5120	0.1400
	Web-Standford	281903	8.2032	0.1539
	Web-Google	875713	5.8296	0.1645
	Web- Brek-Stan	685230	11.0920	0.1364
Nueral Network				
	Brain white matter	360	18.3389	0.1148
Human Protein-Protein Interaction Network				
	Human 01	2239	2.8816	0.1218
	Human 02	1706	3.6172	0.2016
Interactom Network				
	Yeast01	1278	0.2840	0.3285
	Yeast02	813	0.9360	0.3454
	Yeast03	2018	1.3404	0.3031
Transcription Network				
	Yeast-TC	688	1.5683	0.1575
	eColi TC02	1821	2.2015	0.1218
Metabolic Network				

2.2 Publication: Experimental noise cutoff boosts inferability of transcriptional networks in large-scale gene-deletion studies

Authors: C. F. Blum, N. Heramvand*, A. S. Khonsari & M. Kollmann
*N.Heramvand is the co-first author.
This article is published in Nature Communications 9(1), 2018.

Contribution of Nadia Heramvand:

- developed the counting procedure for inferable links and the Inferability measure
- developed the analytical formula of inferability
- generates scale-free and random networks with different average degrees and γ exponents
- analyze the inferability of random, scale-free and real networks with different sizes, average degrees, and gamma exponents
- wrote Supplementary Note 1.
- designed Figures 1 and 2
- contributed to the development of the computer code for the inference algorithm

nature COMMUNICATIONS

ARTICLE

DOI: 10.1038/s41467-017-02489-x OPEN

Experimental noise cutoff boosts inferability of transcriptional networks in large-scale gene-deletion studies

C.F. Blum[1,2], N. Heramvand[1,2], A.S. Khonsari[1] & M. Kollmann[1]

Generating a comprehensive map of molecular interactions in living cells is difficult and great efforts are undertaken to infer molecular interactions from large-scale perturbation experiments. Here, we develop the analytical and numerical tools to quantify the fundamental limits for inferring transcriptional networks from gene knockout screens and introduce a network inference method that is unbiased with respect to measurement noise and scalable to large network sizes. We show that network asymmetry, knockout coverage and measurement noise are central determinants that limit prediction accuracy, whereas the knowledge about gene-specific variability among biological replicates can be used to eliminate noise-sensitive nodes and thereby boost the performance of network inference algorithms.

[1] Institute for Mathematical Modeling of Biological Systems, Heinrich-Heine University of Düsseldorf, Universitätsstraße 1, 40225 Düsseldorf, Germany. [2] Max Planck Institute for Plant Breeding Research, Carl-von-Linné-Weg 10, 50829 Köln, Germany. C.F. Blum and N. Heramvand contributed equally to this work. Correspondence and requests for materials should be addressed to M.K. (email: markus.kollmann@hhu.de)

The functionality of a living cell is determined by the interplay of multiple molecular components that interact with each other. Generating a global map of these molecular interactions is an essential step to advance our understanding of the molecular mechanisms behind disease, development and the reprogramming of organisms for biotechnological applications[1]. The current advances in gene-editing methods[2] have scaled up the size of genome-wide single and double knockout libraries, ranging from microbes[3, 4] to higher eukaryotes[5] and open up a much more informative data source than inferring gene-regulatory networks from unspecific perturbations, such as stress or changes in growth conditions[6]. However, the detection of direct interactions between two genes from association measures–for example, the covariance between transcript levels–remains a highly non-trivial task, given the significant variation among biological replicates, the frequent case where the number of parameters exceeds the number of independent data points, and the high dimensionality of the inference problem. In addition, direct interactions inferred from transcriptome data typically oversimplify the molecular complexity behind gene regulation, which frequently involves protein–protein interactions and modifications on protein or DNA level. Consequently, gene interaction networks inferred from transcriptome studies should in general not be interpreted as or compared with gene-regulatory networks. In this work we first investigate the causes that affect network inferability by introducing a simple network inferability measure and subsequently use the gained insight to design an unbiased, scalable network inference algorithm.

Results

Network inferability. The existence of a direct interaction between gene A as source of regulation (source node) and gene B as target of regulation (target node) can be detected if a significant part of the transcriptional activity of B can be explained by the transcriptional activity of A but not by the transcriptonal activities of the remaining genes in the network. Thus, a necessary condition for identifiability or inferability of links is the knowledge about the information that can be transmitted by alternative routes in the network, which can be obtained by targeted, external perturbations of node activities[7]. As most gene perturbation screens are incomplete—for example, owing to the fact that essential genes cannot be knocked out—we have in general the situation that a significant amount of interactions within an N-gene network are non-inferable, regardless of the amount of experimental replicates and the strength of perturbations.

Limits of network inferability. To estimate the upper bound of links that can be inferred from knockout screens, we consider a directed but not necessarily acyclic network of N nodes, with node activities as observables and a predefined subset of nodes that are perturbed independently by external forces. The perturbed nodes are randomly distributed within the network and we denote by q the fraction of nodes that are perturbed. We assume that an arbitrarily large set of perturbation experiments can be generated, with the freedom to tune the perturbation strength for each node independently. We further assume that other perturbative sources and measurement noise are absent. Calculation of the expected fraction of inferable links, $F(q)$, can be carried out by a simple counting procedure (Figs 1a and 2a), assuming that links can be represented by noiseless, linear functions with non-zero slope. Under these conditions, a directed link between source and target node is inferable–or equivalently its link strength is identifiable–if it is not possible to fully reconstruct the activity state of the source node from the node activities of the remaining network. Consequently, a link is inferable if a part of the variation of the target node can be only explained by the source node, given that a link between them exists, and implies non-zero partial correlation between source and target node. To allow detection of arbitrarily small partial correlations, we make sure that there exists a finite fraction of experiments for each target node, where the target node is not perturbed (Online Methods and Supplementary Note 1). If, for example, only one node in the network is perturbed that targets multiple other nodes, its node activity can be fully reconstructed by any of its targets, resulting in zero partial correlation coefficients, which implies that none of the directed links can be inferred (Fig. 1a, right network). In contrast, if two out of three nodes are perturbed, all links targeting the unperturbed node are inferable (Fig. 1a, left network). In addition, nodes that have been identified as targets of the current target node can be removed prior to inference. This is because an existing link from the actual target node excludes them from

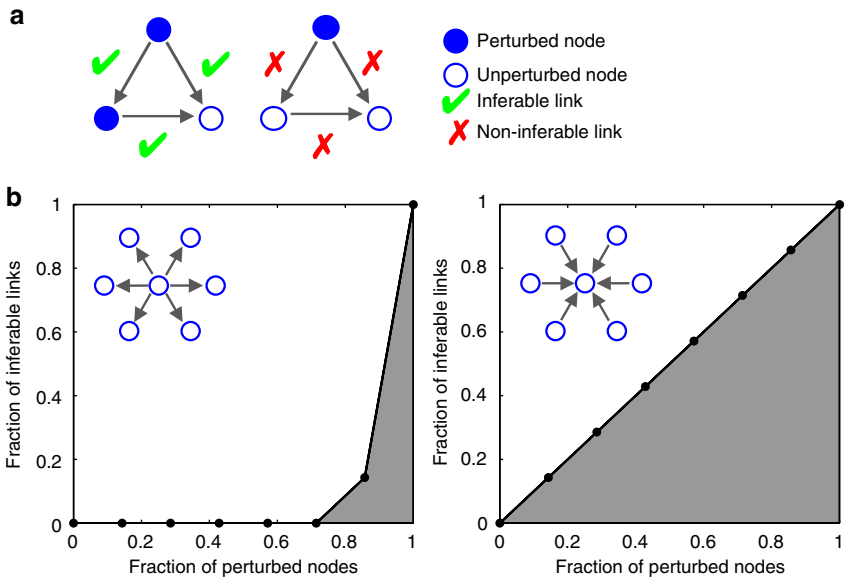

Fig. 1 Illustrative example of network inferability. **a** Left network: fully inferable network; Right network: non-inferable network. **b** Fraction of inferable links versus fraction of perturbed nodes in the network. Left panel: hub of outgoing nodes. Right panel: hub of incoming nodes

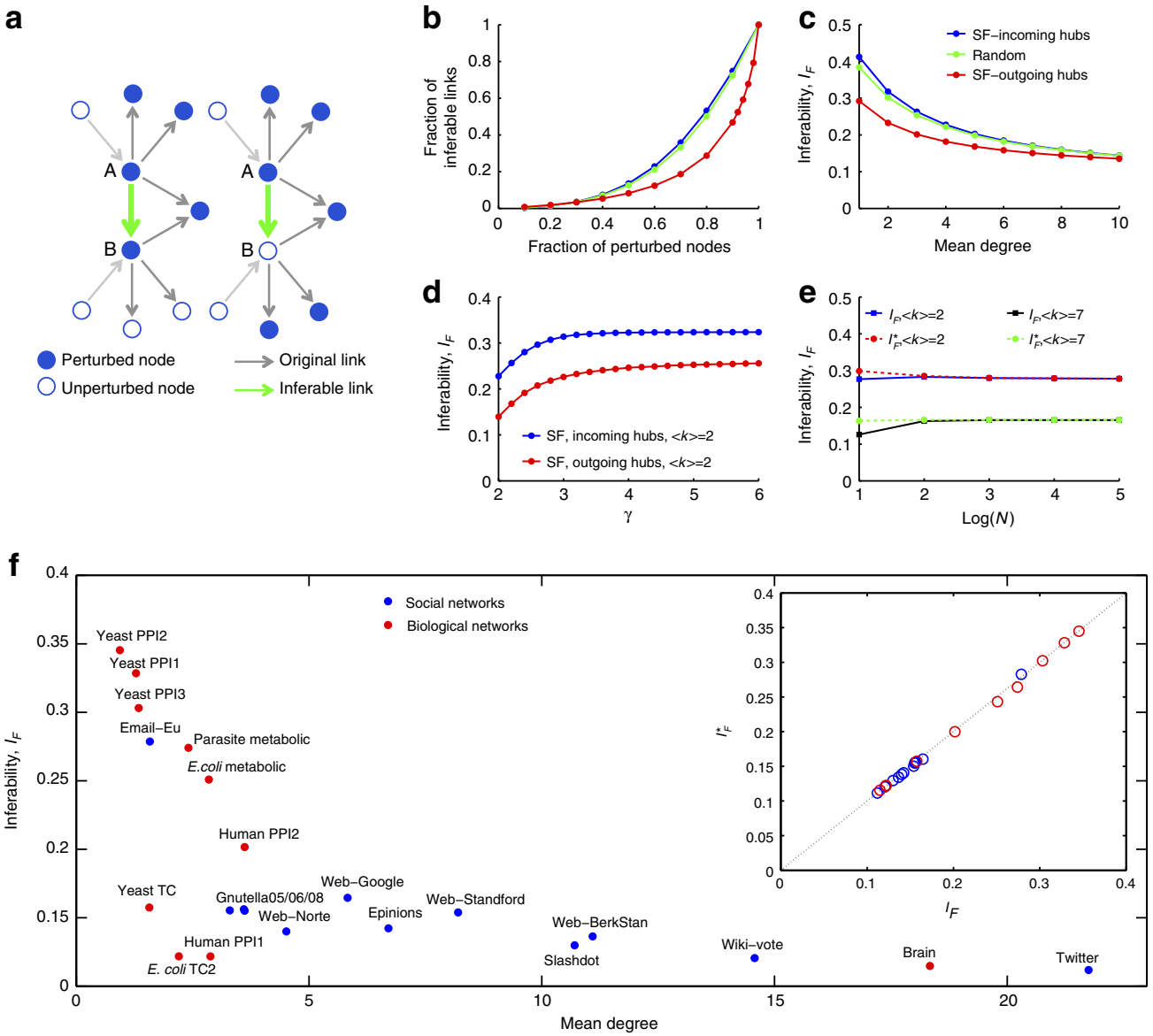

Fig. 2 Inferability as a function of network parameters. **a** Directed links are inferable if either all outgoing links of the source node point to perturbed nodes including the target node (left panel) or if all outgoing links of source node and target node point to perturbed nodes, with the target node not perturbed (right panel). **b** Fraction of inferable links against the fraction of perturbed nodes using three network types: (i) scale-free network with exponent $\gamma = 2.5$ and mean degree $\langle k \rangle = 3$, where nodes of higher degree target nodes of lower degree (outgoing hubs), (ii) same network as (i) but with all link directions inverted (incoming hubs) or a network generated by random insertion of links with the same mean degree as scale-free networks (random network). Colour coding as in **c**. **c** Network inferability versus mean degree, using networks of **b**. **d** Network inferability versus scaling exponent for two types of scale-free networks. **e** Asymptotic invariance of the two inferability measures introduced in the main text with respect to network size. **f** Network inferability as a function of mean degree for social and biological networks. Correlation between the two inferability measures introduced in the main text (inset)

transmitting information back to it, as we exclude bidirectional links from our analysis. This makes the network (Fig. 1a, left network) fully inferable, as the link between the remaining two perturbed nodes can be inferred by collecting experiments for which the target node is unperturbed. We emphasise that our approach to network inferability does not account for a priori known restrictions on the network topology, as in the case of directed acyclic graphs. Such constraints can strongly increase the inferability of directed links[8].

As $F(q)$ is an upper bound for the expected number of directed links that can be inferred from stationary node activities in the absence of noise and other constraints on the network structure, we now ask how this bound is related to the structural properties of the network. To compare different network architectures, it is useful to define the network inferability, I_F, as the area under the $F(q)$-curve, $I_F := \int_0^1 F(q)\mathrm{d}q$. Comparison of I_F between two general classes of network structures with node degrees either power law or Poisson distributed shows that networks that are enriched with nodes of high outdegree are the most difficult ones to infer (Figs 1b and 2b). The reason is that whenever hubs with high outdegree are perturbed there is a high chance that they target more than one of the unperturbed nodes and without additional perturbations it is impossible to detect which of the targets are affected directly and which indirectly. Differences in inferability due to network structure are most predominant for networks with low mean degree and become less predominant with high mean degree (Fig. 2c). As our measure of inferablity, I_F, is essentially determined by the outdegree distribution, the curve

starts saturating for scale-free exponents $\gamma > 3$, as in this regime the variance of the number of links per node is essentially constant for increasing γ and fixed mean degree[9] (Fig. 2d). The network inferability, I_F, is asymptotically independent of network size (Fig. 2e). We further investigated the inferability of causal interactions in biological and social networks as a function of the mean degree (Fig. 2f). The decreasing trend can be explained by the higher number of alternative routes that come with a more strongly connected network. The low inferability of gene-regulatory networks can be attributed to master regulators that regulate a large fraction of the genome (hubs with high outdegree), whereas the comparatively high inferability of protein interaction networks is a consequence of the low number of different binding domains per protein and that only a fraction of the existing interactions have been identified due to limitations of experimental methods[10]. If we assume that the conditional probability $P(k, l, m|k \to l)$ of finding two connected nodes in the directed network, where the source node has $k \geq 1$ outgoing links, the target node has $l \geq 0$ outgoing links, and both share m nodes as common targets of their outgoing links, can be factorised, the resulting inferability measure, I_F^*, is simply a function of the outdegree distributions, $P(k)$ and $P(l)$. We observed that $I_F^* \approx I_F$ for all networks investigated in this work (Fig. 2f, inset). This result shows that for a large variety of networks structures the outdegree is the dominating factor that determines network inferability. Consequently, if the perturbed nodes are not selected at random but are biased towards higher outdegree, inferability is further reduced.

Network inference concepts. From our analyses of network inferability we gained the insight that the number of potential alternative routes how a source node can affect a target node correlates positively with the outdegree of the source node and inversely with the expected inferability of the directed link between source and target, given that perturbed nodes are uniformly distributed in the network. Consequently, network inference algorithms should strongly benefit from an a priori reduction in the number of alternative routes. In the following we present an unbiased network inference algorithm that eliminates alternative routes with low signal-to-noise ratio as a preprocessing step. Inference of transcriptional networks on genome scale is best realised by methods that are (i) asymptotically unbiased, (ii) scalable to large network sizes, (iii) sensitive to feed-forward loops[11] and (iv) can handle data sets with and without knowledge about which nodes are targeted by experimentally induced perturbations[7, 12–16] (Supplementary Note 2). Inference methods for directed networks typically require individual perturbation of all nodes[7] or many perturbations of different strengths to compute conditional association measures[6, 17] or conditional probabilities[18]. Generation of time course data seems to be the most natural way to infer directed networks by simply analysing the temporal ordering of the transcriptional activities[19, 20]. However, this approach precludes the use of knockout experiments and requires fast acting perturbations in combination with monitoring node activities over time, which is experimentally demanding, especially if nodes respond on very different time scales[21].

Experimental variability and technical noise. Inference is further complicated by the fact that transcriptome data contain a significant amount of stochastic variation between biological replicates despite pooling over millions of cells (Fig. 3a). It is interesting to see that the variation across biological replicates for baker's yeast[3] is close to a normal distribution and follows almost exactly a t-distribution with 11 degrees of freedom over five standard deviations (Fig. 3a, inset). The same data set also shows

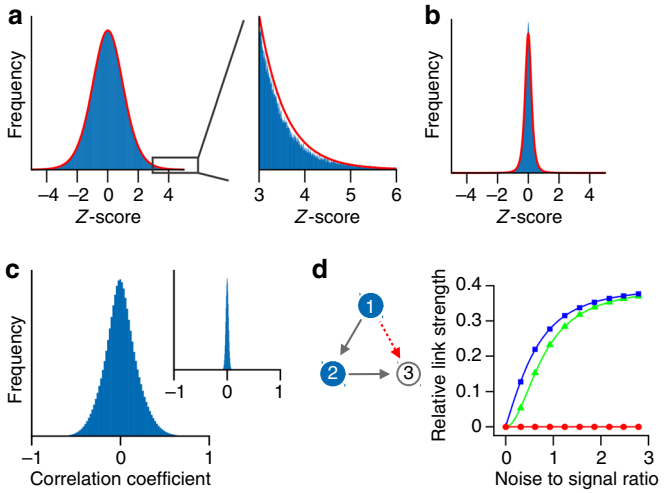

Fig. 3 Distribution of wild-type expression levels for *S. cerevisiae* from 748 biological replicates. **a** Distribution of the relative expression, $\log_2(r_i)$, with $r_i := x_i/x_i^{pool}$ and x_i the expression of gene i relative to x_i^{pool} followed by standardisation of the $\log_2$ fold changes (z-score). The values x_i^{pool} have been obtained by first pooling the 748 biological replicates before measuring gene expression. The distribution is well described within five standard deviations by a t-distribution with 11 degrees of freedom (red line). **b** Distribution as in **a** but now for differences among technical replicates. **c** Correlation between gene expression levels is significantly higher than expected by chance (inset) **d** Illustration of a noise induced false positive link (red arrow) as described in the main text. Data for a three-node network with two links was generated by applying independent perturbations on node 1 and node 2. The link strength of the non-existing link from node 1 to node 3 relative to the existing link from node 2 to node 3 was inferred using three different methods (i) partial correlations (blue squares), (ii) conditional mutual information (green triangles) and PRC (red circles)

that variability among biological replicates is much larger than technical noise (Fig. 3b) for this experimental setup. As variability among biological replicates may arise from subtle differences in growth conditions that induce changes in gene regulation, we expected to see significant cross-correlations among genes (Fig. 3c), whose magnitude is much larger than expected by chance (Fig. 3c, inset). These cross-correlations can be exploited for inferring the structure of undirected networks[12], if the driving noise is independent and identically distributed for all nodes (Supplementary Note 2). In contrast, technical noise not only reduces the statistical significance for detecting true interactions but can also induce a significant fraction of false positive interactions, especially if the interaction network under investigation is sparse. Such noise induced misclassification of links can be illustrated by a simple linear network $A \to B \to C$ for which standard inference methods—such as partial correlations–interpret the information that A has about C erroneously as a direct link between A and C if the state of B is corrupted by measurement noise (Fig. 3d). The reason is that a part of the correlation between A and C cannot be explained by B.

Algorithm for large-scale and unbiased network inference. To make use of the rapidly growing amount of single-gene knockout screens for which transcriptome data are[3] or may become available[22, 23], we developed a method to infer directed networks on a genome scale, where the number of genetic perturbations is typically below the number of nodes or genes in the network (Online Methods). In brief, our method uses the concept of

probabilistic principle component analysis[24] to compute partial response coefficients (PRC) that are asymptotically unbiased with respect to Gaussian measurement noise. In addition, the algorithm provides a feature to identify non-inferable links, which are removed before statistical analysis. In the absence of noise, our numerical method correctly predicts the fraction of links that are inferable, $F(q)$ (Supplementary Note 1), for a network with links represented by linear functions of slope one. To evaluate the performance of our method we generated two synthetic knockout data sets that closely resemble the gene-regulatory network structure of baker's yeast, using the GeneNetWeaver software[25] that uses a hierarchical network structure and our own generative model that uses a scale-free network structure (Supplementary Note 3). We added Gaussian measurement noise to the synthetic data with a standard deviation of 10% the $\log_2$ fold-change in expression level for each perturbation for each gene. Residual bootstrapping among replicates was used to quantify the statistical significance of the inferred link strengths. In comparison with standard inference methods, such as partial correlations[12–14, 26, 27], our method shows a significantly higher performance in the absence of any penalties that enforce sparse network structures (Fig. 4b, left panel). The improved performance of our approach can be assigned to the fact that the method is unbiased with respect to measurement noise (Online Methods).

To further improve the predictive power of our method we included the prior knowledge that transcriptional networks are highly sparse. Sparsity constraints are typically realised by penalising either the existence of links or the link strengths by adding appropriate cost functions, such as L^1-norm regularised regression (Lasso)[28]. Adding a cost function to the main objective comes with the problem to trade-off the log-likelihood against the number of links in the network whose strength is allowed to be non-zero. In the absence of experimentally verified interactions there is no obvious way how to determine a suitable regularisation parameter that weights the likelihood against the cost function, which is one of the great weaknesses of such methods.

In our approach we reduce network complexity by assuming that functionally relevant information in molecular networks can only pass through nodes whose response to perturbations is significantly above the base line that is given by the variability among biological replicates. The individual noise levels can be estimated from natural variations among wild-type experimental replicates (Fig. 3a). The significance level that removes nodes from the network with low signal-to-noise ratio can be set to a desired false discovery rate. It can be shown that removal of noisy nodes imposes a sparsity constraint on the inference problem (Online Methods). The different steps required to arrive at a list of significant links are illustrated in Fig. 4a. In the first step, genes are grouped in clusters that are co-expressed under all perturbations. These clusters are treated as single network nodes in the subsequent steps. In the second step, only those samples are extracted from the data set that correspond to a perturbation of a chosen gene—the source node—with no other genes perturbed (node 5 in Fig. 4a). From this reduced data set, we identify all nodes in the network that change expression above a given significance level upon perturbing the source node. These significantly responding nodes define a subnetwork for each source node, which is typically much smaller in size than the complete network. In the third step, we collect all perturbation

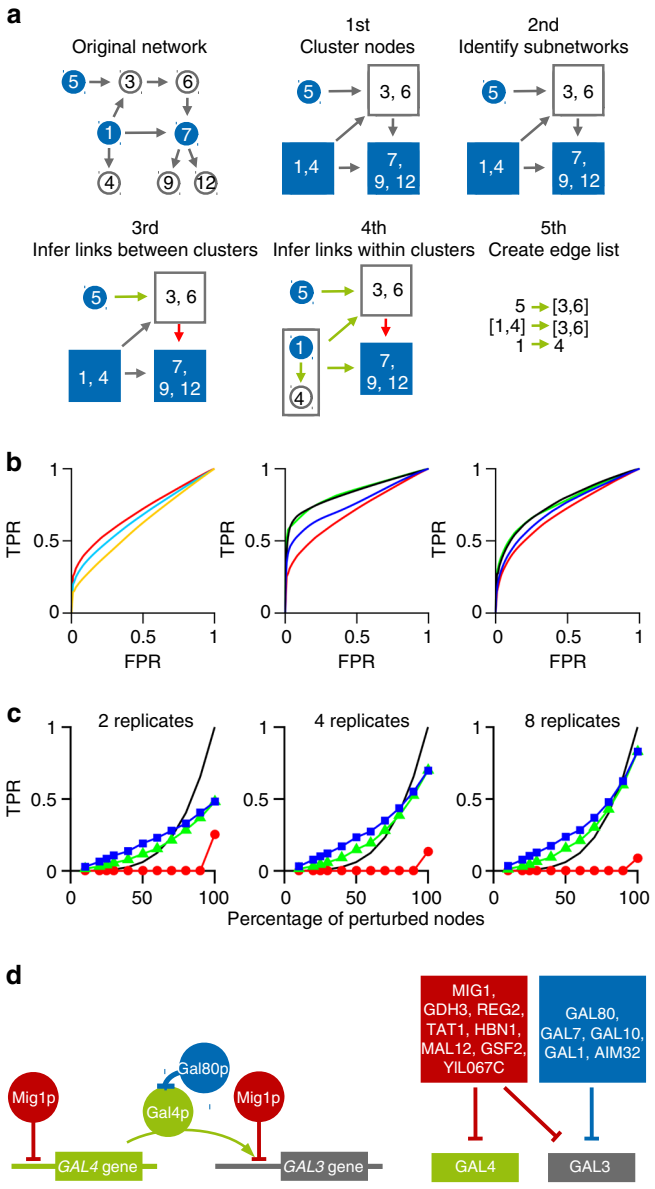

Fig. 4 Performance of our method. **a** Flow-chart showing the algorithmic steps for network inference as explained in the main text. **b** Receiver Operating Characteristic (ROC) curves for 300-node scale-free networks with additive Gaussian measurement noise of 10% of the expression level and 25% of the nodes perturbed. Data were generated using GeneNetWeaver (left and middle panel) as well as using scale-free network structure with mean degree of $\langle k \rangle = 2$ and scaling exponent $\gamma = 2.5$ (right panel, Supplementary Note 3). Here, the true positive rate is computed with respect to the inferable links[39]. Performance of inference methods without sparsity constraints (left panel): PRC (red), partial correlations/linear regression (turquoise) and conditional mutual information (orange). Performance of inference methods with sparsity constraints (middle and right panel): PRC with subnetwork method (green) and Lasso (black) both applied to a subset of significantly responding nodes that were selected with 1% false discovery rate, Lasso regression applied to all 300 nodes (blue), and PRC from left panel (red) for comparison. **c** True positives for the same scale-free network of **b**, with 2, 4 and 8 experimental replicates with 5% false discovery rate for both significantly responding nodes and link strength: PRC (red), PRC with subnetwork method (green), PRC with subnetwork and clustering method (blue), and $F(q)$ (black line). **d** The *S. cerevisiae* GAL network as an example for a gene-regulatory network where phosphorylated Mig1 sets the basal expression levels of Gal4 and one of its many regulatory targets, Gal3. Gal4 protein can activate Gal3 expression but is inactivated upon binding of Gal80 protein. The transcriptome data set contains knockout mutants for GAL80 and MIG1 but not for the remaining GAL genes. A schematic representation of the key molecular mechanisms (left) and links inferred from transcriptome data[3] (right)

data from the complete data set for all nodes that are part of the subnetwork. Before inferring a direct interaction that points from the source node to a given target node in the subnetwork (green arrows in Fig. 4a), we remove all experiments from the data set where the target node is perturbed. The second and third steps essentially realise the counting procedure of inferable links as illustrated in Fig. 2a, with the difference that significant links are identified by PRCs in combination with residual bootstrapping over replicates (Online Methods, Supplementary Note 3). In the fourth step, we collect all clusters of co-expressed genes that contain exactly two nodes, with one of the nodes perturbed and check statistical significance of the directed link between them. In the fifth step, all significant links are collected in an edge list. We refer to these five steps as the clustering method. If we remove all links from the edge list that have more than one node in a source cluster or more than one node in a target cluster, we obtain an edge list that corresponds to links between single genes. This reduced edge list would also arise by skipping the clustering step and we refer to the remaining inference steps that compute links between single genes as subnetwork method.

Performance of the proposed inference algorithm. The Lasso method in combination with bootstrapping has been benchmarked as one of the highest performing network inference methods for in silico generated expression data[29]. The receiver operating characteristic (ROC) curve of the subnetwork method shows better performance than the Lasso method (Fig. 4b, middle and right panel) after adjusting the regularisation parameter of the Lasso method such that the area under the ROC curve is maximised. However, a significant performance boost for the Lasso method can be achieved by applying the second step of our method that removes noisy nodes, resulting in comparable performance of Lasso with the subnetwork method for the case that validation data exist such that the regularisation parameter can be determined (Fig. 4b, middle and right panel).

To get insight into the optimal experimental design for generating data for network inference, we computed the fraction of correctly inferred links and compared them against the fraction of independently perturbed nodes for different numbers of experimental replicates. We compared three different variants of our approach: PRC, PRC together with subnetwork method and PRC together with clustering method (Fig. 4c). As all variants share PRC as underlying inference method (Online Methods), the observed strong increase in performance can be assigned to the sparsity constraint that comes with the subnetwork method or the clustering method. Owing to this constraint, both the subnetwork method and the clustering method can have higher accuracy than the noise-free analytical solution, as the latter does not enforce sparse network structures. The results show that in the presence of 10% measurement noise the amount of available replicates limits the true positive rate, even if 100% of nodes are perturbed. Inference of >80% of the network can only be achieved if the number of replicates is sufficiently high.

To benchmark the performance of our algorithms in comparison to others, we applied our method to the DREAM3 in silico network inference challenge[30]. The provided data set of this challenge has the advantage that full information about the identity of perturbed nodes is given. We ignored the transient information from time series and used the stationary state of time course data to estimate the variation in expression between biological replicates. To identify the significantly responding nodes, we used a Bonferroni corrected significance level of $\alpha = 0.05/N$, where the number of alternative hypotheses—or the number of possible incoming links for a given target node in our case–are bounded by number of possible source nodes in the network, $N-1$. To make sure that we correctly implemented the published performance evaluation method that is based on curve fitting a sampled null hypothesis[31], we followed the proposed curve fitting procedure suggested by the organisers of the challenge by using different exponential family distributions for each tail, and alternatively by using a single t-distribution to fit AUROC null hypothesis samples. The results are shown in Table 1 and Supplementary Data 4. The overall second place among the other 29 inference methods should be interpreted in the light that the better performing algorithm uses extensive hyperparameter tuning, makes use of transient data, and does not scale well with network size[32]. Furthermore, our approach seems to be robust with respect to the chosen significance level as changing α by one order of magnitude did not affect the ranking. However, we emphasise that for 'large p small n' problems, where the number of parameters exceeds the number of independent data points, preprocessing often has a larger effect on performance than the inference method itself[30]. For our algorithm the performance boost is a consequence of generating subnetworks as preprocessing step.

Application to yeast genome knockout data. To evaluate the performance of our approach on real data, we use one of the largest publicly available transcriptome data sets[3], comprising of transcriptomes that cover 6170 genes for 1441 single-gene knockouts that can be utilised for network inference using PRC. We use the galactose utilisation network as a gene-regulatory example, which is one of the best characterised gene-regulatory modules in yeast[33]. The regulatory mechanism of the GAL4 gene as a key regulator is shown in Fig. 4d, left panel. As information about phosphorylation and protein interaction is absent in expression data, the inferred network structure from transcriptome data with GAL4 and GAL80 perturbed is different from the known gene regulation but can identify major regulators and their targets. Whether the gene AIM32—which is not known to be part of the GAL network—is co-regulated with GAL80 or an artefact of the knockout screen is difficult to judge. Both options are possible as AIM32 is located in close vicinity to GAL80 on the genome. By sorting genes with respect to their number of statistically significant outgoing links, we can identify potential key regulators. Besides transcription factors, the regulators with highest statistical significance are factors involved in chromatin remodelling, signalling kinases, and genes involved in ubiquitination (Supplementary Data 1–3). This result—although expected for eukaryotes—is inaccessible for inference methods

Table 1 Ranking and overall scores (in parantheses) among the original participants of the DREAM3 in silico network inference challenge

	10 nodes $\alpha = 0.05/10$	50 nodes $\alpha = 0.05/50$	100 nodes $\alpha = 0.05/100$
Original scoring method	2nd (4.64)	2nd (31.43)	2nd/1st (55.98)
AUROC background fitted with t-distribution	2nd (4.14)	3rd (30.10)	2nd/1st (50.06)

Scores were obtained with the original scoring method and a scoring method in which the AUROC background distribution was fitted with a t-distribution. Here, α denotes the significance level for the identification of nodes that are significantly affected by perturbations

that a priori fix known transcription factors as regulatory sources. However, as the number of deleted genes in this data set comprise just 23% of the genes for which transcript levels have been measured, we can estimate from our simulations that we have inferred <10% of the direct interactions in the transcriptional network of yeast.

Discussion

We have developed an unbiased network inference method for perturbation experiments that target individual nodes in the network. Consequently, node activity data that result from unspecific perturbations cannot be exploited by this algorithm in its present form. As individual gene knockout or knockdowns dominate many large-scale experimental studies of node activities in biological networks[3, 23] and their genome-wide coverage is constantly improving[22, 34], we expect that the biological data sets to which the algorithm can be applied will rapidly increase in the near future. However, currently most of the large-scale knockout or knockdown screens lack complete coverage of mutants and often come with low number of experimental replicates, if any. In this work we have shown that insufficient coverage of perturbed nodes in transciptome data fundamentally limit the amount of links that can be inferred, independently of the employed inference algorithm and that high statistical power requires a significant amount of replicates to drive down effects of experimental variability and measurement noise. We therefore introduced a network inference approach that is able to detect significant links for the case that only a fraction of nodes are perturbed, removes nodes with low signal-to-noise ratio from the network, and makes use of an inference algorithm that is insensitive to measurement noise. Including prior knowledge about network complexity and reducing the effects of noise is crucial for network inference problems, where the number of parameters, e.g., link strengths, scale quadratically with network size and often exceed the number of measured data points. Good scaling behaviour and the absence of time-consuming hyperparameter tuning make our approach an easily applicable network inference tool that shows competitive performance with state-of-the-art methods. However, even when complete coverage of single-gene perturbations together with a high number of experimental replicates of transcriptome data are available, the inferred transcriptional network cannot be directly translated into a model that reflects the biochemical reality of gene regulation. The reason is that gene regulation can involve complex molecular interactions on DNA, RNA, protein and small molecule level that result in direct interactions between mRNA levels. An example of such complex interactions is the observed regulation by the human oncogene IDH1—a metabolic enzyme involved in the citric acid cycle. Mutational loss of normal enzymatic function of IDH1 and production of the metabolite 2-hydroxyglutarate can affect the activity of an epigenetic regulator, which promotes tumorgenesis by reprogramming transcriptional activity on genome scale[35]. Inference of such complex molecular interactions would require a combination of different high-throughput technologies, with the challenge that different methods typically show large differences in sensitivity and coverage[36].

Methods

PRC. We aim at inferring direct interactions between N observable molecular components, such as transcripts or proteins, by measuring their concentrations. We define by $\boldsymbol{y} \in \mathbb{R}^N$ an N dimensional vector that represents the logarithm of these concentrations, which is the natural scale where experimental data are reported. We assume that the available data set has been generated from P perturbation experiments, $\{\boldsymbol{y}_k\}_{k=1}^P$, which may also include experimental replicates. We further assume that the molecular targets of the perturbations are known, as it is the case for gene knockout or knockdown experiments. The elements of the interaction matrix $\boldsymbol{A} \in \mathbb{R}^{N\times N}$ define the strengths of the directed interactions among the molecular components, for example, A_{ij} quantifies the direct impact of component j on component i. Given the available experimental data, our aim is to correctly classify the off-diagonal elements of $\boldsymbol{A}$ as zero or non-zero to obtain the structural organisation of the interaction network. We assume that the observed component abundance on log-scale, $\boldsymbol{y}^{obs}$, differs from the true value, $\boldsymbol{y}$, by additive measurement noise, ϵ, which is characterised by zero mean, $\mathbb{E}[\epsilon] = 0$, and variance, $\mathbb{E}[\epsilon\epsilon^T] = \sigma^2\boldsymbol{I}_N$, with $\boldsymbol{I}_N$ the N dimensional identity matrix. We assume that the observed data can by described to sufficient accuracy by a linear stationary model

$$\begin{aligned} 0 &= \boldsymbol{A}\left(\boldsymbol{y} - \boldsymbol{y}^{ref}\right) + \boldsymbol{B}\boldsymbol{u} \\ \boldsymbol{y}^{obs} &= \boldsymbol{y} + \epsilon, \end{aligned} \tag{1}$$

with $\boldsymbol{A}$ negative definite to ensure stability. Equations of this type typically arise from linear expansion of a non-linear model around a reference state, $\boldsymbol{y}^{ref}$. Linear models are usually preferred for network inference a on larger scale, as the amount of data often limit model complexity and the fact that linear models can give surprisingly good resuits for non-linear cases. The perturbation vector $\boldsymbol{u}$ reflects perturbations that persist long enough to propagate through the network, such as mutations that affect gene activity. Here, $\boldsymbol{u}$ is defined such that for $\boldsymbol{u} = 0$ the system approaches the reference state $\boldsymbol{y} = \boldsymbol{y}^{ref}$. Note that the reference state, $\boldsymbol{y}^{ref}$ is not necessarily the unperturbed state but could be also defined as the average over perturbed and unperturbed states. We assume that the perturbation forces are sampled from a standard normal distribution, with mean $\mathbb{E}[\boldsymbol{u}] = 0$ and covariance matrix $\mathbb{E}[\boldsymbol{u}\boldsymbol{u}^T] = \boldsymbol{I}_N$. The identity matrix is a consequence of the fact that we can absorb the associated standard deviations of the perturbative forces, $\boldsymbol{u}$, in the matrix $\boldsymbol{B} \in \mathbb{R}^{N\times N}$. We introduce normal distributed perturbations for mathematical convenience, as this implies that also $\boldsymbol{y}$ is normal distributed and the resulting maximum likelihood approach is analytically solvable. In general, only the positions of the non-zero elements of $\boldsymbol{B}$ are known from the experimental setup but their actual values are unknown. Using a linear model that operates on log-scale of physical quantities implies that only perturbations can be modelled that act multiplicatively on molecular concentrations. Fortunately, most enzymatic reactions typically fall into this class, such as sequestration and inhibition by other components and also knockout and knockdown experiments can be described on multiplicative level. From Eq. (1) we can derive a relation between the interaction matrix $\boldsymbol{A}$ and the covariance matrix of observed component abundances

$$\begin{aligned} \boldsymbol{C} &:= \mathbb{E}\left[\left(\boldsymbol{y}^{obs} - \boldsymbol{y}^{ref}\right)\left(\boldsymbol{y}^{obs} - \boldsymbol{y}^{ref}\right)^T\right] \\ &= \boldsymbol{A}^{-1}\boldsymbol{B}\boldsymbol{B}^T\boldsymbol{A}^{-T} + \sigma^2\boldsymbol{I}_N \end{aligned} \tag{2}$$

We exploit Eq. (2) to infer directed networks from correlation data. Here, we assume that component abundances are obtained from averaging over a large number of cells. In this case, fast fluctuating perturbations that arise from thermal noise and can be observed only on single-cell level average out. To infer the interaction matrix, $\boldsymbol{A}$, we start with singular value decomposition of the matrix product $\boldsymbol{A}^{-1}\boldsymbol{B}$

$$\boldsymbol{U}\boldsymbol{\Sigma}\boldsymbol{V}^T := \boldsymbol{A}^{-1}\boldsymbol{B} \quad \Rightarrow \quad \boldsymbol{B} = \boldsymbol{A}\boldsymbol{U}\boldsymbol{\Sigma}\boldsymbol{V}^T \tag{3}$$

with $\boldsymbol{U}$ and $\boldsymbol{V}$ orthogonal matrices and $\boldsymbol{\Sigma}$ a diagonal matrix containing the singular values. The negative definite matrix $\boldsymbol{A}$ has full rank and hence is invertible. In the following, we show that it is possible to infer the strength of a directed link between a sender node j and a receiver node i, if all direct perturbations on receiver node i are removed from the data set and if a significant partial correlation between i and j exists. Removing the perturbation data for node i implies that the matrix $\boldsymbol{B}$ has at least one zero entry. As a consequence, $N_0 \geq 1$ singular values are zero–as in general not all nodes are perturbed–and the corresponding rows of $\boldsymbol{U}$ span the left null-space of $\boldsymbol{A}^{-1}\boldsymbol{B}$. In the absence of fast fluctuating perturbations, $\gamma = 0$, we can rewrite the covariance matrix as

$$\boldsymbol{C} = \boldsymbol{A}^{-1}\boldsymbol{B}\boldsymbol{B}^T\boldsymbol{A}^{-T} + \sigma^2\boldsymbol{I}_N \tag{4}$$

$$= \boldsymbol{U}(\boldsymbol{\Sigma}^2 + \sigma^2\boldsymbol{I}_N)\boldsymbol{U}^T. \tag{5}$$

Assuming that the observed node activities follow a multivariate normal distribution, we can find estimates for the unknown orthogonal matrix $\boldsymbol{U}$, the singular values $\boldsymbol{\Sigma}$, and the observational noise σ by maximising the log-likelihood function $\mathcal{L}$ under the constraint $\boldsymbol{U}_l^T\boldsymbol{U}_k = \delta_{lk}$, with $\boldsymbol{U}_k$ the k-th column vector of $\boldsymbol{U}$ and δ_{lk} the Kronecker delta. It fact, it suffices to constrain the norm of the vectors, $\|\boldsymbol{U}_k\|$, as the corresponding maximum likelihood solution leads to an eigenvalue problem with $\boldsymbol{U}_k$ as eigenvectors, which can always be made orthogonal. We can therefore define the likelihood function by

$$\mathcal{L} := \ln \prod_{n=1}^{P} \mathcal{N}\left(\boldsymbol{y}_n^{obs} | \boldsymbol{y}^{ref}, \boldsymbol{C}\right) + \sum_{k=1}^{N} \lambda_k\left(\boldsymbol{U}_k^T\boldsymbol{U}_k - 1\right) \tag{6}$$

$$= -\tfrac{P}{2}\{M\ln 2\pi + \ln|\boldsymbol{C}| + \mathrm{tr}(\boldsymbol{C}^{-1}\boldsymbol{S})\} + \sum_{k=1}^{N} \lambda_k\left(\boldsymbol{U}_k^T\boldsymbol{U}_k - 1\right) \tag{7}$$

Here, $\boldsymbol{S} := \frac{1}{P}\sum_{n=1}^{P}\left(\boldsymbol{y}_n^{obs} - \boldsymbol{y}^{ref}\right)\left(\boldsymbol{y}_n^{obs} - \boldsymbol{y}^{ref}\right)^T$ and $\boldsymbol{y}^{ref} := \frac{1}{P}\sum_{n=1}^{P}\boldsymbol{y}_n^{obs}$ denote maximum likelihood estimates of the covariance matrix[37]. From this definition of $\boldsymbol{y}^{ref}$ follows that the initially introduced perturbation vector, $\boldsymbol{u}$, must satisfy, $\frac{1}{P}\sum_{n=1}^{P}\boldsymbol{u}_n = \boldsymbol{0}$. We further defined with λ_k a Lagrange multiplier and denoted by tr(.) the trace of a matrix. In the following calculations, we substitute $\boldsymbol{S}$ by the unbiased sample covariance matrix, $\boldsymbol{S} \to P(P-1)^{-1}\boldsymbol{S}$. Note that $\boldsymbol{V}$ must disappear in the likelihood function as the covariance matrix of $\boldsymbol{u}$ is invariant under any orthogonal transformation $\boldsymbol{u} \to \boldsymbol{V}^T\boldsymbol{u}$.

The maximum of the log-likelihood function is determined by the conditions $\mathrm{d}\mathcal{L}/\mathrm{d}\boldsymbol{U}_k = 0$, $\mathrm{d}\mathcal{L}/\mathrm{d}\boldsymbol{\Sigma}_{kk} = 0$, and $\mathrm{d}\mathcal{L}/\mathrm{d}\sigma^2 = 0$, which results in

$$\boldsymbol{S}\hat{\boldsymbol{U}}_k = \Lambda_k\hat{\boldsymbol{U}}_k \quad \text{with } \Lambda_1 \le \Lambda_2 \le \ldots \le \Lambda_N \tag{8}$$

$$\hat{\sigma}^2 = \frac{1}{N_0}\sum_{k=1}^{N_0}\Lambda_k \tag{9}$$

$$\hat{\Sigma}_{kk} = \begin{cases} \sqrt{\Lambda_k - \sigma^2} & \text{for} \quad k > N_0 \\ 0 & \text{for} \quad k \le N_0 \end{cases} \tag{10}$$

showing that maximum likelihood estimates of $\hat{\boldsymbol{U}}$, $\hat{\sigma}^2$, and $\hat{\boldsymbol{\Sigma}}$ are determined by the sample covariance matrix $\boldsymbol{S}$. If $N_0 > 1$ and the full-rank sample covariance matrix is significantly different from a block-diagonal form—e.g., the network is not separable in subnetworks–the orientations of the corresponding N_0 eigenvectors are determined by sampling noise in the space orthogonal to remaining $N - N_0$ eigenvectors. In case that we have less data points than nodes in the network—e.g., the number of perturbed nodes times their replicates is smaller than the network size—some of the N_0 smallest eigenvalues become exactly zero and as a consequence the noise level, $\hat{\sigma}$, is underestimated. Although a maximum likelihood solution exists in this case, it is necessary to regularise the covariance matrix, $\boldsymbol{S} \to (1-\epsilon)\boldsymbol{S} + \epsilon\boldsymbol{I}_N$, with ϵ a regularisation parameter[37], as a correct estimate of the noise level is essential for statistical analysis. Note that the derivation of the maximum likelihood solution is mathematically equivalent to the derivation of principle component analysis from a probabilistic perspective[24].

Solving the matrix equation, Eq. (3), for $\boldsymbol{A}$ gives

$$\boldsymbol{A} = \left(\boldsymbol{B}\boldsymbol{V}\boldsymbol{\Sigma}^{+} + \boldsymbol{W}\boldsymbol{\Sigma}^{0}\right)\boldsymbol{U}^T \tag{11}$$

with $\boldsymbol{\Sigma}^{+}$ the pseudoinverse of $\boldsymbol{\Sigma}$. As the matrix $\boldsymbol{A}$ has full rank, we complement $\boldsymbol{\Sigma}^{+}$ with an unknown diagonal matrix $\boldsymbol{\Sigma}^{0}$ that has non-zero values where $\boldsymbol{\Sigma}^{+}$ has zero values and vice versa and complement $\boldsymbol{BV}$ with an unknown orthogonal matrix $\boldsymbol{W}$. Note that by construction, $\boldsymbol{\Sigma}^{+}\boldsymbol{U}^T$ and $\boldsymbol{\Sigma}^{+}\boldsymbol{U}^T$ map from complementary subspaces and thereby ensure that $\boldsymbol{A}$ has full rank. The fact that $\boldsymbol{V}$, $\boldsymbol{W}$ and $\boldsymbol{\Sigma}^{0}$ cannot be determined from $\boldsymbol{S}$ shows that $\boldsymbol{A}$ cannot be computed from a single covariance matrix. A more general case arises when measurement noise is independent but not isotropic, $\sigma^2\boldsymbol{I} \to \sigma^2\boldsymbol{D}$, with $\boldsymbol{D} = \mathrm{diag}(r_1, r_2, \ldots, r_N)$ a diagonal matrix with known positive elements that contains scaled noise variances, $r_i := \sigma_i^2/\sigma^2$, resulting in

$$\boldsymbol{C} = \boldsymbol{A}^{-1}\boldsymbol{B}\boldsymbol{B}^T\boldsymbol{A}^{-T} + \sigma^2\boldsymbol{D} \tag{12}$$

A transformation to isotropic noise is possible by multiplying both sides of Eq. (12) by $\boldsymbol{D}^{-\frac{1}{2}}$, which changes the result Eq. (11) to

$$\boldsymbol{A} = \left(\boldsymbol{B}\boldsymbol{V}\boldsymbol{\Sigma}^{+} + \boldsymbol{W}\boldsymbol{\Sigma}^{0}\right)\boldsymbol{U}^T\boldsymbol{D}^{-\frac{1}{2}} \tag{13}$$

with $\boldsymbol{U}$ the eigenvectors of $\boldsymbol{D}^{-\frac{1}{2}}\boldsymbol{S}\boldsymbol{D}^{-\frac{1}{2}}$.

Case $N_0 = 1$. We assume that the i-th node is the only unperturbed node in the network and hence set $B_{il} = 0$ for all l. From Eq. (11) we obtain a unique solution for the i-th row of $\boldsymbol{A}$ relative to the diagonal element, A_{ii},

$$\frac{A_{ij}}{A_{ii}} = \frac{\sum_{k,l=1}^{N} B_{il}V_{lk}\Sigma_{kk} + \sum_{k=1}^{N} W_{ik}\Sigma_{kk}^{0}U_{kj}^T}{\sum_{k,l=1}^{N} B_{il}V_{lk}\Sigma_{kk} + \sum_{k=1}^{N} W_{ik}\Sigma_{kk}^{0}U_{ki}^T} = \frac{U_{kj}^T}{U_{ki}^T}\bigg|_{k=1} = \frac{U_{j1}}{U_{i1}} \tag{14}$$

with U_{j1} the j-th element of the eigenvector that has the smallest eigenvalue. Note that the first term in the brackets vanishes as $B_{il} = 0$ and Σ_{11}^{0} is the only non-zero element of $\boldsymbol{\Sigma}^{0}$. The important point is that any dependency on σ–which affects eigenvalues but not eigenfunctions–has dropped out, making this method asymptotically unbiased with respect to measurement noise. The fact that we can determine the elements of the i-th row of $\boldsymbol{A}$ only relative to a reference value, A_{ii}, is rooted in fact that we have to determine the N parameters $\{A_{i1}, \ldots, A_{ii}, \ldots, A_{iN}\}$ from $N-1$ perturbations. As a consequence, the strengths of the links onto the target nodes cannot be compared directly if their restoring forces or degradation rates, A_{ii}, are different. Generally, only relative values of $\boldsymbol{A}$ can be determined, as the average perturbation strength on node i cannot be disentangled from its restoring force A_{il}–a problem that is typically circumvented by defining $A_{ii} := -1$ for all i[7, 13, 15]. For the case that all nodes in the network are perturbed one-by-one, we can cycle through the network and remove the perturbations that act on the current receiver node, whereas keeping the perturbations on the remaining nodes. By computing the N corresponding covariance matrices and their eigenvectors, we can infer the complete network structure from Eq. (14) if the data quality is sufficiently high. Note that the method makes use of the fact that multi-node perturbations can be realised by superposition of single-node perturbations, which is a special property of linear models.

Case $N_0 > 1$. If more than one node are not perturbed we get from Eq. (11)

$$\frac{A_{ij}}{A_{ii}} = \frac{\sum_{k=1}^{N_0} W_{ik}\Sigma_{kk}^{0}U_{kj}^T}{\sum_{k=1}^{N_0} W_{ik}\Sigma_{kk}^{0}U_{ki}^T} \tag{15}$$

Non-unique solutions of Eq. (15) can arise if a given fraction of the variance of the receiver node i can be explained by more than one sender node, for example, when a perturbed node j targets two nodes with index i and l. In this case it is unclear from the node activity data whether i is affected directly by j or indirectly through l, or by a combination of both routes. If node l is not perturbed or only weakly perturbed, a statistical criterion is needed to decide about inferability or identifyability of the link $j \to i$, which can be computed numerically as follows: To find out whether j transmits a significant amount of information to i that is not passing through l, we first remove node j from the observable nodes of the network but keep its perturbative effect on other nodes in the data set. We then determine the link strengths $\boldsymbol{A}'$ for the remaining network of size $N-1$. To construct a possible realisation of $\boldsymbol{A}'$ we set in Eq. (15) the non-zero values of $\boldsymbol{\Sigma}^{0}$ to unity and use $\boldsymbol{W} = \boldsymbol{U}$ to arrive at the expression

$$\frac{A'_{il}}{A'_{ii}} = \frac{\sum_{k=1}^{N_0} U'_{ik}U'_{lk}}{\sum_{k=1}^{N_0} U'_{ik}U'_{ik}} \tag{16}$$

with $\boldsymbol{U}'$ determined from the sample covariance matrix with the j-th column and j-th row removed. Fixing $\boldsymbol{W}$ and $\boldsymbol{\Sigma}^{0}$ to seemingly arbitrary values does not affect the result we are after. If l is the only unperturbed node besides i, then in the A' system l can now be treated as perturbed—as it may receive perturbations from the unobserved node j—and thus Eq. (14) applies. If l is part of many unperturbed nodes that are affected by j, then the knowledge how much each of these nodes contributes to the variance of the target node i (which is determined by $\boldsymbol{W}$ and $\boldsymbol{\Sigma}^{0}$) is irrelevant as we are only interested in the total effect of the alternative routes on node i. Using the inferred link strength from Eq. (16) we can rewrite Eq. (2) as a two-node residual inference problem between j and i, where we obtain a lower bound for link strength from node j to i by using the variation of i that could not be explained by $\boldsymbol{A}'$. This concept is similar to computing partial correlations. Defining by $\tilde{\boldsymbol{A}}$, $\tilde{\boldsymbol{B}}$ and $\tilde{\boldsymbol{D}}$ the 2×2 analogues to the full problem we obtain

$$\tilde{\boldsymbol{C}} = \tilde{\boldsymbol{A}}^{-1}\boldsymbol{B}\boldsymbol{B}^T\tilde{\boldsymbol{A}}^{-1} + \sigma^2\tilde{\boldsymbol{D}} \tag{17}$$

with $\tilde{\boldsymbol{C}}$ the covariance matrix of the vector $\tilde{\boldsymbol{y}}^{obs} = \left(y_j^{obs}, y_i^{obs} + \sum_{l\neq\{i,j\}} A'_{il}(A'_{ii})^{-1}y_l^{obs}\right)^T$ and $\tilde{D}_{11} = r_j$, $\tilde{D}_{22} = r_i + \sum_{l\neq\{i,j\}} A'^{2}_{il}A'^{-2}_{ii}r_l$, using the scaled variances $r_i = \sigma_i^2/\sigma^2$. Note that $A_{ii} < 0$ for all i as these elements represent sufficiently strong restoring forces that ensure negative definiteness of $\boldsymbol{A}$ and that we have $0 = A'_{ii}y_i^{obs} + \sum_{l\neq i} A'_{il}y_l^{obs}$ from Eq. (1) in the stationary case. An estimate for the minimum relative link strength from node j to node i can be calculated from Eq. (13) and is given by

$$\frac{\tilde{A}_{12}}{\tilde{A}_{11}} = \frac{\tilde{U}_{21}\tilde{D}_{22}^{-1/2}}{\tilde{U}_{11}\tilde{D}_{11}^{-1/2}} \tag{18}$$

Eq. (18) can be considered as an asymptotically unbiased response coefficient between node 1 as target node and node 2 as source node, as again any dependency on σ^2 has dropped out. An estimate for the maximum relative link strength from node j to node i follows from Eq. (18) with the off-diagonal elements of $\boldsymbol{A}'$ set to zero. We classify a link as non-inferable if there exists (i) a significant difference between the minimum und maximum estimated link strength and (ii) a minimum link strength that is not significantly different from noise.

Computational complexity of PRC. The computational cost for computing PRCs scales as $\mathcal{O}\left(N_{sub}^3\right)$, with N_{sub} the size of the subnetwork under consideration. However, as we infer directed networks, we first have to remove the perturbations on each target node before its incoming links can be inferred. The cycling through up to $N_{sub}-1$ perturbed target nodes increases the computational complexity to $\mathcal{O}\left(N_{sub}^4\right)$ in the worst case. As we have generated a subnetwork for perturbed node and used residual bootstrapping to infer statistically significant links, the total computational complexity is given by $\mathcal{O}\left(N_{boot}N_{per}\left\langle N_{sub}^4\right\rangle\right)$, where $\langle . \rangle$ denotes averaging over all subnetworks, N_{per} the number of perturbed nodes, and N_{boot} the number of bootstrap samples. If the travelling distance of perturbations (correlation length) in the network is significantly shorter than the network diameter, such that $N_{sub}/N \to 0$ in the limit of large networks, $N \to \infty$, the computational complexity scales linearly with network size. In contrast, using Lasso to infer directed links requires $\mathcal{O}\left(N_{boot}N_{sig}^4\right)$ operations, as the more efficient Graphical Lasso method[38] is only applicable to undirected networks. Whether our method is computationally

more efficient than Lasso depends on the inference problem. However, for the networks investigated in this work our method required significantly lesscomputational time than inference via Lasso using parallel computing.

Fraction of inferable links. Inferability of a directed link between source and target node requires that the remaining network may not contain the same information that is transmitted between them. A sufficient condition is that all information that the remaining network receives from the source node is destroyed by sufficiently strong perturbations. If the target node is not perturbed, information from the source node may reach the remaining network through the target node. In this case also the targets of the target node must be perturbed (Fig. 2a). Counting network motifs that satisfy these conditions gives the number of inferable links. If the network size, N, is significantly larger than the number of outgoing links for both the source and target nodes, we can approximate the fraction of inferable links, $F(q)$, by the expression (Supplementary Note 1)

$$F(q) \approx \sum_{k=1} \sum_{l=0} \sum_{m=0}^{\min(k-1,l)} \left[q^{k+1} + (1-q)q^{z}\right] P(k,l,m|k \to l)$$

Here, $P(k, l, m|k \to l)$ is the conditional probability of finding two connected nodes in the directed network, where the source node has $k \geq 1$ outgoing links, the target node has $l \geq 0$ outgoing links, and both share m nodes as common targets of their outgoing links. The first term in the brackets corresponds to the case that independent perturbation data for node B exists (Fig. 2a, left panel) and the second term to the case where independent perturbation data for node B are absent (Fig. 2a, right panel). In the calculation of $F(q)$ we assumed that the links in the network are represented by noiseless, linear functions with non-zero slope and that ensure that information of source nodes is neither destroyed nor absorbed in the process of transmission.

Data preparation. Kemmeren et al.[3] provided a transcriptome data set of a *Saccharomyces cerevisiae* genome-wide knockout library (with mutant strains isogenic to S288c). This data set comprises transcript levels of 6170 genes for 1484 deletion mutants. The data are presented as the logarithm of the fluorescence intensity ratios (M-values) of transcripts relative to their average abundance across a large number of wild-type replicates, resulting in logarithmic fold changes of mutant/wild-type gene expression levels compared with a wild-type reference level. Kemmeren et al. also used a dye swap setup for several experiments to average out the effect of a possible dye bias. Their chip design measures most of the genes twice per biological sample, thus allowing to estimate the technical variance. The preprocessing of the data is described in Kemmeren et al.[3], Supplementary Information.

Residual bootstrapping. We make use of the 748 measured wild-type experimental replicates to determine the natural variation among biological replicates, $\delta_{in} := \log_2(r_{in}) - \langle \log_2(r_{in}) \rangle_n$, with $r_{in} := x_{in}/x_i^{pool}$, x_{in} the expression of gene i in wild-type replicate n, x_i^{pool} the expression level of gene i measured after pooling over wild-type replicates, and $\langle . \rangle_n$ denoting the average over replicates. To generate the bootstrap samples we randomly select 200 different δ_{in} from the replicates for each gene i, and add these values to the log fold changes of the perturbed expression levels, $\langle \log_2(r_{in}^{pert}) \rangle_n$, with $r_{in}^{pert} := x_{in}^{pert}/x_i^{pool}$ and the average is taken over the two replicates for each knockout.

Sparsity constraints by removing noisy nodes. As network inference typically comes with an insufficient amount of independent perturbations and experimental replicates we run into the problem of overfitting the data. In this case, noisy information from many network nodes is collected to explain the response of a given target node. L^1-norm regularised regression (Lasso) systematically removes many links, where each link explains only a small part of the variation of the target node, in favour of few links, where each link contributes significantly. In our approach we remove noisy nodes and thus their potential outgoing links, where the critical noise level is determined by the variability among biological replicates. In the presence of noise, our algorithm removes weakly responding nodes from the network. We thereby assume that the existence of many indirect interactions between source and target node by first distributing the signal of the source node among many weakly responding nodes and then collecting these weak signals to generate a significantly responding target node is much less likely than the existence of a single direct interaction. However, in the noise-free case we run into the same problem as Lasso to determine the right cutoff (regularisation parameter).

Synthetic data. Synthetic data were generated using our own model and GeneNetWeaver[25]—an open access software that has been designed for benchmarking network inference methods. With GeneNetWeaver, networks were generated from a model that closely resembles the structure of the yeast regulatory network[25], and steady state levels of node activities were computed using ordinary differential equations. In our data generating model, we first generated scale-free networks with an exponent of 2.5 and an average degree of 2. Then, we solved a system of ordinary differential equations with non-linear regulatory interactions between nodes to obtain steady state values of node activities, e.g., transcript levels. For both models, logarithmic fold changes of node activities were calculated (transcriptional levels upon perturbation relative to wild levels), and gaussian noise was added.

Code availability. MATLAB and Python codes for the network inference algorithm and the data preprocessing steps are available on request.

Data availability. The data sets analysed during the current study are described in ref.[3] and are available from Gene Expression Omnibus https://www.ncbi.nlm.nih.gov/geo/ under the accession numbers GSE42527, GSE42526, GSE42215, GSE42217, GSE42241 and GSE42240.

Received: 11 November 2016 Accepted: 1 December 2017
Published online: 09 January 2018

References

1. Smanski, M. J. et al. Synthetic biology to access and expand nature's chemical diversity. *Nat. Rev. Microbiol.* **14**, 135–149 (2016).
2. Esvelt, K. M. & Wang, H. H. Genome-scale engineering for systems and synthetic biology. *Mol. Syst. Biol.* **9**, 641–641 (2014).
3. Kemmeren, P. et al. Large-scale genetic perturbations reveal regulatory networks and an abundance of gene-specific repressors. *Cell* **157**, 740–752 (2014).
4. Costanzo, M. et al. The genetic landscape of a cell. *Science* **327**, 425–431 (2010).
5. Wilhelm, M. et al. Mass-spectrometry-based draft of the human proteome. *Nature* **509**, 582–587 (2014).
6. Meinshausen, N. et al. Methods for causal inference from gene perturbation experiments and validation. *Proc. Natl Acad. Sci.* **113**, 7361–7368 (2016).
7. Kholodenko, B. N. et al. Untangling the wires: a strategy to trace functional interactions in signaling and gene networks. *Proc. Natl Acad. Sci.* **99**, 12841–12846 (2002).
8. F, F. & Q, Z. Learning sparse causal gaussian networks with experimental intervention: regularization and coordinate descent. *J. Am. Stat. Assoc.* **108**, 288–300 (2013).
9. Newman, M. E. J. *Networks* (Oxford University Press, 2010).
10. Menche, J. et al. Uncovering disease-disease relationships through the incomplete interactome. *Science* **347**, 1257601–1–1257601–7 (2015).
11. Marbach, D. et al. Wisdom of crowds for robust gene network inference. *Nat. Methods* **9**, 796–804 (2012).
12. Feizi, S., Marbach, D., Médard, M. & Kellis, M. Network deconvolution as a general method to distinguish direct dependencies in networks. *Nat. Biotechnol.* **31**, 726–733 (2013).
13. Barzel, B. & Barabási, A.-L. Network link prediction by global silencing of indirect correlations. *Nat. Biotechnol.* **31**, 720–725 (2013).
14. Weigt, M., White, R. A., Szurmant, H., Hoch, J. A. & Hwa, T. Identification of direct residue contacts in protein-protein interaction by message passing. *Proc. Natl Acad. Sci.* **106**, 67–72 (2009).
15. Bastiaens, P. et al. Silence on the relevant literature and errors in implementation. *Nat. Biotechnol.* **33**, 336–339 (2015).
16. Bansal, M., Belcastro, V., Ambesi-Impiombato, A. & di Bernardo, D. How to infer gene networks from expression profiles. *Mol. Syst. Biol.* **3**, 1–10 (2007).
17. Hill, S. M. et al. Inferring causal molecular networks: empirical assessment through a community-based effort. *Nat. Methods* **13**, 310–318 (2016).
18. Friedman, N., Linial, M., Nachman, I. & Pe'er, D. Using Bayesian networks to analyze expression data. *J. Comp. Biol.* **7**, 601–620 (2000).
19. Granger, C. W. J. Investigating causal relations by econometric models and cross-spectral methods. *Econometrica* **37**, 424 (1969).
20. Schreiber, T. Measuring information transfer. *Phys. Rev. Lett.* **85**, 461–464 (2000).
21. Oates, C. & Mukherjee, S. Network inference and biological dynamics. *Ann. Appl. Stat.* **6**, 1209–1235 (2012).
22. Blomen, V. A. et al. Gene essentiality and synthetic lethality in haploid human cells. *Science* **350**, 1092–1096 (2015).
23. Costanzo, M. et al. A global genetic interaction network maps a wiring diagram of cellular function. *Science* **353**, 1381–1394 (2016).
24. Tipping, M. E. & Bishop, C. M. Probabilistic principal component analysis. *J. R. Stat. Soc.* **61**, 611–622 (1999).
25. Schaffter, T., Marbach, D. & Floreano, D. GeneNetWeaver: in silico benchmark generation and performance profiling of network inference methods. *Bioinformatics* **27**, 2263–2270 (2011).
26. Omranian, N., Eloundou-Mbebi, J. M. O., Mueller-Roeber, B. & Nikoloski, Z. Gene regulatory network inference using fused LASSO on multiple data sets. *Sci. Rep.* **6**, 1–14 (2016).
27. Alipanahi, B. & Frey, B. J. Network cleanup. *Nat. Biotechnol.* **31**, 714–715 (2013).

28. Friedman, J., Hastie, T. & Tibshirani, R. Regularization paths for generalized linear models via coordinate descent. *J. Stat. Softw.* **33**, 1–19 (2010).
29. Al-Momani, M. Shrinkage and Penalty Estimation Strategies in Some Spatial Models. *Electronic Theses and Dissertations,* 1–239 (2013).
30. Marbach, D. et al. Revealing strengths and weaknesses of methods for gene network inference. *Proc. Natl Acad. Sci.* **107**, 6286–6291 (2010).
31. Prill, R. J. et al. Towards a rigorous assessment of systems biology models: the DREAM3 challenges. *PLoS ONE* **5**, e9202 (2010).
32. Ruan, J. A top-performing algorithm for the DREAM3 gene expression prediction challenge. *PLoS ONE* **5**, 1–8 (2010).
33. Stockwell, S. R., Landry, C. R. & Rifkin, S. A. The yeast galactose network as a quantitative model for cellular memory. *Mol. BioSyst.* **11**, 28–37 (2015).
34. Shalem, O. et al. Genome-scale crispr-cas9 knockout screening in human cells. *Science* **343**, 84–87 (2014).
35. Vogelstein, B. et al. Cancer genome landscapes. *Science* **339**, 1546–1558 (2013).
36. Williams, E. G. et al. Systems proteomics of liver mitochondria function. *Science* **352**, aad0189–1–aad0189–14 (2016).
37. Schäfer, J. & Strimmer, K. A shrinkage approach to large-scale covariance matrix estimation and implications for functional genomics. *Stat. Appl. Genet. Mol. Biol.* **4**, 1–32 (2005).
38. Friedman, J., Hastie, T. & Tibshirani, R. Sparse inverse covariance estimation with the graphical lasso. *Biostatistics* **9**, 432–441 (2008).
39. Siegenthaler, C. & Gunawan, R. Assessment of network inference methods: how to cope with an underdetermined problem. *PLoS ONE* **9**, e90481 (2014).

Acknowledgements

We acknowledge help from Patrick Kemmeren in interpreting the yeast transcriptome data, the High Performance Computing Plattform of the Heinrich-Heine University and DFG funding by SPP 1395 and the Cluster of Excellence in Plant Sciences (grant no. EXC 1028).

Author contributions

A.S.K. and M.K. conceived the PRC method. N.H. and M.K. developed the counting procedure for inferable links and the Inferability measure. C.F.B. and M.K. developed the clustering and subnetwork methods and analysed the transcriptome data. N.H. wrote Supplementary Note 1. M.K. wrote Supplementary Note 2. C.F.B. wrote Supplementary Note 3.

Additional information

Supplementary Information accompanies this paper at https://doi.org/10.1038/s41467-017-02489-x.

Competing interests: The authors declare no competing financial interests.

Reprints and permission information is available online at http://npg.nature.com/reprintsandpermissions/

Publisher's note: Springer Nature remains neutral with regard to jurisdictional claims in published maps and institutional affiliations.

Supplementary Note 1

Counting the number of inferable links as a function of perturbed nodes

The expected fraction of inferable links can be calculated analytically if (i) the N_p externally perturbed nodes are uniformly distributed throughout the network, (ii) measurement noise is absent, (iii) additional perturbations – such as internal perturbations arising from thermal noise – are absent, (iv) links are assumed to be represented by noiseless, linear functions with non-zero slope, and (v) an arbitrary large set of perturbation experiments can be generated, with the freedom to tune the perturbation strength for each node independently. Throughout this work we do not assume that networks belong to the class of directed acyclic graphs (DAG), which is often a necessary prerequisite for approaches based on Bayesian networks [1] and structural equations models [2]. The assumption that perturbed nodes are uniformly distributed throughout the network is done for mathematical convenience and can be generalised to other distributions. However, if the distribution of perturbed nodes correlates with features that affect inferability, such as the outdegree, the maximum fraction of inferable links can change significantly. We assume links to be represented by linear functions as otherwise inferability would depend on the functional realisation of each link due to fact that any saturating behaviour by sigmoidal functions can limit the information that can be transmitted, which in turn can affect the fraction of inferable links. Moreover, a linear network model has the important property that independent single-node perturbation experiments can be linearly combined to compute the expected responses of multi-node perturbation experiments.

To count the number of inferable links under the conditions (i)-(v) we assume that for a given subnetwork a perturbed node (A) targets a node (B), given that the outdegree of node A is k, the outdegree of node B is l, and A and B have c nodes as common targets (Supplementary Figure 1). We denote a directed link from source node (A) to target node (B) as inferable if there exits a detectable amount of mutual information between A and B that cannot be transmitted by any alternative route through the network. This requires that at least one node of each alternative route is perturbed and thereby part of the transmitted information is destroyed. It is important to recognise that it is necessary and sufficient to perturb only the shortest alternative routes that pass through the outgoing nodes of A or B, as we assume that all possible network structures – and thus also the shortest ones – occur with the same prior probability and information about A spreading through the network must pass through the outgoing nodes of A or B. To meet

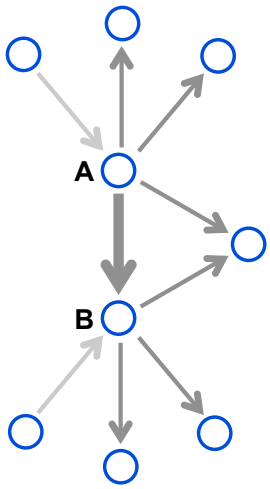

Supplementary Figure 1: Example of a directed subnetwork. We would like to infer the link from node A to node B (shown in bold), where A has outdegree 4, B has outdegree 3, and A and B share 1 common target.

this requirement, either one of the following conditions must be fulfilled (Fig. 2a, main text):

1. All nodes that are targeted by A are perturbed, including node B.
2. Except B, all nodes that are targeted by A and B are perturbed.

By collecting all subnetworks that fulfil conditions 1 or 2 we can calculate the average fraction of inferable links, $F(N_p)$, using $N' := N-k-1$ and $N'_p := N_p-k-1$

$$F(N_p) = \sum_k \frac{\binom{N'}{N'_p}}{\binom{N}{N_p}} P(k|A \to B) + \sum_{k,l,c} \frac{\binom{N'-l+c}{N'_p-l+c+1}}{\binom{N}{N_p}} P(k,l,c|A \to B) \quad (1)$$

Here, N is network size, N_p is number of perturbed nodes, k is the outdegree of the source node (A), l is the outdegree of the target node (B), c is the number of common nodes targeted by A and B. We further defined by $P(k|A \to B)$ the conditional probability that for any two connected nodes, source node (A) has

outdegree k and $P(k,l,c|A \to B)$ is conditional probability that for any two connected nodes, source node (A) has outdegree k , target node (B) has outdegree l, and A and B target c common nodes. The first term in the numerator counts motifs that fulfil condition 1, and the second term in the numerator counts motifs that fulfil condition 2. The term in the denominator counts all possible network motifs, when N_p nodes of the network are perturbed.

Assuming that the network size, N, and the number of perturbed nodes, N_p, are much larger than the outdegrees, $N, N_p \gg k, l$, we can apply Stirling's approximation and simplify Eq. (1)

$$F(q) \approx \sum_{k,l,c} \left[q^{k+1} + (1-q)q^{k+l-c}\right] P(k,l,c|A \to B) \tag{2}$$

where q denotes fraction of perturbed nodes, $q = N_p/N$.

Network's Inferability

According to Eq. (2), networks with different structural features have different $F(q)$ curves (Fig. 1b, main text). We therefore define an inferability measure, I_F, as the area under the curve of F(q) that reflects how difficult it is to infer links for a given network structure

$$\begin{aligned} I_F &= \int_0^1 F(q)dq \\ &= \sum_{k,l,c} \left[\frac{1}{k+2} + \frac{1}{k+l-c+1} - \frac{1}{k+l-c+2}\right] P(k,l,c|A \to B) \end{aligned} \tag{3}$$

Note that I_F is independent of network size. For sufficiently large networks $N \gg 1$ and when feed forward loops are rare, we can approximate the joint probability by

$$\begin{aligned} I_F &\approx I_F^* \\ &:= \sum_{k,l,c} \left[\frac{1}{k+2} + \frac{1}{k+l+1} - \frac{1}{k+l+2}\right] P(k|A \to B)P(l|A \to B) \end{aligned} \tag{4}$$

According to Eqs. (3) and (4), inferability mainly depends on the outdegree of nodes. Consequently, networks consisting of nodes with high outdegree have low inferability (I_F) and are the most difficult ones to infer.

Comparison of $F(N_p)$ with the inference algorithm

We compared the fraction of inferable links determined by the analytical formula, $F(N_p)$, and the average number of inferable links classified by our inference algorithm in the limit of low measurement noise. In order to calculate the average number of inferable links from the inference algorithm, we focus on scale-free and random networks. For each number of perturbed nodes, N_p, we first randomly select the nodes that will be perturbed and subsequently generate node activity data for single-node perturbations. For each random sample of N_p nodes, we calculate the fraction of inferable links and finally average over all configurations of perturbed nodes. We compared the results of the analytical and numerical approaches for three different types of networks (Supplementary Figure 2). We considered a scale-free network where hubs are targets of links (Supplementary Figure 2-a), a scale-free network where hubs are sources of links (Supplementary Figure 2-b), and a random network (Supplementary Figure 2-c). For all three network types, the network sizes are $N = 100$ and averaging runs over 300 different configurations of N_p randomly selected nodes that are perturbed individually by knockouts.

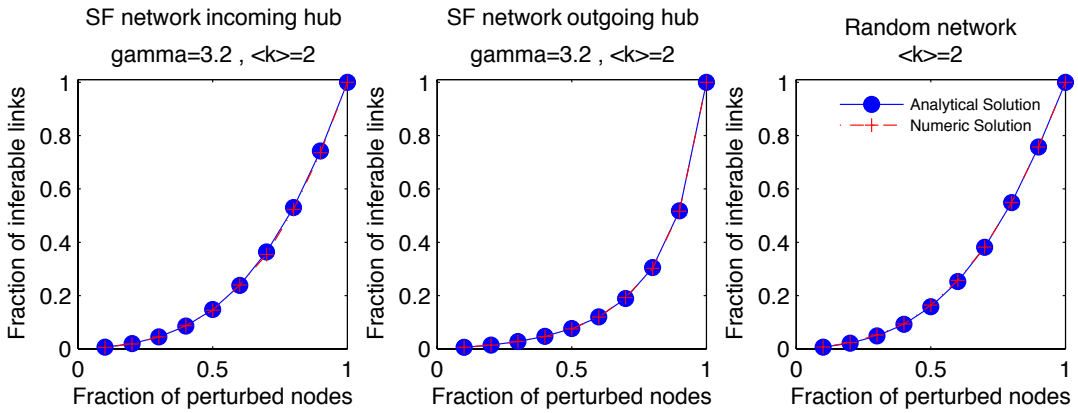

Supplementary Figure 2: Comparison of the analytical formula, Eq. (1) and the inference algorithm by calculating the number of inferable links with respect to the number of perturbed nodes, N_p.

3 Pharmocokinetics Modeling of Cangrelor

3.1 Summary

Cangrelor is a high-affinity, reversible antagonist of the $P2Y_{12}$ receptor that inhibits ADP-induced platelet aggregate completely. Cangrelor has a short half-life of 2.6 to 3.3 minutes and reaches steady-state rapidly [45]. Cangrelor is approved for patients with Coronary artery disease (CAD) undergoing percutaneous coronary intervention (PCI). Due to the short half-life of Cangrelor, it should be administered as a bolus of 30 μg/kg followed by an immediate infusion of 4 μg/kg/min for at least 2 hours [46]. However, in clinical routine, several deviations from the correct administration of the drug, such as delay in the start of the infusion after bolus administration or interruptions during infusion, may occur.

By applying a one-compartment model, the kinetics of Cangrelor is studied. Based on the model, the impact of different deviations of correct administration of the drug is investigated; such as different delay times, and different durations of interruption. For this purpose, for each duration of delay and interruption, the change of plasma concentration of the drug is considered. Furthermore, an optimum second bolus dosage is suggested to reconstruct to steady-state condition, in such a way that the drug concentration achieves an effective but not excessive Cangrelor serum concentration.

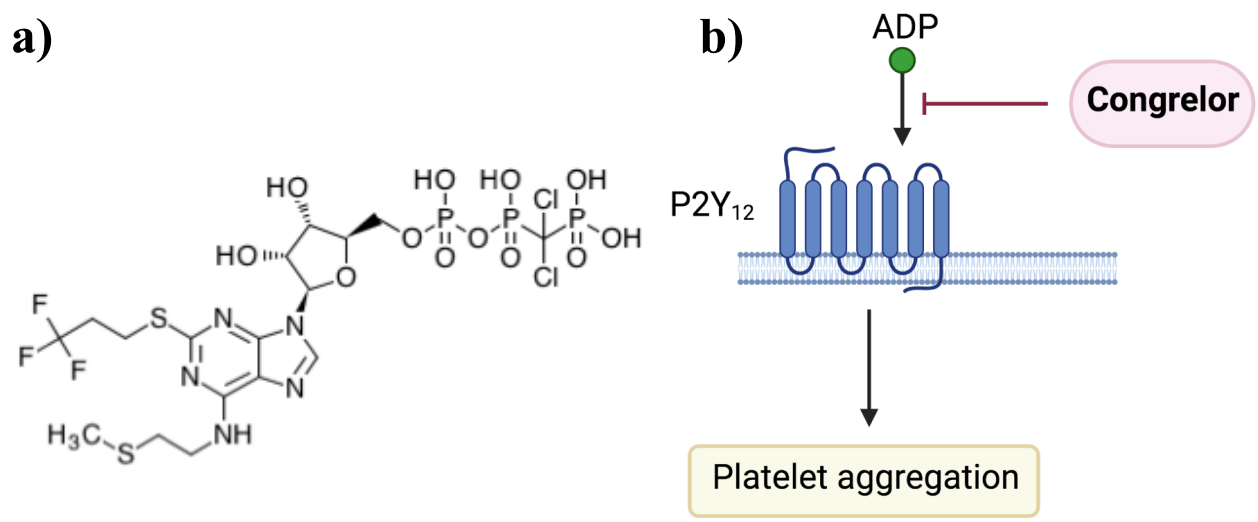

Fig. 3.1 a) Chemical structure of Cangrelor. b) Inhibition of ADP-induced platelet aggregate by Congrelor.

3.2 Publication: Pharmacosimulation of interruptions and its solution in intravenous administration of cangrelor

Authors: Maryna Masyuk, Nadia Heramvand, Johanna M. Muessig, Amir M. Nia, Amin Polzin, Markus Kollmann, Malte Kelm, Christian Jung
This article is published in Clinical Hemorheology and Microcirculation, vol. 68, no. 4, pp. 421-425, 2018

Contribution of Nadia Heramvand:

- developed predictive pharmacokinetics (PK) of Congrelor
- simulated clinical complications, i.e, delay, and interruption of the drug infusion

Clinical Hemorheology and Microcirculation xx (20xx) x–xx
DOI 10.3233/CH-170323
IOS Press

Pharmacosimulation of interruptions and its solution in intravenous administration of cangrelor

Maryna Masyuk[a,*], Nadia Heramvand[b,c], Johanna M. Muessig[a], Amir M. Nia[a], Amin Polzin[a], Markus Kollmann[b], Malte Kelm[a] and Christian Jung[a]
[a]*Department of Internal Medicine, Division of Cardiology, Pulmonary Diseases, Vascular Medicine, University Hospital Düsseldorf, Düsseldorf, Germany*
[b]*Institute of Mathematical Modelling of Biological Systems, Department of Biology, Faculty of Mathematics and Natural Sciences, Heinrich-Heine-University Düsseldorf, Düsseldorf, Germany*
[c]*Max Planck Institute for Plant Breeding Research, Köln, Germany*

Abstract.
BACKGROUND: Cangrelor is an intravenous adenosine diphosphate (ADP) $P2Y_{12}$ receptor antagonist, which has to be administered as a bolus followed by immediate infusion. Nevertheless, in clinical routine deviations from the correct practice, such as delayed infusion onset or interruptions during infusion, may occur.
OBJECTIVE: The objective of the present study was to investigate the impact of administration delays on cangrelor concentration in a pharmacological simulation setting and to give possible solutions for the clinical practice.
METHODS: We simulated the effects of different delays in administration of cangrelor in a model based on known pharmacokinetic parameters. Additionally, we calculated the optimal dosage of a second bolus.
RESULTS: We demonstrate that already a short delay between the bolus and begin of infusion as well as short infusion interruptions considerably affect the serum concentration of cangrelor. Additionally, we estimate the dosage of a possible second bolus which highly depends on the duration of the delay.
CONCLUSIONS: Our results emphasize that continuous administration of cangrelor is crucial to avoid the critical time frame of increased thrombosis risk. We suggest a strategy for dealing with interruptions by demonstrating that a second bolus allows to reach rapidly an effective but not excessive cangrelor serum concentration.

Keywords: Cangrelor, $P2Y_{12}$ inhibitor, pharmacokinetics, pharmacosimulation

1. Introduction

Percutaneous coronary intervention (PCI) with stent implantation is the treatment of choice in patients with acute coronary syndrome [1]. It has been established that the use of adjunctive antiplatelet therapy during and after PCI is crucial in preventing thrombotic complications [2]. In the last two decades, unfractionated heparin, aspirin and $P2Y_{12}$ inhibitors evolved the standard antithrombotic therapy in patients undergoing PCI [3]. Although the oral $P2Y_{12}$ antagonists, such as clopidogrel, ticagrelor and prasugrel, are potent agents in reducing ischemic events, in particular stent thrombosis, several limitations of these drugs are known. Thus, the irreversibility of the action of clopidogrel and

*Corresponding author: Maryna Masyuk, M.D., Division of Cardiology, Pulmonary Diseases, Vascular Medicine, University Hospital Düsseldorf, Moorenstraße 5, 40225 Düsseldorf, Germany. Tel.: +49 211 8115897; Fax: +49 211 8115493; E-mail: maryna.masyuk@med.uni-duesseldorf.de.

prasugrel is associated with increased bleeding risk if urgent surgery is required [4]. Another problem is the bioavailability in acute settings, in which the patients might be sedated or present nausea, vomiting or a shock state [5, 6]. Recently, novel antiplatelet drugs have been developed. Among these, cangrelor is the only potent intravenous direct and specific adenosine diphosphate (ADP) $P2Y_{12}$ receptor antagonist. It is characterized by a fast onset of action as well as fast reversibility, making it a reliable antiplatelet therapeutic in acute clinical setting [7]. To prevent thrombotic complications, it is essential to rapidly achieve the therapeutic serum concentration and to maintain it continuously. Due to its short half-life (approximately 3 to 6 minutes), cangrelor has to be administered as a bolus (30 μg/kg) followed by immediate infusion (4 μg/kg/min) [8, 9]. However, in clinical routine several deviations from the correct practice, such as belated onset of the infusion after bolus administration or interruptions during infusion, may occur.

Thus, the purpose of the present study was to demonstrate the impact of different alterations from the correct administration mode on cangrelor serum concentration in order to estimate the kinetics of underdosage and to give suggestions for delay management in clinical practice. Therefore, we simulated multiple bolus-infusion delays and infusion interruptions using mathematical modeling based on known pharmacokinetic parameters of cangrelor.

2. Methods

Simulations were performed using ode45 ordinary differential equation solver for MATLAB Software (R2015a, MathWorks, Natick, MA, USA). The starting point for all the simulations was the recommended application mode consisting of an administration of a 30 μg/kg bolus followed by continuous infusion at a concentration rate of 4 μg/kg/min. All simulations were performed based on pharmacokinetic parameters published in literature [8, 10]. Briefly, cangrelor activity was assumed to follow a one-compartment model, as after intravenous application it is rapidly distributed in the blood plasma showing a plasma protein binding rate of 97 to 98% and metabolized in the circulation independently of hepatic or renal function [10]. It has been shown to have linear pharmacokinetics in the range of the tested concentrations, in both healthy volunteers and patients. After intravenous administration of the bolus, cangrelor reaches its maximum plasma concentration within 2 minutes achieving the steady-state concentration of 488 ng/ml after approximately 10 minutes. Finally, cangrelor is metabolized by dephosphorylation to its primary metabolite, a nucleoside with a negligible anti-platelet activity. Cangrelor metabolites are excreted to approximately two third via urine and one third via feces. Further pharmacokinetic parameters used for the simulations were volume of distribution of 0.05 l/kg and elimination half-life of 3.5 minutes [10, 11]. On this basis, mathematical simulations were performed to evaluate effects of different delays between the bolus and initiation of the infusion as well as interruptions of continuous infusion of length. Subsequently, the dosage of a second bolus was calculated in a manner, allowing to rapidly reachieve an effective but not excessive cangrelor serum concentration. Each simulation was performed ten times to prevent possible errors.

3. Results

Using the known pharmacokinetic parameters of cangrelor, we mathematically simulated the effects of different delays and interruptions in application on the drug serum concentration. Here we demonstrated that already a short delay between the bolus and the beginning of infusion of only 4 minutes considerably affects the serum concentration of cangrelor. Longer delays of 10 or 15 minutes even lead to drastic decreases to 26% or 10% of the target drug concentration (Fig. 1A-C). Furthermore, we showed that already interruptions of continuous infusion of only 1 minute decreased the cangrelor

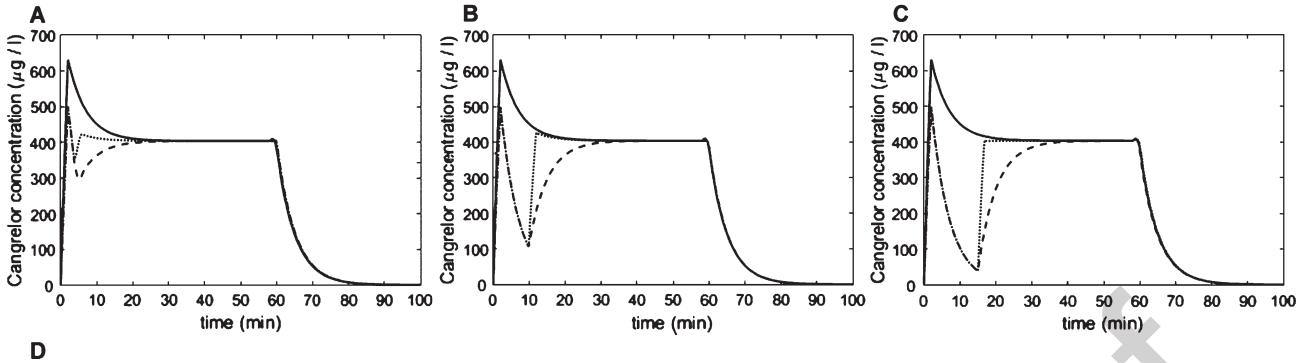

D

Time Delay min	1	2	3	4	5	6	7	8	9	10	11	12	13	14	15
Dosage of 2nd Bolus µg/kg				4.0	4.2	7.1	10.0	10.5	11.1	13.0	13.5	13.7	15.0	15.0	16.9
Dosage of 2nd Bolus mg (adjusted to 80 kg)				0.32	0.34	0.57	0.80	0.84	0.89	1.04	1.08	1.10	1.20	1.20	1.35

Fig. 1. Effects of bolus-to-infusion delays on serum cangrelor concentration. Delays: A: 4 minutes, B. 10 minutes, C. 15 minutes. The solid line in each plot shows the regular pharmacokinetics of cangrelor administered in accordance with recommendations. The dashed lines show the rapid decrease in cangrelor serum levels beneath the target concentration after the delays between the bolus and initiation of infusion. The dotted lines show the effectiveness of the second bolus to rapidly reachieve the steady-state concentration of cangrelor.

serum concentration rapidly beneath the steady-state level. Longer interruptions of 5 or 10 minutes lead to substantial decreases in drug concentration (Fig. 2A-C). Additionally, we estimated the dosage of a possible second bolus, which highly depends on the duration of the delay. Figure 1D shows the calculated optimal dosages of the second bolus according to the duration of delay. Thus, after 4 minutes of delay between the first bolus and the infusion initiation a dosage of 4 µg/kg is sufficient to quickly reachieve the steady-state concentration of cangrelor, whereas longer delays require higher drug concentrations, e.g. 13 µg/kg after a delay of 10 minutes. For interruptions of the continuous infusion an analogous temporal dependence of the second bolus dosage can be observed (Fig. 2D).

4. Discussion

Several studies have shown cangrelor to be a potent and safe antiplatelet agent, which can be effectively used in acute settings due to its intravenous application mode, its fast action onset while being no prodrug, and total reversibility. The use of cangrelor in patients undergoing PCI has been studied in two clinical studies, the Cangrelor versus Standard Therapy to Achieve Optimal Management of Platelet Inhibition (CHAMPION) PCI and CHAMPION PLATFORM studies. Here, it has been reported that cangrelor application during PCI was associated with reductions of prespecified secondary end points, such as stent thrombosis and death of any cause as compared to placebo during PCI group. At the same time there was no significant difference in bleeding events requiring blood transfusion between the cangrelor and standard therapy groups [12, 13]. The CHAMPION PHOENIX trial designed to evaluate whether cangrelor reduces ischemic events after PCI revealed a significant reduction in ischemic events including stent thrombosis and myocardial reinfarction within 48 hours post-PCI in patients receiving cangrelor as compared to the group receiving a loading dose clopidogrel [14]. Its pharmacokinetic properties, such as short half-life, not only make cangrelor an optimal antiplatelet drug during emergency situations, but also imply the necessity of strict administration standards.

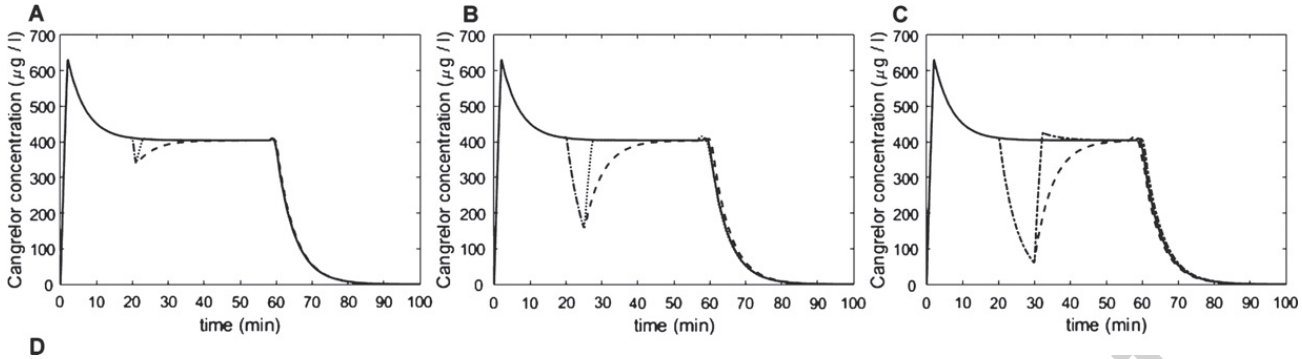

D

Time Interruption min	1	2	3	4	5	6	7	8	9	10
Dosage of 2nd Bolus µg/kg	3.0	5.5	5.5	8.5	8.5	10.5	11.0	11.0	13.0	13.4
Dosage of 2nd Bolus mg (adjusted to 80 kg)	0.24	0.44	0.44	0.68	0.68	0.84	0.88	0.88	1.04	1.07

Fig. 2. Effects of infusion interruptions on serum cangrelor concentration. Duration of interruptions: A: 1 minute, B. 5 minutes, C. 10 minutes. The solid line in each plot shows the regular pharmacokinetics of cangrelor administered as a continuous infusion. The dashed lines show the rapid decrease in cangrelor serum levels beneath the target concentration after infusion interruptions. The dotted lines show the effectiveness of the second bolus to rapidly reachieve the steady-state concentration of cangrelor.

In a substudy of the CHAMPION trial concerning the pharmacodynamic effects of cangrelor on the platelet function, Angiolillo and colleagues observed that the average platelet reactivity after discontinuation of cangrelor infusion was not significantly different between the patients treated initially with cangrelor or loading dosis clopidogrel. This supports the assumption of a rapid platelet recovery upon termination of administration of cangrelor [9]. These results strengthen our hypothesis that maintenance of a constant serum concentration of cangrelor is crucial for a sufficient antithrombotic effect. In the present study, we demonstrate that already short delays or interruptions in cangrelor administration lead to a rapid and substantial decrease of drug serum concentrations.

Our results highly suggest avoiding bolus-infusion delays or infusion interruptions. If the deviation from the proper administration mode has already occurred, an appropriate approach from the pharmacokinetic prospective would be the application of a second bolus. Here, we estimated the dosage of the second bolus according to the duration of the delay or interruption required to achieve effective concentration of cangrelor without causing overdosage. However, it must be taken into account that the present study is based on a simulated model. In this setting, it can be only assumed that the decrease of concentration affects the antiplatelet effect of cangrelor. It cannot be proven that the simulated delays and interruptions have a relevant effect on the platelet aggregation. This represents the major limitation of our study. Nevertheless, pharmacosimulation studies serve as a valuable tool to provide an initial assessment of concentration alterations after incorrect use of a drug.

5. Conclusion

Here, we give first insights in management of interruptions of cangrelor administration after PCI in clinical practice. While evidently further clinical safety and efficacy trials are necessary for final

recommendations in the future, we strongly recommend avoiding bolus-infusion delays and to administer the bolus only when the infusion is prepared.

References

[1] Bavry AA, Kumbhani DJ, Rassi AN, Bhatt DL, Askari AT. Benefit of early invasive therapy in acute coronary syndromes: A meta-analysis of contemporary randomized clinical trials. J Am Coll Cardiol. 2006;48(7):1319-25.

[2] Ullrich H, Gori T. Antiplatelet therapies in patients with an indication for anticoagulation. Clin Hemorheol Microcirc. 2016;64(3):273-8.

[3] Koskinas KC, Räber L, Zanchin T, Pilgrim T, Stortecky S, Hunziker L, et al. Duration of triple antithrombotic therapy and outcomes among patients undergoing percutaneous coronary intervention. JACC Cardiovasc Interv. 2016;9(14): 1473-83.

[4] Kapetanakis EI, Medlam DA, Boyce SW, Haile E, Hill PC, Dullum, Mercedes KC, et al. Clopidogrel administration prior to coronary artery bypass grafting surgery: The cardiologist's panacea or the surgeon's headache? Eur Heart J. 2005;26(6):576-83.

[5] Heestermans, Antonius ACM, van Werkum, Jochem W, Taubert D, Seesing TH, Beckerath N von, Hackeng CM, et al. Impaired bioavailability of clopidogrel in patients with a ST-segment elevation myocardial infarction. Thromb Res. 2008;122(6):776-81.

[6] Součková L, Opatřilová R, Suk P, Čundrle I, Pavlík M, Zvoníček V, et al. Impaired bioavailability and antiplatelet effect of high-dose clopidogrel in patients after cardiopulmonary resuscitation (CPR). Eur J Clin Pharmacol. 2013;69(3):309-17.

[7] Greenbaum AB, Grines CL, Bittl JA, Becker RC, Kereiakes DJ, Gilchrist IC, et al. Initial experience with an intravenous P2Y12 platelet receptor antagonist in patients undergoing percutaneous coronary intervention: Results from a 2-part, phase II, multicenter, randomized, placebo- and active-controlled trial. Am Heart J. 2006;151(3):689.e1-689.e10.

[8] Akers WS, Oh JJ, Oestreich JH, Ferraris S, Wethington M, Steinhubl SR. Pharmacokinetics and pharmacodynamics of a bolus and infusion of cangrelor: A direct, parenteral P2Y12 receptor antagonist. J Clin Pharmacol. 2010;50(1):27-35.

[9] Angiolillo DJ, Schneider DJ, Bhatt DL, French WJ, Price MJ, Saucedo JF, et al. Pharmacodynamic effects of cangrelor and clopidogrel: The platelet function substudy from the cangrelor versus standard therapy to achieve optimal management of platelet inhibition (CHAMPION) trials. J Thromb Thrombolysis. 2012;34(1):44-55.

[10] U.S. Food and Drug Administration [homepage on the Internet]. Silver Spring: KENGREAL™ (cangrelor) for injection, for intravenous use. Highlights of prescribing information; 2015 [updated 2015 Jun; cited 2017 Aug 13]. Available from: https://www.accessdata.fda.gov/drugsatfda_docs/label/2015/204958lbl.pdf

[11] U.S. Food and Drug Administration [homepage on the Internet]. Silver Spring: FDA Briefing Document for the Cardiovascular and Renal Drugs Advisory Committee (CRDAC); 2015 [updated 2015 Apr 15; cited 2017 Aug 13]. Available from: https://www.fda.gov/downloads/AdvisoryCommittees/CommitteesMeetingMaterials/Drugs/CardiovascularandRenalDrugsAdvisoryCommittee/UCM442199.pdf

[12] Bhatt DL, Lincoff AM, Gibson CM, Stone GW, McNulty S, Montalescot G, et al. Intravenous platelet blockade with cangrelor during PCI. N Engl J Med. 2009;361(24):2330-41.

[13] Harrington RA, Stone GW, McNulty S, White HD, Lincoff AM, Gibson CM, et al. Platelet inhibition with cangrelor in patients undergoing PCI. N Engl J Med. 2009;361(24):2318-29.

[14] Bhatt DL, Stone GW, Mahaffey KW, Gibson CM, Steg PG, Hamm CW, et al. Effect of platelet inhibition with cangrelor during PCI on ischemic events. N Engl J Med. 2013;368(14):1303-13.

4 Pharmocokinetics Modeling of Tirofiban

4.1 Summary

Tirofiban is a non-peptide reversible antagonist of the platelet-fibrinogen glycoprotein (GP) IIb/IIIa receptor and inhibits platelet aggregation (Fig 4.1). It prevents the blood from clotting during episodes of chest pain or a heart attack, or while the patient is undergoing a procedure to treat a blocked coronary artery [47].

There are differences in recommended dosage in EU and USA labels, which require different adjustment dosages for patients with normal renal function and severe renal impairment (Table 4.1 [48] , [49]).

This study aims to apply pharmacokinetic modeling to investigate the difference between American and European Tirofiban recommended dosage for three groups of patients:

- Group 1: Healthy volunteers (CrCl >90 mL/min),
- Group 2: Subjects with moderate (CrCl 30-59 mL/min) renal impairment
- Group 3: Subjects with severe (CrCl <30 mL/min) renal impairment

By applying a two-compartment model and using patient data, first of all, PK parameters of Tirofiban for each goup of patients is calculated. Second the dynamical behavior of the drug under EU and USA recommended dosages is studied. Then the effect of infusion delay and

infusion interruption is investigated. Moreover, an effective second bolus dosage is calculated to reconstitute plasma concentration as quickly, but not excessively, as possible.

Table 4.1 EU and US recommended dosage of Tirofiban

	EU	US
Dosing	0.4 μg/kg/min for 30 minutes, followed by 0.1 μg/kg/min infusion	25 μ g/kg within 5 minutes, followed by 0.15 μ/kg/min infusion for up to 18 hours
Renal Dose adjustment	For patients with creatinine clearance < 30mL/min: both the loading and maintenance infusion are reduced by 50%	For patients with creatinine clearance < 60 mL/min: bolus is unchanged at 25 μg/kg/min, maintenance infusion is reduceed by 50% to 0.075 μg/kg/min

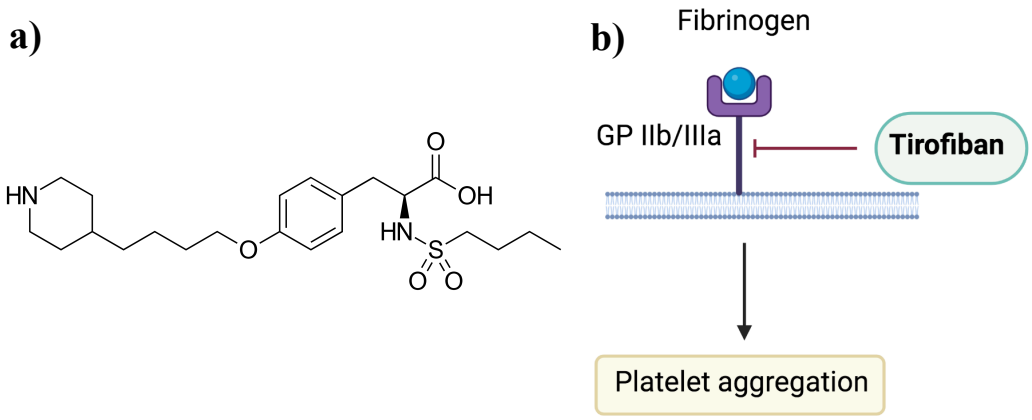

Fig. 4.1 a) Chemical structure of Tirofiban. b) Tirofiban blocks platelet accumulation by inhibiting the binding of fibrinogen to GP IIb/IIIa receptors

4.2 Publication: Pharmacosimulation of delays and interruptions during administration of tirofiban: a systematic comparison between EU and US dosage regimens

Authors: Nadia Heramvand, Maryna Masyuk, Johanna M. Muessig, Amir M. Nia, Athanasios Karathanos1, Amin Polzin, Marco Valgimigli, Paul A. Gurbel, Udaya S. Tantry, Malte Kelm, Christian Jung
This article is published in Journal of Thrombosis and Thrombolysis, 2022.

Contribution of Nadia Heramvand:

- estimated PK parameters of Tirofiban
- developed predictive pharmacokinetics (PK) of Tirofiban
- compared The US and EU recommendation dosages
- simulated clinical complications, i.e, delay, and interruption of the drug infusion
- generated the figures
- wrote the method section

Journal of Thrombosis and Thrombolysis
https://doi.org/10.1007/s11239-022-02654-0

Pharmacosimulation of delays and interruptions during administration of tirofiban: a systematic comparison between EU and US dosage regimens

Nadia Heramvand[1] · Maryna Masyuk[1] · Johanna M. Muessig[1] · Amir M. Nia[1] · Athanasios Karathanos[1] · Amin Polzin[1] · Marco Valgimigli[3] · Paul A. Gurbel[4] · Udaya S. Tantry[4] · Malte Kelm[1,2] · Christian Jung[1]

Accepted: 5 April 2022

Abstract

Tirofiban is a glycoproteine (GP) IIb/IIIa receptor antagonist, which inhibits platelet-platelet aggregation and is a potential adjunctive antithrombotic treatment in patients with acute coronary syndromes (ACS) or high-risk percutaneous coronary interventions (PCI). It is administered intravenously as a bolus followed by continuous infusion. However, the dosage recommendations in the United States (US) and European Union (EU) differ considerably. Furthermore, in routine clinical practice, deviations from the recommendations may occur. The objective of the present study was to investigate the impact of different alterations on tirofiban plasma concentrations in US and EU administration regimens and to give suggestions for delay management in clinical practice. We therefore mathematically simulated the effects of different bolus-infusion delays and infusion interruptions in different scenarios according to the renal function. Here, we provide a systematic assessment of concentration patterns of tirofiban in the US versus EU dosage regimens. We show that differences between the two regimens have important effects on plasma drug levels. Furthermore, we demonstrate that deviations from the proper administration mode affect the concentration of tirofiban. Additionally, we calculated the optimal dosage of a second bolus to rapidly restore the initial concentration without causing overdosage. In conclusion, differences in tirofiban dosing regimens between the U.S and EU and potential infusion interruptions have important effects on drug levels that may impact on degrees of platelet inhibition and thus antithrombotic effects. Thus, the findings of our modelling studies may help to explain differences in clinical outcomes observed in previous clinical trials on tirofiban.

Keywords Tirofiban · GP IIb/IIIa inhibitor · Pharmacokinetics · Pharmacosimulation

Highlights

- Tirofiban is a potential adjunctive antithrombotic treatment in patients with ACS or high-risk PCI.
- Maintenance of a proper plasma concentration is crucial for sufficient antithrombotic effect and a better clinical outcome.
- The dosage recommendations for normal or impaired renal function differ significantly between U.S. and EU, which has important effects on plasma drug levels.
- Here, we provide first suggestions for management of delays or interruptions in daily clinical practice, which should be investigated in future studies.

Nadia Heramvand, Maryna Masyuk both contributed equally to this work.

✉ Maryna Masyuk
maryna.masyuk@med.uni-duesseldorf.de

[1] Department of Medicine, Division of Cardiology, Pulmonary Diseases and Vascular Medicine, University Hospital Düsseldorf, Moorenstraße 5, 40225 Düsseldorf, Germany

[2] CARID: Cardiovascular Research Institute Düsseldorf, Düsseldorf, Germany

[3] Cardiocentro Ticino, Lugano and University of Bern, Bern, Switzerland

[4] Sinai Center for Thrombosis Research and Drug Development, Sinai Hospital of Baltimore, Baltimore, MD, USA

Published online: 28 April 2022

Introduction

Platelet-fibrinogen interaction is a crucial pathway in platelet aggregation and the pathogenesis of coronary artery thrombosis [1]. By binding to glycoprotein (GP) IIb/IIIa receptors, fibrinogen ensures platelet-platelet aggregation and thrombus formation at the site of vascular injury [2]. Thus, blockade of GP IIb/IIIa receptor is a potential additional antithrombotic treatment strategy [3, 4]. Tirofiban is an intravenous non-peptide reversible GP IIb/IIIa receptor antagonist [5, 6]. Several large randomized controlled trials (RCTs) have shown the antithrombotic benefits of tirofiban use in patients with acute coronary syndromes (ACS) and in high-risk percutaneous coronary interventions (PCI) [6–9]. A PCI is considered as a high-risk procedure when several characteristics, including complex coronary artery disease (multivessel or left main disease and anatomically complex coronary lesions), hemodynamic compromise (shock or severely depressed LV function), and clinical comorbidities such as advanced age, diabetes mellitus, peripheral vascular disease, heart failure, acute coronary syndromes, or previous cardiac surgery, apply [10]. A meta-analysis including 6 large RCTs with 29,570 non ST-elevation ACS patients has confirmed a significant reduction of 30-day mortality or non-fatal myocardial infarction (MI) in patients receiving GP IIb/IIIa inhibitors [11]. However, bleeding events remain a major concern [6]. Thus, current European Society of Cardiology (ESC) and American Heart Association/American College of Cardiology (AHA/ACC) guidelines recommend the use of GP IIb/IIIa inhibitors in ACS patients treated invasively with dual antiplatelet therapy (DAPT) with a Class IIb for bailout situations or thrombotic complications during PCI [12, 13]. Tirofiban is administered intravenously as a bolus followed immediately by continuous infusion. The current dosage regimens are regulated and approved by the United States (US) Food and Drug Administration (FDA) and European Medicines Agency (EMA). However, the dosage recommendations of the two regulatory bodies differ considerably [14, 15].

In routine clinical practice, several deviations from the recommendations, such as delay between the bolus and the infusion or infusion interruptions may occur. The purpose of the present study was to investigate, by mathematical modelling, the impact of various deviations from the recommended tirofiban administration regimen on plasma concentrations for both US and EU tirofiban on-label regimens and provide practical suggestions for their optimal pharmacological management.

Methods

Simulations were performed using the Python™ programming language. First, a two-compartment pharmacokinetic (PK) model of tirofiban has been applied, as after a single intravenous bolus, the plasma concentration–time of tirofiban passes through distribution and disposition phases (Supplementary Fig. 1 a). Therefore, the plasma concentration–time of tirofiban could be described through $Cp(t) = Ae - \alpha t + Be^{-\beta t}$ equation, where $Cp(t)$ is the plasma concentration at any time (t), A and B are empirical constants, α and β are distribution and disposition rate constants, respectively. This biphasic behaviour of plasma concentration could be also explained as tirofiban is not strongly bound to plasma protein with an unbound fraction in human plasma of 35%[14]. In the next step, A, B, α and β were estimated by applying the method of residuals [16] and based on real-world concentration measurements at different time points in patients with normal or impaired renal function, obtained during product development (Supplementary Table 1). Briefly, patients were treated with a 25 µg/kg tirofiban bolus. The patients were subdivided into three groups according to the renal function: patients with normal function (creatinine clearance; CrCl > 90 ml/min; $n = 8$), moderate (CrCl 30–59 ml/min; $n = 8$) and severe renal impairment (CrCl < 30 ml/min; $n = 7$). Patients with mild renal impairment (CrCl 90–60 ml/min) were not included in the dataset. Plasma concentrations of tirofiban were measured after 0.25, 0.50, 0.75, 1, 2, 3, 4, and 6 h in all patients and additionally after 8, 10, and 12 h in patients with renal impairment. Supplementary Table 2 presents the estimated PK parameters.

The elimination of tirofiban occurs by renal and biliary excretion, as it has been shown by experiments with radioactively labelled tirofiban administered to healthy individuals. Here, 66% of radioactivity was recovered in the urine and 23% in the feces, with a total recovery of radioactivity of 91%. The half-life of tirofiban is approximately 1.5 h. In clinical studies, patients with decreased renal function showed a reduced plasma clearance of tirofiban. Thus, in patients with creatinine clearance < 30 ml/min, the plasma clearance is reduced over 50%. [15]. The second term of the previous equation, $Be^{-\beta t}$, reflects the elimination of the tirofiban from the body. For renally impaired subjects, $Be^{-\beta t}$ declines slower, indicating that the elimination half-life of tirofiban is greater, which results in a higher concentration of the drug, compared with subjects with a normal renal function. Then, to simulate the time profile of plasma concentrations of tirofiban for different scenarios, a two-compartment ordinary differential equation (ODEs) was applied:

$$\begin{aligned} \frac{dXc}{dt} &= I(t) + k_{21}X_p - k_{12}X_c - k_{10}X_c \\ \frac{dXc}{dt} &= k_{12}X_C - k_{21}X_p \end{aligned},$$

where.

$I(t)$ is the rate of drug administration and has units of mass.time^{-1}, X_c is the amount of drug in the central compartment and has units of mass, X_p is the amount of drug in the peripheral compartment and has units of mass, k_{12} is the first-order transfer rate constant from the central compartment to the peripheral compartment and has units of time^{-1}, k_{21} is the first-order transfer rate constant from the peripheral compartment to the central compartment and has units of time^{-1}, k_{10} is the first-order elimination rate constant from the central compartment and has units of time^{-1}.

Here the estimated α, β, A and B were used to calculate the ODEs parameters [16].The ODE set was integrated using the "solve_ivp" function from the SciPy package (version 1.1.0). By solving the two sets of ODEs with different conditions, the effect of different delays and interruptions was evaluated. Finally, the dosage of a second bolus was estimated allowing a rapid recovery of tirofiban plasma levels within the anticipated therapeutic window. This optimization was performed using "Nelder-Mead" method of the "minimize" function from the SciPy package (version 1.1.0).

Results

Patient characteristics

The real-world cohort during the product development consisted of overall 23 patients (normal renal function: $n = 8$, moderate impairment: $n = 8$, severe impairment: $n = 7$). Patients were of a mean age of 60.4 years (range 31–82 years). Patients in the normal renal function group had a slightly higher weight (90.9 vs. 82.0 kg) and BMI (31.46 vs. 28.60 kg/m^2) compared to those in the moderate and severe renal function groups. Patients were almost equally split between male and female (11 male vs. 12 female) with more White patients (17 patients) enrolled compared to Black/African American (6 patients). There were no patients of Hispanic/Latino ethnicity or of Asian descent. None of the patients had acute coronary syndrome.

Parameter estimation and model verification

PK parameters of tirofiban for the three groups of patients according to renal function have been estimated as described above (Supplementary Table 2). Calculated PK parameter estimates were used to develop a dynamic model to simulate the plasma concentration–time profile of tirofiban. Here, we demonstrate a good fit between modelled and real-world patient data, thus confirming our model to be suitable for further simulations (Supplementary Fig. 1b–d).

Comparison between EU and US dosage regimens

Based on calculated PK parameters, simulations were carried out by applying EU and US dosage recommendations, as described above. Briefly, EU recommendations implicate both a lower loading and maintenance doses (loading concentration of 0.4 µg/kg/min over 30 min, followed by 0.1 µg/kg/min infusion) than US recommendations (25 µg/kg within 5 min followed by infusion at a rate of 0.15 µg/kg/min for up to 18 h) in patients with normal renal function. Furthermore, renal dose adjustment is recommended only for patients with severe renal impairment (CrCl < 30 ml/min) in EU but start with moderately impaired function (CrCl ≤ 60 ml/min) in the US However, while EU recommends reduction of both, bolus and infusion rate, US recommendations include an unchanged bolus dose followed by a reduced maintenance infusion rate [14, 15]. Figure 1 shows plasma concentration–time curves of tirofiban for three groups of patients according to renal function. In all scenarios, in the US regimen, the initial plasma concentration following bolus administration is considerably higher and the steady-state concentration is achieved faster than in the EU regimen. In case of normal renal function as well as severe renal impairment, where the dosage reduction occurs in both regimens, the steady-state plasma concentration is lower in the EU than in the US regimen. However, in severe renal impairment, the steady-state concentration in the EU regimen is reached even more slowly than in normal function. For moderate renal function, the steady-state concentration is higher in the EU than in the US regimen.

Effects of delays and interruptions in EU and US dosage regimens

In the next step, we mathematically simulated the effect of different delays and interruptions of administration on plasma drug concentration. Here, we demonstrate that short delays between the bolus and initiation of continuous infusion do not result in significant changes in the drug concentrations in either EU or US regimens regardless of renal function (Fig. 2). However, a longer than 30-min delay leads to considerable decrease in plasma concentrations in the EU dosing regimen in all three groups (Fig. 2b, d, f). Notably, in the US regimen, the concentration decrease after delays of more than 30 min is lower than in EU dosing. Furthermore, in moderate or severe renal dysfunction group, the influence of delay is less pronounced than in normal renal function in US regimen (Fig. 2a, c, e). Similarly, we show that interruptions of continuous infusion over 30 min lead to considerable decrease in tirofiban plasma concentrations (Fig. 3). This effect is even more pronounced in the EU regimen (Fig. 3 b, d, f). According to the US dosage recommendations, the decrease in concentrations after interruption are

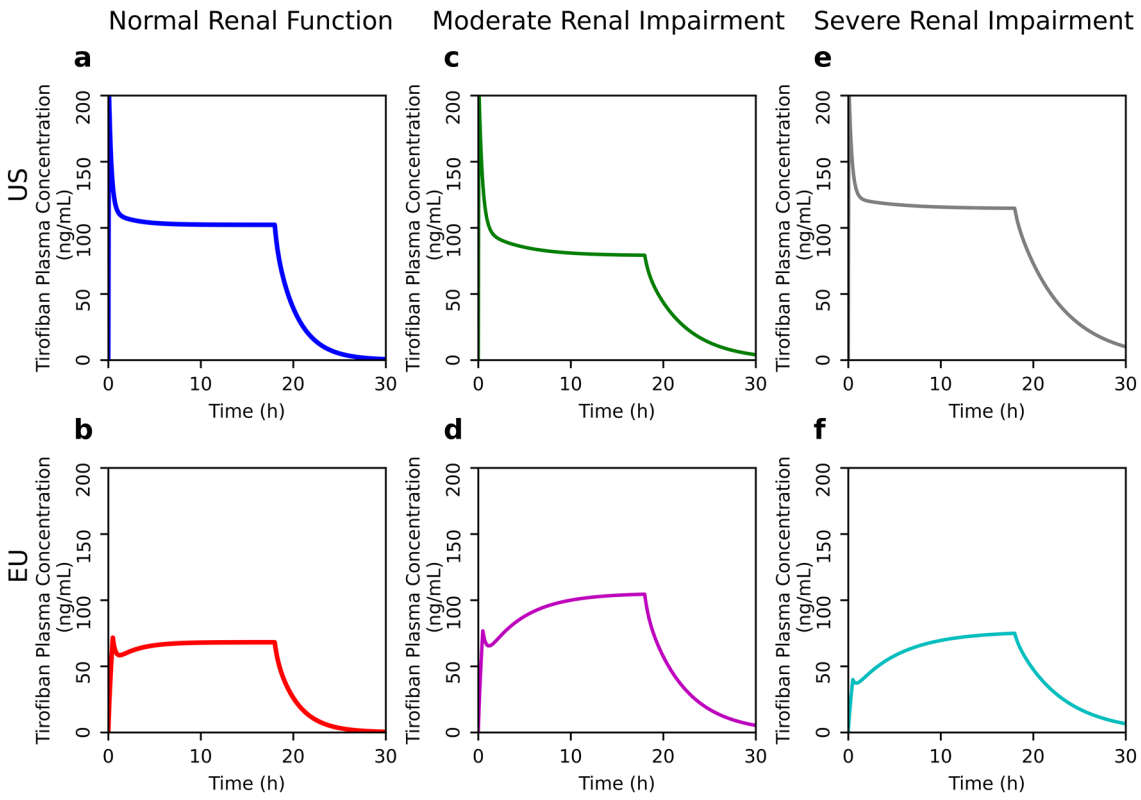

Fig. 1 Plasma concentration–time curves of tirofiban according to renal function in US **(a, c, e)** and EU **(b, d, f)** dosing regimens

less pronounced in renal dysfunction group than in case of normal renal function group (Fig. 3a, c, e).

Additionally, we estimated the dosage of a possible second bolus to compensate for the delays or interruptions in intravenous tirofiban application in both EU and US regimens (Table 1 and 2; Supplementary Fig. 2 and 3).

Discussion

Several studies have investigated the effect of the GP IIb/IIIa inhibitor tirofiban in patients with ACS or in patients undergoing high-risk PCI. The PRISM-PLUS trial showed a reduction in major adverse cardiac events (MACE) at 30 days with GP IIb/IIIa inhibitor plus unfractionated heparin as compared to unfractionated heparin alone [7]. In the Randomized Efficacy Study of Tirofiban for Outcomes and Restenosis (RESTORE) trial, the administration of tirofiban was not associated with a significant reduction in MACE [8]. A study by Steinhubl et al. including 501 patients treated with abciximab, tirofiban and eptifibatide, demonstrated that the levels of platelet function inhibition are independently associated with the rate of MACE after PCI [17]. Moreover, it has been demonstrated that normal myocardial perfusion after fibrinolytic therapy for ST-elevation myocardial infarction (STEMI) and after PCI for ACS is associated with higher GPI receptor occupancy in the setting of eptifibatide therapy [18–20]. Thus, higher doses of tirofiban would similarly be expected, in turn, to provide greater receptor occupancy to provide sufficient platelet inhibition to translate into a beneficial clinical effect. In 2004, the ADVANCE trial demonstrated a significant reduction of ischemic events using tirofiban in the setting of high-risk PCI when administered at a high dose bolus of 25 µg/kg followed by infusion of 0.15 µg/kg/min for 24–48 h [9]. A systematic pooled meta-analysis of RCTs investigating tirofiban versus placebo or abciximab including over 20,000 patients confirmed a reduction of death or combined endpoint of death and MI with the use of tirofiban. [21].

All these studies strengthen our hypothesis that maintenance of a proper plasma concentration of tirofiban is crucial for sufficient antithrombotic effect and a better clinical outcome. Interestingly, the dosage recommendations for tirofiban differ between EU and US In the present study, we systematically compare two dosing regimens and simulated different deviations from the recommended administration mode using a mathematical model. USUSOur simulations of tirofiban plasma concentration in normal renal function, using the US dosing regimen, demonstrated a faster increase in plasma concentration to almost double steady-state level

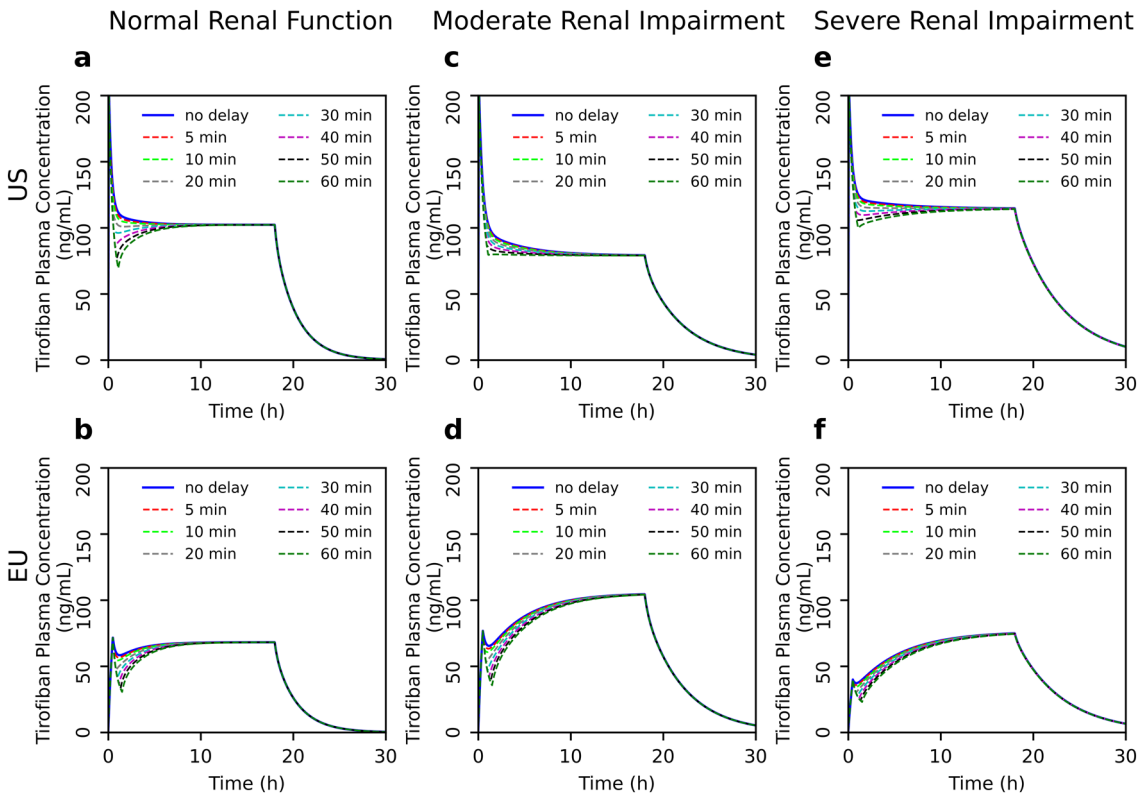

Fig. 2 Effects of different delays between bolus and initiation of continuous infusion of tirofiban on plasma drug concentration in different populations according to renal function. Comparison between US **(a, c, e)** and EU **(b, d, f)** dosing regimens

followed by a drop to a still high level of plasma tirofiban concentration of over 100 ng/ml. In the EU dosing regimen, the bolus is administered at a lower dose over a longer timeframe followed by continuous infusion. This leads to almost constant plasma tirofiban levels during the entire administration period, which is, however, considerably lower than in the US regimen. By contrast, in case of moderate renal impairment, the steady-state concentration in the EU regimen is higher than in the US regimen as there is no dosage adjustment in the EU recommendation. In our model of severe renal insufficiency, we have demonstrated a lower steady-state tirofiban concentration, which is reached more slowly in the EU than in the US regimen. This can be explained by the fact that in the EU regimen, both the loading as well as maintenance doses are reduced, while the bolus dose remains unchanged in the US recommendations. Furthermore, we show here that deviations from the proper administration mode affect the concentration of tirofiban. However, shorter delays or interruptions do not have a major impact on plasma drug levels, whereas deviations of over 30 min show considerable effects. This finding is consistent with the elimination half-life of tirofiban of approximately 2 h [6]. Of note, regardless of renal function, the changes in plasma levels are less pronounced using the US regimen compared to the EU regimen. This is most likely due to a higher dose of initial bolus in the US regimen, which is not reduced even in case of severe renal impairment.

In the context of clinical studies, the EU regimen in patients with normal renal function is comparable to the dosage used in the PRISM-PLUS trial [7], whereas the US dosing regimen was used in the ADVANCE trial [9], both showing a beneficial antithrombotic effect of tirofiban. By contrast, in the RESTORE trial which failed to demonstrate a MACE reduction by use of GP IIb/IIIa inhibitors, a lower bolus dose has been applied (10 µg/kg bolus followed by infusion at a rate of 0.15 µg/kg/min). Therefore, one could speculate that both EU and US regimens are equal in terms of their antithrombotic effect. Despite the higher steady-state drug level in the US dosing regimen, the ADVANCE study did not reveal a higher rate of adverse events such as major bleedings [9]. Nonetheless, it is important to note that the present study is based on a simulated mathematical model. Even though we demonstrated that the changes in drug concentration following delays or interruptions in the US regimen are less pronounced than in the EU regimen, it is not clear what concentration is required to induce adequate effect on platelet aggregation. This represents the main limitation of our study as we only provide a pharmacokinetics simulation without taking into account the pharmacodynamics

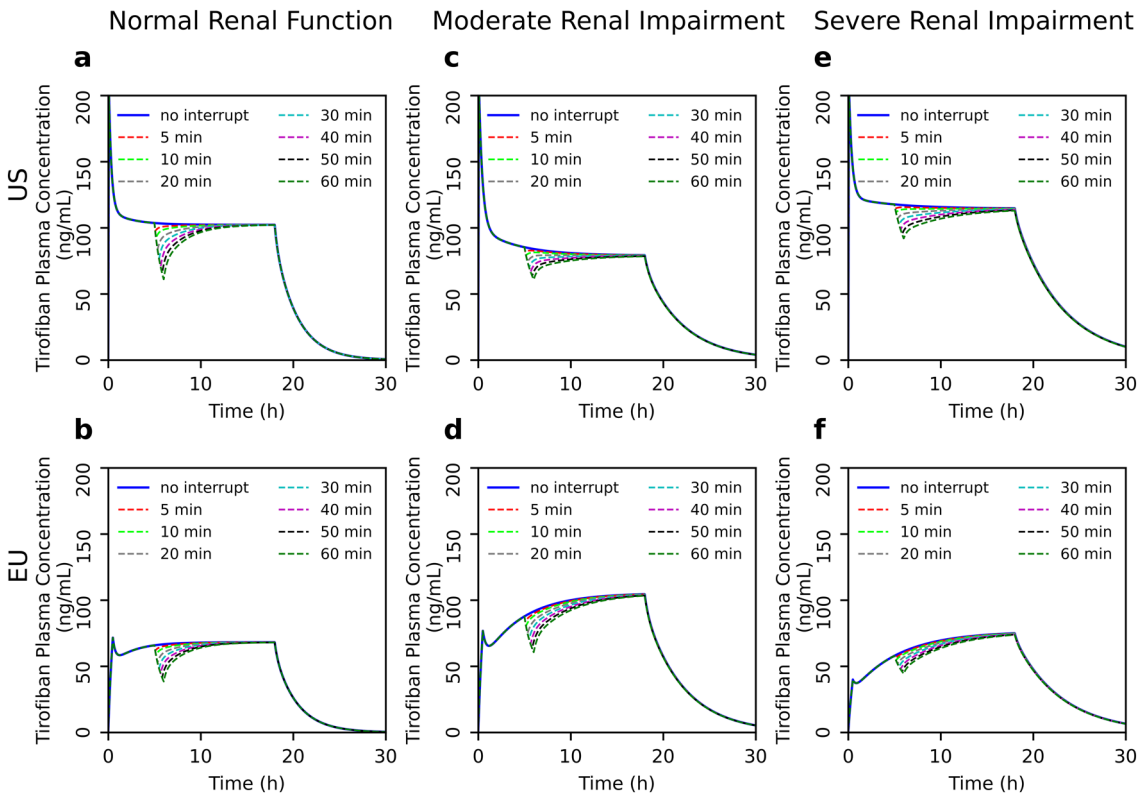

Fig. 3 Effects of different interruptions of continuous infusion of tirofiban on plasma drug concentration in different populations according to renal function. Comparison between US **(a, c, e)** and EU **(b, d, f)** dosing regimens

Table 1 Dosage of the 2nd bolus after different delays between bolus administration and initiation of infusion of tirofiban in patients with normal renal function

	Delay (min)	5	10	20	30	40	50	60	70
US	Dosage of 2nd bolus (µg/kg)	–	–	–	1.5	2.84	4.05	5.15	6.16
	in % of 1st bolus	–	–	–	6%	11%	16%	21%	25%
EU	Dosage of 2nd bolus (µg/kg)	0.58	0.64	0.76	0.86	0.95	1.04	1.11	1.19
	in % of 1st bolus	5%	5%	6%	7%	8%	9%	9%	10%

Table 2 Dosage of the 2nd bolus after different infusion interruptions of tirofiban in patients with normal renal function

	Interruption (min)	5	10	20	30	40	50	60	70
US	Dosage of 2nd bolus (µg/kg)	0.48	1.18	2.5	3.7	4.82	5.86	6.83	7.73
	in % of 1st bolus	2%	5%	10%	15%	19%	23%	27%	31%
EU	Dosage of 2nd bolus (µg/kg)	0.16	0.24	0.37	0.5	0.61	0.72	0.82	0.92
	in % of 1st bolus	1%	2%	3%	4%	5%	6%	7%	8%

of the drug. Another pharmacokinetic modelling study published by Lakings et al. in 2012 used the simulation approach to identify an appropriate dosage in patients with severely impaired renal function which would lead to a similar tirofiban time-concentration profile as reached by the US regimen dosage in patients with normal renal function [22]. When comparing the real-life and modeled concentration–time profiles in this study and our study at the same dosing regimens, it is notable that in our study the steady-state plasma levels are considerably higher in both normal and severely impaired renal function. Even more pronounced is the concentration difference in patients with severe renal impairment after the recommended dosing rate adjustment. This is surprising as the reduced renal elimination would expectedly lead to higher plasma concentrations, as it is the case in our simulations. However, the differences in the estimated PK parameters in both studies are most likely due to a relatively low number of

measurements, on which the estimated parameters are based. This is another limitation of the present study.

In conclusion, differences in tirofiban dosing regimens between the US and EU and potential infusion interruptions have important effects on drug levels that may impact, in turn, on degrees of platelet inhibition. The totality of evidence supports that high levels of receptor occupancy by GPIs are required to reduce clinical thrombotic events. Thus, the findings of our modelling studies may help to explain differences in clinical outcomes observed in trials of tirofiban for the treatment of high-risk coronary artery disease. Our data indicates towards equality of both regimens in terms of clinical outcomes and possible higher probability of side effects due to a higher steady-state concentration in US regimen. However, this study remains a mathematical model and evidently future clinical trials are required for a real-world comparison between the two regimens in different clinical settings.

Supplementary Information The online version contains supplementary material available at https://doi.org/10.1007/s11239-022-02654-0.

Author contributions NH and MM performed the mathematical simulations, prepared the material, analyzed, and interpreted the data, wrote the manuscript and approved the final version to be published. JMM, AMN, AK, AP, MV, PAG, UST and MK substantially contributed to interpretation of data, revised the manuscript critically for important intellectual content and approved the final version to be published. CJ substantially contributed to conception and design and the interpretation of data, revised the manuscript critically for important intellectual content and approved the final version to be published.

Funding Open Access funding enabled and organized by Projekt DEAL. This work was supported by Medicure Inc. through an unrestricted grant. Institutional support has been received by the German Research Council (Sonderforschungsbereich 1116).

Data availability The data underlying this article are available in the article and in its online supplementary material.

Code availability Python™ codes to simulate pharmacokinetics of tirofiban in this manuscript are available on request.

Declarations

Conflicts of interest Paul A. Gurbel reports grants and personal fees from Bayer HealthCare LLC, Otitopic Inc, Amgen, Janssen, Medicure, and US WorldMeds LLC; grants from Instrumentation Laboratory, Haemonetics, Medicure Inc, Idorsia Pharmaceuticals, and Hikari Dx; personal fees from UpToDate. Paul A. Gurbel is a relator and expert witness in litigation involving clopidogrel. In addition, Paul A. Gurbel holds two patents, Detection of restenosis risk in patients and Assessment of cardiac health and thrombotic risk in a patient. Nadia Heramvand reports a grant from Medicure Inc. Marco Valgimigli reports research grants to the Inselspital from Medicure Inc. for the conduct of the FABOLUS FASTER Trial.

References

1. Fuster V, Badimon L, Badimon JJ et al (1992) The pathogenesis of coronary artery disease and the acute coronary syndromes (1). N Engl J Med 326:242–250. https://doi.org/10.1056/NEJM199201233260406
2. van de Werf F (1997) Clinical trials with glycoprotein IIb/IIIa receptor antagonists in acute coronary syndromes. Thromb Haemost 78:210–213
3. Coller BS (1995) Blockade of platelet GPIIb/IIIa receptors as an antithrombotic strategy. Circulation 92:2373–2380. https://doi.org/10.1161/01.cir.92.9.2373
4. Lefkovits J, Plow EF, Topol EJ (1995) Platelet glycoprotein IIb/IIIa receptors in cardiovascular medicine. N Engl J Med 332:1553–1559. https://doi.org/10.1056/NEJM199506083322306
5. Hartman GD, Egbertson MS, Halczenko W et al (1992) Non-peptide fibrinogen receptor antagonists. 1. Discovery and design of exosite inhibitors. J Med Chem 35:4640–4642. https://doi.org/10.1021/jm00102a020
6. McClellan KJ, Goa KL (1998) Tirofiban. A review of its use in acute coronary syndromes. Drugs 56:1067–1080. https://doi.org/10.2165/00003495-199856060-00017
7. Platelet Receptor Inhibition in Ischemic Syndrome Management in Patients Limited by Unstable Signs and Symptoms (PRISM-PLUS) Study Investigators (1998) Inhibition of the platelet glycoprotein IIb/IIIa receptor with tirofiban in unstable angina and non-Q-wave myocardial infarction. N Engl J Med 338:1488–1497. https://doi.org/10.1056/NEJM199805213382102
8. Investigators R (1997) Effects of platelet glycoprotein IIb/IIIa blockade with tirofiban on adverse cardiac events in patients with unstable angina or acute myocardial infarction undergoing coronary angioplasty. The RESTORE Investigators. Randomized Efficacy Study of Tirofiban for Outcomes and REstenosis. Circulation 96:1445–1453. https://doi.org/10.1161/01.cir.96.5.1445
9. Valgimigli M, Percoco G, Barbieri D et al (2004) The additive value of tirofiban administered with the high-dose bolus in the prevention of ischemic complications during high-risk coronary angioplasty: the ADVANCE trial. J Am Coll Cardiol 44:14–19. https://doi.org/10.1016/j.jacc.2004.03.042
10. Bass TA (2015) High-risk percutaneous coronary interventions in modern day clinical practice: current concepts and challenges. Circ Cardiovasc Interv 8:e003405. https://doi.org/10.1161/CIRCINTERVENTIONS.115.003405
11. Roffi M, Chew DP, Mukherjee D et al (2002) Platelet glycoprotein IIb/IIIa inhibition in acute coronary syndromes. Gradient of benefit related to the revascularization strategy. Eur Heart J 23:1441–1448. https://doi.org/10.1053/euhj.2002.3160
12. Amsterdam EA, Wenger NK, Brindis RG et al (2014) 2014 AHA/ACC guideline for the management of patients with non-ST-elevation acute coronary syndromes: a report of the American College of Cardiology/American Heart Association Task

Force on Practice Guidelines. J Am Coll Cardiol 64:e139–e228. https://doi.org/10.1016/j.jacc.2014.09.017
13. Roffi M, Patrono C, Collet J-P et al (2016) 2015 ESC Guidelines for the management of acute coronary syndromes in patients presenting without persistent ST-segment elevation: task force for the management of acute coronary syndromes in patients presenting without persistent ST-segment elevation of the European Society of Cardiology (ESC). Eur Heart J 37:267–315. https://doi.org/10.1093/eurheartj/ehv320
14. U.S. Food and Drug Administration (2001) Aggrastat (tirofiban Hydrochloride) injection & premixed injection: drug approval package. https://www.accessdata.fda.gov/drugsatfda_docs/nda/99/20912S001_Aggrastat.cfm. Accessed January 2020.
15. European Medicines Agency. The European Agency for the Evaluation of Medicinal Products (1999) Opinion following an article 10 referral Aggrastat. International Nonproprietary Name (INN): Tirofiban. https://www.ema.europa.eu/en/documents/referral/opinion-following-article-10-referral-aggrastat-international-non-proprietary-name-inn-tirofiban_en.pdf. Accessed March 2020
16. Jambhekar SS, Breen PJ (2009) Basic pharmacokinetics. Repr, Pharmaceutical Pr, London
17. Steinhubl SR, Talley JD, Braden GA et al (2001) Point-of-care measured platelet inhibition correlates with a reduced risk of an adverse cardiac event after percutaneous coronary intervention: results of the GOLD (AU-assessing Ultegra) multicenter study. Circulation 103:2572–2578. https://doi.org/10.1161/01.cir.103.21.2572
18. Gibson CM, Jennings LK, Murphy SA et al (2004) Association between platelet receptor occupancy after eptifibatide (integrilin) therapy and patency, myocardial perfusion, and ST-segment resolution among patients with ST-segment-elevation myocardial infarction: an INTEGRITI (Integrilin and Tenecteplase in Acute Myocardial Infarction) substudy. Circulation 110:679–684. https://doi.org/10.1161/01.CIR.0000137912.11655.F6
19. Deibele AJ, Jennings LK, Tcheng JE et al (2010) Intracoronary eptifibatide bolus administration during percutaneous coronary revascularization for acute coronary syndromes with evaluation of platelet glycoprotein IIb/IIIa receptor occupancy and platelet function: the Intracoronary Eptifibatide (ICE) Trial. Circulation 121:784–791. https://doi.org/10.1161/CIRCULATIONAHA.109.882746
20. Gurbel PA, Tantry US (2010) Delivery of glycoprotein IIb/IIIa inhibitor therapy for percutaneous coronary intervention: why not take the intracoronary highway? Circulation 121:739–741. https://doi.org/10.1161/CIR.0b013e3181d40dc9
21. Valgimigli M, Biondi-Zoccai G, Tebaldi M et al (2010) Tirofiban as adjunctive therapy for acute coronary syndromes and percutaneous coronary intervention: a meta-analysis of randomized trials. Eur Heart J 31:35–49. https://doi.org/10.1093/eurheartj/ehp376
22. Lakings DB, Janzen MC, Schneider DJ (2012) Pharmacokinetic modeling of the high-dose bolus regimen of tirofiban in patients with severe renal impairment. Coron Artery Dis 23:208–214. https://doi.org/10.1097/MCA.0b013e328351556e

Supplementary Fig. 1

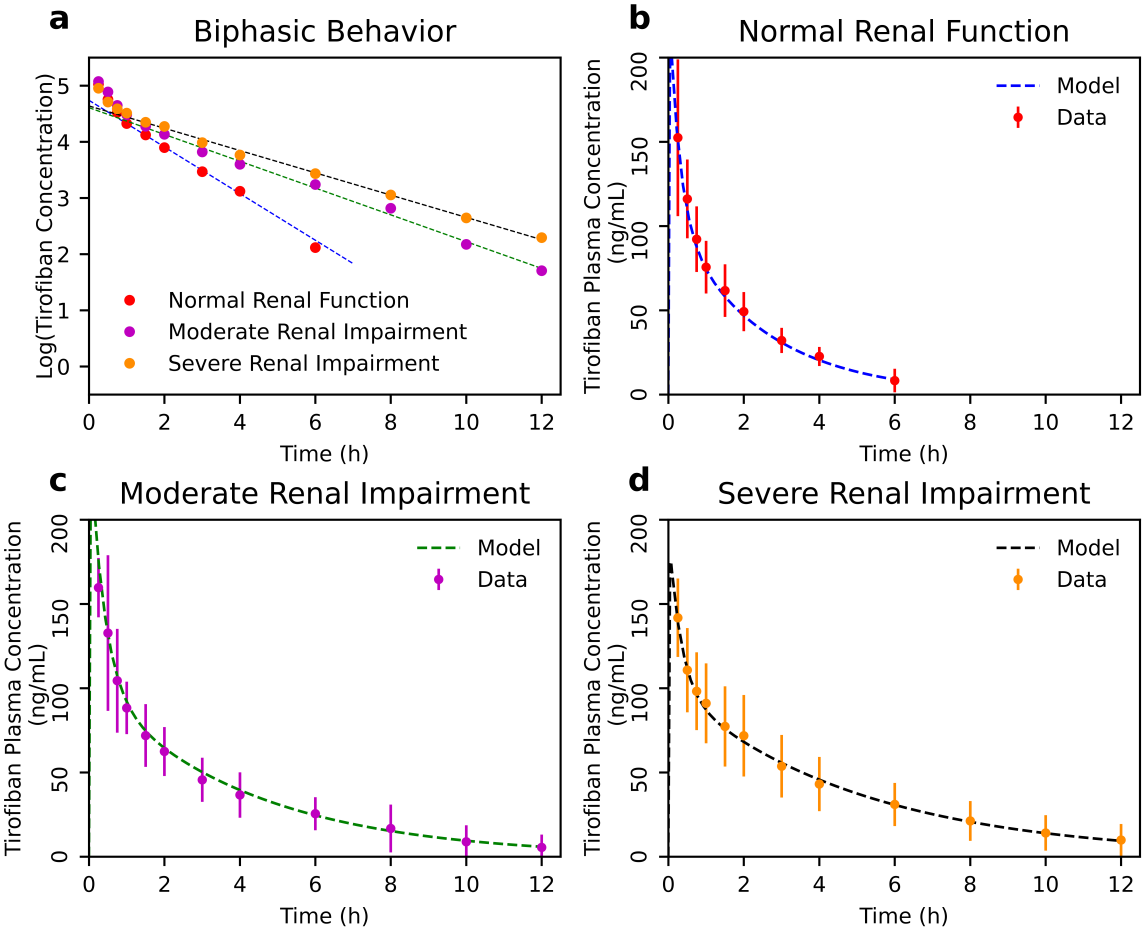

Supplementary Fig. 2

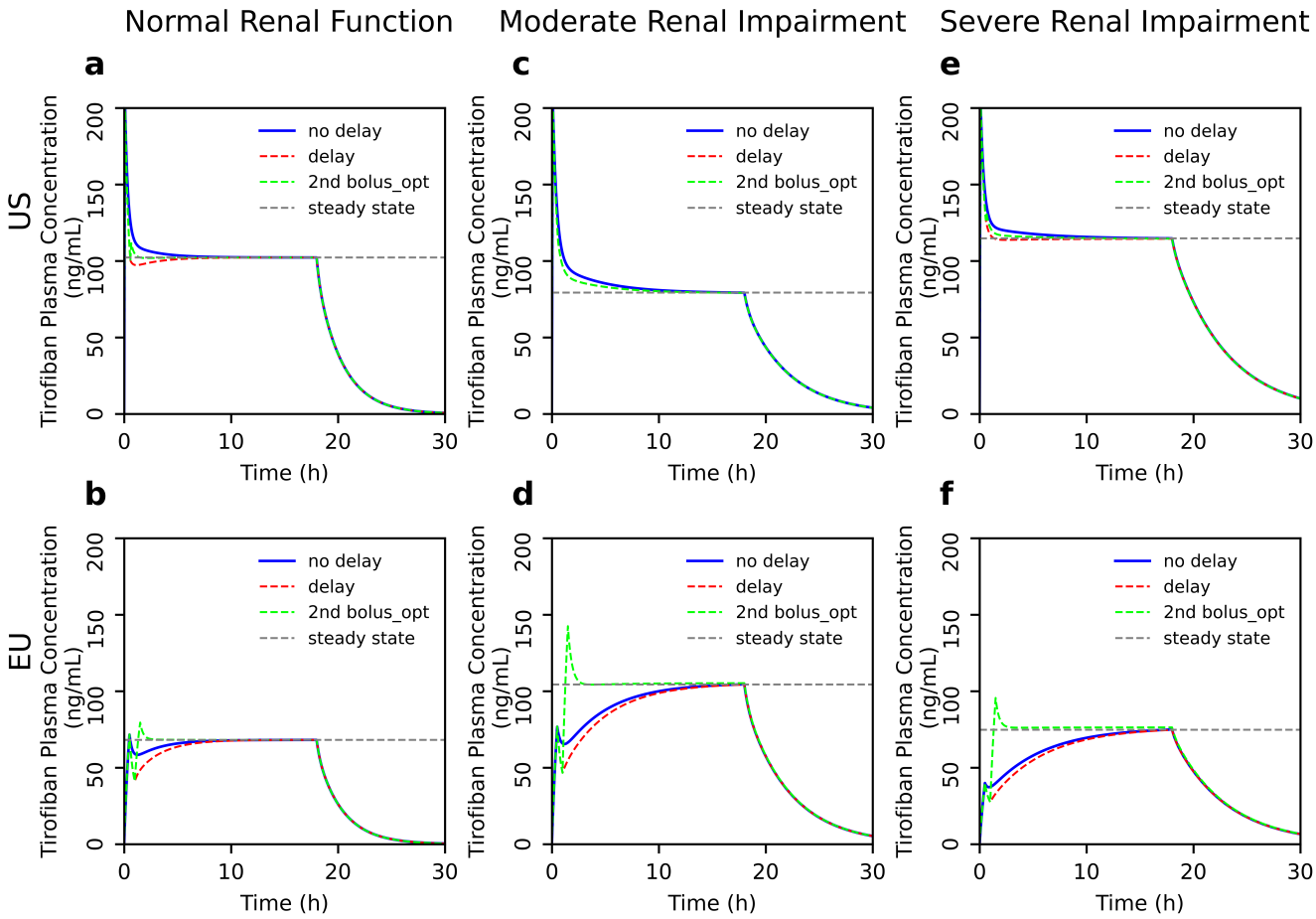

Supplementary Fig. 3

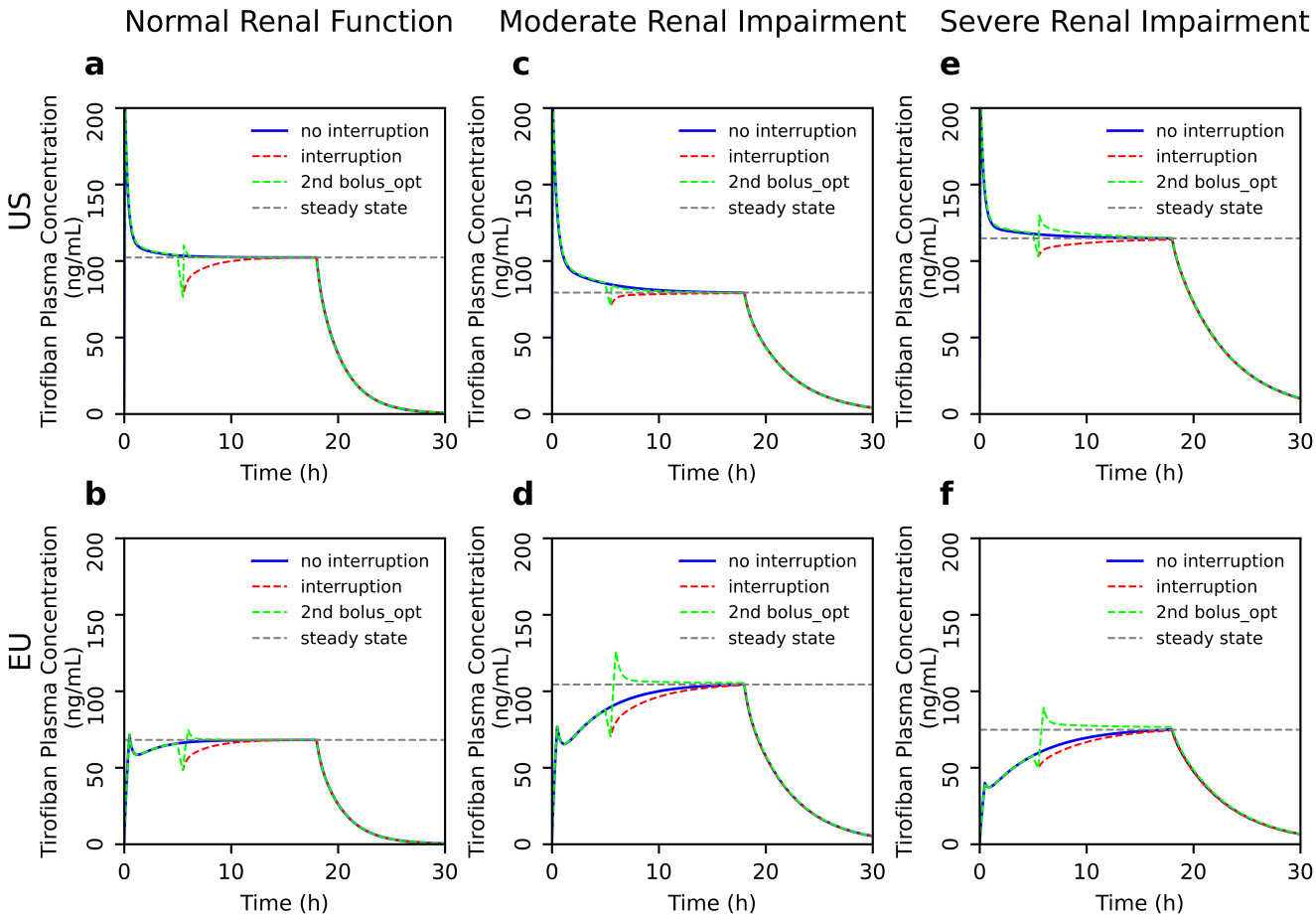

5 | Conclusion

This thesis aimed to explore the optimal strategies for modeling biological systems. The high-level complexity of the biological systems hinders the ability to investigate them as a whole. The complexity may lie both in the high number of interacting components as well as their complicated underlying relationships. Recently available high-throughput empirical techniques that are mainly employed to decipher these complexities are a blessing, yet inadequate due to the high level of noise and cost. Intrinsic plasticity and noise of the biological systems add another level of twist. As a result, available experimental datasets are often incomplete and noisy. To overcome these shortcomings, advanced modeling strategies are needed.

The biological network inference problem can represent all these challenges. For example, in gene-knockout studies investigating gene regulatory networks, the available empirical data are huge, noisy, and incomplete. Inferablity was introduced in this thesis, as a measure to quantify the number of interactions that can be inferred from a set of experimental data for a specific network. It was shown that inferablity is highly dependent on the underlying structure of the network as well as the number of data points.

It was demonstrated that compartmentalizing the system is a suitable approach to tackle the mentioned challenges. Compartmentalizing means decomposing a complex system into simpler subsystems (compartments) to declutter the model from unnecessary details and see how these subsystems work together. Besides network inference problems, multi-compartment pharmacokinetic modeling is a good example of such coarse-grained models. They are simple but inclusive tools in the process of drug development.

In general, this thesis aimed to convey this message that before modeling a biological system, it is highly important to anticipate the level of model complexity needed to answer the questions of the study. Not too complex as the unnecessary details cause inconvenience and not too simple as the biology of the system gets lost.

References

[1] Anthony Trewavas. A brief history of systems biology. *The Plant cell*, 18(10):2420–2430, 10 2006.

[2] Ingo Brigandt and Alan Love. In Edward N. Zalta, editor, *Reductionism in Biology*. Metaphysics Research Lab, Stanford University, https://plato.stanford.edu/archives/spr2017/entries/reduction-biology/, spring 2017 edition, 2017.

[3] Marc H V Van Regenmortel. Reductionism and complexity in molecular biology. *EMBO reports*, 5(11):1016–1020, 11 2004.

[4] Avi Ma'ayan. Complex systems biology. *Journal of the Royal Society, Interface*, 14(134):20170391, 09 2017.

[5] Raina Robeva. Systems biology - old concepts, new science, new challenges. *Frontiers in Psychiatry*, 1:1, 2010.

[6] Olaf Wolkenhauer. Systems biology: The reincarnation of systems theory applied in biology? *Briefings in Bioinformatics*, 2(3):258–270, 09 2001.

[7] Manfred Drack and Olaf Wolkenhauer. System approaches of weiss and bertalanffy and their relevance for systems biology today. *Seminars in Cancer Biology*, 21(3):150–155, 2011.

[8] Manfred Drack. Ludwig von bertalanffy's organismic view on the theory of evolution. *Journal of Experimental Zoology Part B: Molecular and Developmental Evolution*, 324(2):77–90, 2015.

[9] Ludwig Von Bertalanffy. *General System Theory: Foundations, Development, Applications*. George Braziller Inc; Revised edition, March 1976.

[10] Robert Rosen. *Life itself: A Comprehensive Inquiry into the Nature, Origin, and Fabrication of Life*. New York: Columbia University Press, 1991.

[11] Robert Rosen. The representation of biological systems from the standpoint of the theory of categories. *The bulletin of mathematical biophysics*, 20(4):317–341, 1958.

[12] Ivo Siekmann. An applied mathematician's perspective on rosennean complexity. *Ecological Complexity*, 35:28–38, 09 2018.

[13] Albert-László Barabás. *Network Science*. Cambridge University Press, July 2016.

[14] Uri Alon. *An Introduction to Systems Biology: Design Principles of Biological Circuits*. Taylor and Francis Inc, 1st edition, July 2006.

[15] Duncan J. Watts and Steven H. Strogatz. Collective dynamics of 'small-world'networks. *Nature*, 393(6684):440–442, 1998.

[16] Albert-László Barabási and Réka Albert. Emergence of scaling in random networks. *Science*, 286(5439):509, 10 1999.

[17] Markus I. Eronen and Daniel Stephen Brooks. Levels of organization in biology. In Edward N. Zalta, editor, *The Stanford Encyclopedia of Philosophy*. Metaphysics Research Lab, Stanford University, https://plato.stanford.edu/archives/spr2018/entries/levels-org-biology/, Spring 2018.

[18] Sara Green. Revisiting generality in biology: systems biology and the quest for design principles. *Biology & Philosophy*, 30(5):629–652, 2015.

[19] Piers J. Ingram, Michael PH Stumpf, and Jaroslav Stark. Network motifs: structure does not determine function. *BMC Genomics*, 7(1):108, 2006.

[20] Roger P Alexander, Philip M Kim, Thierry Emonet, and Mark B Gerstein. Understanding modularity in molecular networks requires dynamics. *Science signaling*, 2(81):pe44–pe44, 07 2009.

[21] Armindo Salvador. Uri alon, an introduction to systems biology: Design principles of biological circuits, chapman & hall/crc, london, isbn 1584886420, gbp 30.99, 2007 (320 pp.). *Mathematical Biosciences - MATH BIOSCI*, 215:193–195, 10 2008.

[22] Andreea Munteanu, James Cotterell, Ricard V. Solé, and James Sharpe. Design principles of stripe-forming motifs: the role of positive feedback. *Scientific Reports*, 4(1):5003, 2014.

[23] Sara Green and Olaf Wolkenhauer. Tracing organizing principles: learning from the history of systems biology. *Hist Philos Life Sci*, 35(4):553–576, 2013.

[24] Maureen A. O'Malley Ingo Brigandt, Sara Green. *Systems Biology and Mechanistic Explanation*. Routledge, 1st edition, 7 July 2017.

[25] James B. Bassingthwaighte, Erik Butterworth, Bartholomew Jardine, and Gary M. Raymond. *Compartmental Modeling in the Analysis of Biological Systems*, pages 391–438. Humana Press, Totowa, NJ, 2012.

[26] Jarosław Kwapień and Stanisław Drożdż. Physical approach to complex systems. *Physics Reports*, 515(3):115–226, 2012.

[27] Carlos Gershenson, Alexander F. Siegenfeld, and Yaneer Bar-Yam. An introduction to complex systems science and its applications. *Complexity*, 2020:6105872, 2020.

[28] M. E. J Newman. *Networks An Introduction*. Oxford University Press, March 2010.

[29] Erdös P. and Rényi A. On the evolution of random graphs. *Publication of the Mathematical Institute of the Hungarian Academy of Sciences*, 5:17–61, 1960.

[30] H. Jeong, B. Tombor, R. Albert, Z. N. Oltvai, and A. L. Barabási. The large-scale organization of metabolic networks. *Nature*, 407(6804):651–654, 2000.

[31] Harrison B. Smith, Hyunju Kim, and Sara I. Walker. Scarcity of scale-free topology is universal across biochemical networks. *Scientific Reports*, 11(1):6542, 2021.

[32] David E. Featherstone and Kendal Broadie. Wrestling with pleiotropy: Genomic and topological analysis of the yeast gene expression network. *BioEssays*, 24(3):267–274, 2002.

[33] Reuven Cohen and Shlomo Havlin. Scale-free networks are ultrasmall. *Phys. Rev. Lett.*, 90:058701, Feb 2003.

[34] Shai S. Shen-Orr, Ron Milo, Shmoolik Mangan, and Uri Alon. Network motifs in the transcriptional regulation network of escherichia coli. *Nature Genetics*, 31(1):64–68, 2002.

[35] Yong Wang. *Gene Regulatory Networks*, pages 801–805. Springer New York, New York, NY, 2013.

[36] Yong Wang, Trupti Joshi, Xiang-Sun Zhang, Dong Xu, and Luonan Chen. Inferring gene regulatory networks from multiple microarray datasets. *Bioinformatics*, 22(19):2413–2420, 7/28/2021 2006.

[37] Hiroaki Kitano. Biological robustness. *Nature Reviews Genetics*, 5(11):826–837, 2004.

[38] Axel Kowald Christoph Wierling Hans Lehrach Edda Klipp, Ralf Herwig. *Systems Biology in Practice: Concepts, Implementation and Application*. Wiley-Blackwell, 2008.

[39] Philip J. Breen Sunil S. Jambhekar. *Basic Pharmacokinetics*. Pharmaceutical Press, 1st edition, May 2009.

[40] CRESSMAN W. A. KAPLAN S. A. RIEGELMAN S. DITTERT, U W. and J. G. WAGNER. Guidelines for biopharmaceutical studies in man. *Academy of Pharmaceutical Sciences, American Pharmaceutical Association, Washington, D.C., U.S.A.*, 1972.

[41] Andrzej Kostrzewski Soraya Dhillon. *Clinical Pharmacokinetics*. Pharmaceutical Press, 1st edition, March 2006.

[42] Wikipedia contributors. Pharmacokinetics — Wikipedia, the free encyclopedia. https://en.wikipedia.org/w/index.php?title=Pharmacokinetics&oldid=1019790603, September 2021.

[43] *Introduction to Drug Disposition and Pharmacokinetics, Appendix 3: Curve Fitting*, pages 303–306. John Wiley & Sons, Ltd, 2016.

[44] Jure Leskovec and Andrej Krevl. SNAP Datasets: Stanford Large Network Dataset Collection,. http://snap.stanford.edu/data, June 2014.

[45] Dominick J. Angiolillo and Piera Capranzano. Pharmacology of emerging novel platelet inhibitors. *American Heart Journal*, 156(2, Supplement):10S–15S, 2008. Platelet Inhibitor Therapy: Current Perspectives and Emerging Novel Agents.

[46] Leonardo De Luca, Philippe Gabriel Steg, Deepak L. Bhatt, Davide Capodanno, and Dominick J. Angiolillo. Cangrelor: Clinical data, contemporary use, and future perspectives. *Journal of the American Heart Association*, 10(13):e022125, 2021/09/15 2021.

[47] Karen J. McClellan and Karen L. Goa. Tirofiban. *Drugs*, 56(6):1067–1080, 1998.

[48] U.s. food and drug administration, drug approval pacakge, aggrastat (tirofiban hydrochloride), July 2 2001.

[49] European medicines agency. the european agency for the evaluation of medicinal products, opinion following an article 10 referral aggrastat. international nonproprietary name (inn): Tirofiban., 1999.